Elucidating structure-property relationships of indacenodithiophene-copolymers for the development of soft and stretchable electronics

Parker J. W. Sommerville

A dissertation

submitted in partial fulfillment of the

requirements for the degree of

Doctor of Philosophy

University of Washington

2022

Reading Committee:

Prof. Christine K. Luscombe, Chair

Prof. Matthew Golder

Prof. Alshakim Nelson

Program Authorized to Offer Degree:

Chemistry

University of Washington

Abstract

Elucidating structure-property relationships of indacenodithiophene-copolymers for the development of soft and stretchable electronics

Parker J. W. Sommerville

Chair of the Supervisory Committee:
Professor Christine K. Luscombe
Materials Science & Engineering

Indacenodithiophene (IDT) copolymers are a promising class of copolymers for use as semiconducting charge transport layers in organic electronic devices. Certain IDT-copolymers have achieved hole mobilities that surpass 3.0 $cm^2\ V^{-1}\ s^{-1}$ in spite of its near-amorphous thin-film morphology. Their near-amorphous morphologies and high charge makes them prime candidates for use in stretchable electronics. Despite this potential, some IDT-copolymer systems including $PIDT_{C16}$-BT and $PIDT_{C16}$-TPD_{C1} undergo brittle failure and have high elastic moduli at low molecular weight, while at the same molecular weight others including $PIDT_{C16}$-BPD_{C1} undergo ductile failure with a comparatively smaller elastic modulus. The two studies described herein are focused understanding the how structural differences between IDT-copolymers impact their electronic and mechanical properties, to guide the design of IDT-copolymers for use in stretchable electronics. First, a series of $PIDT_{C16}$-BT-r-BPD_{C1} copolymers is investigated. It is found that the side chain extension profile of the hexadecyl side chains that extend from the IDT monomer, which is modulated by the degree of backbone coplanarity, has a deterministic role in the ability of an IDT-copolymer to plastically deform. Unfortunately, the increased hole mobility comes at the sacrifice of hole mobility. Second, side chain substitution was performed on both

BT-containing and TPD-containing IDT copolymers; all of which have coplanar backbones. Inclusion of larger alkyl side chains on the TPD monomer led to plasticly deforming IDT-copolymers with remarkably low elastic moduli. This improvement arises because of an inhibited ability for individual polymer chains to interdigitate alkyl their side chains with the side chains of neighboring polymer chains, which makes reorganization more facile. Unfortunately, the hole mobility is decreased due to the impact of interdigitation on the microstructural arrangement of IDT-copolymers. These results highlight the extensive role side chains play in determining the materials properties of IDT-copolymers and indicate the promise that side chain substitution can have in tuning the mechanical properties of IDT-copolymers.

ACKNOWLEDGMENTS

I'd like to thank from the outset my advisor Prof. Christine Luscombe for providing me the opportunity to perform the science I am passionate about, the patience and scientific expertise that enabled me to undertake these endeavors, and for holding me to a higher standard than I ever had myself. I must also thank her for her empathy and support that she provided me during personally difficult periods of time in my life, which allowed me the time to recover and push onwards. Thank you, Christine.

Fellow Luscombe group members both past and present provided invaluable support and discussion throughout the completion of my thesis work. Many thanks to all of you for the rigorous debates, practical advice, support, humorous moments, and genuine friendship.
To my friends, who provided me solace at many a turn, thank you for your patience. My relationships with you all are invaluable.

Few people have the opportunity complete their doctoral studies in their hometown. I'd like to thank from the bottom of my heart, my family, whose support, homecooked meals, and love were invaluable and my greatest treasures in life. Moments with you all helped me through many moments of self-doubt and struggle.

Specifically, to Korinne, there is no one individual who has supported me more than you these last five years than you. I could not have done this without your belief, support, and love. I'm so grateful to you for everything you have done and proud of who you have become during these past five years. This work is dedicated to you.

TABLE OF CONTENTS

Chapter 1. Contents
LIST OF FIGURES vi
LIST OF TABLES x
LIST OF SCHEMES xi
Chapter 1. Introduction 12
1.1 Conjugated Polymers 12
1.2 Conjugated Polymers as transport layer in OFET Devices 15
1.3 Mechanical property evaluation 18
1.4 A conjugated polymer paradigm: An overall relationship between polymer structure, conformational properties, thin-film microstructure, and the electromechanical properties of conjugated polymers 21
1.4.1 Chemical structure 23
1.4.2 Conformational properties 25
1.4.3 Solid state microstructure 26
1.5 Indacenodithiophene (IDT) copolymers 29
Chapter 2. Elucidating the Influence of Side-Chain Circular Distribution on the Crack Onset Strain and Hole Mobility of Near-Amorphous Indacenodithiophene Copolymers 33
2.1 Abstract 33
2.2 Introduction 34
2.3 Results and Discussion 37
2.4 Conclusion 48
2.5 Supplementary Information 48
2.5.1 Chemical synthesis 48
2.5.2 DFT Calculations 50
2.5.3 Crystallographic measurements 52
2.5.4 Charge Transport Property Measurement 54
2.5.5 Crack Onset Strain Measurements 57
2.5.6 Fast Scanning calorimetry Measurements 58
2.5.7 Optoelectronic measurements 60

2.5.8 ^{1}H NMR Spectra 62
Chapter 3. Uncovering the impact of side-chain interdigitation in determining the response to strain and hole mobility of planar indacenodithiophene copolymers through side chain substitution ... 69
3.1 Abstract 69
3.2 Introduction 70
3.3 Results and Discussion 73
3.5 Conclusion 86
3.6 Supplementary Information 87
3.6.1 Chemical synthesis 87
3.6.2 Size exclusion chromatography (SEC) characterization 94
3.6.3 Optoelectronic measurements 94
3.6.4 Fast Scanning Calorimetry (FSC) 95
3.6.5 Crystallographic measurements 98
3.6.6 Charge Modulation Spectroscopy (CMS) 99
3.6.7 Pseudo free-standing tensile tests (FOW) 101
3.6.8 Charge transport property measurements 101
3.6.8 ^{1}H NMR spectroscopy 105
Chapter 4. Outlook and recommendations for future work 113
4.1 Outlook 113
4.2 Side chain substitution of TIF- and TBIDT-copolymers 114

LIST OF FIGURES

Figure 1.1. MO diagram for oligo-ethylenes and polyacetylene demonstrating the formation of bandlike structures due to increasing conjugation length. 13

Figure 1.2. Schematic representation of two neighboring P3HT polymer chains, illustrating the direction of intra-molecular charge transport (blue) along the backbone and inter-molecular charge transport (red) between the conjugated rings of neighboring polymer chains. 14

Figure 1.3. Schematic of a bottom-gate top-contact (BGTC) organic field effect transistor (OFET) consisting of a substrate (orange), gate electrode (grey), dielectric layer (blue), conjugated polymer semiconductor layer (green) and source and drain electrodes (gold). 16

Figure 1.4. A schematic detailing the reorganization of polymer chains (black) beginning with initial strain (a) which causes elongation of the film through elastic deformation and chain alignment (b), followed by plastic flow if available to the system, which ultimately results in initial void formation (c) and void propagation that leads to rupture of the thin film (d). 20

Figure 1.5. A generic stress–strain curve. Labeled are mechanical properties of interest associated with strain (blue), stress (green), and energy (red). The units associated with each, respectively, are generally given in % strain, MPa, and MJ/m^3. Reproduced from reference 55 with permission from the American Chemical Society. 21

Figure 1.6. A visual representation of the conjugated polymer paradigm. 23

Figure 1.7. The chemical structures of P3HT (left) and PIDT$_{C16}$-BT (right). 25

Figure 1.8. Schematics of the microstructure of a semicrystalline polymer film, for example P3HT (a) disordered aggregates (b) and a completely amorphous film (c). Reproduced from reference 11 with permission from Nature Publishing Group. 27

Figure 1.9. Schematic representations of near-amorphous thin film morphologies of rigid (a) and semiflexible (b) polymer chains. 28

Figure 1.10. Basic design strategies for modification to the structure of IDT-BT. Republished from reference 25 with permission from the American Chemical Society. 30

Figure 1.11. Schematic illustration of the film microstructure of IDT-BT with low M_w (left), relatively higher M_w (middle), and ultrahigh M_w (right), where the red chain in each illustration represents chains of specific M_w, and the aggregate structures are marked by the blue areas. Republished from reference 45 with permission from the American Chemical Society. 31

Figure 2.1. Topological drawings of polymer chains, shown in red, that are relatively linear and nonlinear (top). Drawings of trimers viewed down the long axis of the polymer backbone with different degrees of coplanarity between monomer units because of varying magnitudes (small or large) of twist between monomer units (bottom). Red, yellow, and blue lines represent the conjugated rings of separate monomers. 36

Figure 2.2. Thin-film (a) UV–vis absorbance and (b) PL data of all IDT copolymers. 40

Figure 2.3. (a) (010) *d*-spacings, (b) zoomed-in regions of the raw-GIWAXS data, and (c) the normalized intensity and coherence length of the (001) backbone reflection signal. 41

Figure 2.4. Density functional theory calculations of $PIDT_{C16}$-BT, 50% BPD, and $PIDT_{C16}$-BPD_{C1} 9-mer optimized geometries from two perspectives: (a) from above the polymer backbone and (b) through the long axis of the polymer backbone. 42

Figure 2.5. (a) FSC heating thermograms comparing aged (black) and unaged (red) $PIDT_{C16}$-BT (top panel) and $PIDT_{C16}$-BPD_{C1} (bottom panel). Enthalpic overshoots (red highlighted areas) are observed when the aging temperatures (indicated on the right of the graph) were below the glass transition temperature of the materials. (b) Extrapolating the enthalpy recovery between aged and unaged samples of $PIDT_{C16}$-BT (top panel) and $PIDT_{C16}$-BPD_{C1} (bottom panel) allows for determination of the temperature at which the enthalpy overshoot is zero. This temperature correlates to the onset of the glass transition temperature. 45

Figure 2.6. Hole mobility data from OFET measurements (blue) and CoS (red) vs % BPD of each IDT copolymer. The 50% BPD, 75% BPD, 90% BPD, and $PIDT_{C16}$-BPD_{C1} samples were each extended to the limit of our strain stage (75% strain) without observed cracking. 47

Figure 2.7. The torsional potentials of the a) IDT-BT and b) IDT-BPD bonds. Edge-on views of the anti- and syn- conformers of the c) IDT-BT and d) IDT-BPD bonds. 51

Figure 2.8. 2D GIWAXS spectrum of each IDT-copolymer. The crystallographic plane of each signal has been labeled. 53

Figure 2.9. The d-spacing of the π-π (010), alkyl stacking (100), and interchain (001) signals from GIWAXS experiments. 53

Figure 2.10. The thickness normalized intensity of the π-π (010), alkyl stacking (100), and interchain (001) signals from GIWAXS experiments. 54

Figure 2.11. The coherence lengths from Scherrer analysis of the π-π (010), alkyl stacking (100), and backbone (001) signals from GIWAXS experiments. 54

Figure 2.12. Representative drain current versus gate voltage (IdVg) curves for each polymer system. 56

Figure 2.13. Temperature program followed for the aging of polymer samples conducted with Mettler Toledo Flash DSC 1. 59

Figure 2.14. Fast scanning calorimetry heating thermograms measured for $PIDT_{C16}$-BT (left) and $PIDT_{C16}$-BPD_{C1} (right) using 'aging' temperatures above the glass transition temperature. Two distinct endotherms appear when annealing samples above the glass transition temperatures, indicating possible liquid-crystalline or liquid-crystalline-like transitions. These occur at temperatures notably below room temperature (around 0 °C) for $PIDT_{C16}$-BPD_{C1}, while for $PIDT_{C16}$-BT the transition is around room temperature with a tail reaching 100 °C. 60

Figure 2.15. The $CHCl_3$ solution (blue) and thin-film (orange) UV-Vis (solid) and PL (dashed) spectra of each copolymer is shown. 61

Figure 2.16. ^{1}H NMR spectra of $PIDT_{C16}$-BT. 62

Figure 2.17. ^{1}H NMR spectra of 10% BPD. 63

Figure 2.18. ^{1}H NMR spectra of BPD 35%. 64

Figure 2.19. ^{1}H NMR spectra of BPD 50%. 65

Figure 2.20. ^{1}H NMR spectra of BPD 75%. 66

Figure 2.21. ^{1}H NMR spectra of BPD 95%. 67

Figure 2.22. ^{1}H NMR spectra of BPD 100%.....68

Figure 3.1. The structures of the BT-containing IDT copolymers which vary in the length of each side chain extending from the IDT monomer (left) and the TPD-containing IDT-copolymers which have the same side chains at the IDT monomer and vary in side chain character at the TPD-position. (right).....75

Figure 3.2. Linecuts of the 2D GIWAXS spectra in the Q_{xy} direction of each IDT-copolymer is shown. The (001) signal is labeled for clarity. 76

Figure 3.3. IDT-copolymers with side chains on only the IDT subunit (grey block) are able to interdigitate side chains and align in parallel (a) and IDT-copolymers with side chains on the IDT-monomer and TPD-monomer cannot interdigitate their side chains and therefore do not align in parallel (b).....77

Figure 3.4. Solution (a) and thin-film (b) UV-Vis spectra for each IDT-copolymer. 79

Figure 3.5. Enthalpic recovery curves of all IDT-copolymers with extrapolated T_g values. 81

Figure 3.6. The CMS spectra of the BT-containing IDT copolymers (a) and TPD-containing IDT copolymers are shown.....83

Figure 3.7. Representative stress-strain curves obtained through film-on-water elongation measurements for all IDT-copolymers except PIDT$_{C16}$-TPD$_{C1}$, which was too glassy to be tested. The colored 'X' on each line denotes fracture strain of each material for clarity. 84

Figure 3.8. Solution PL for all IDT-copolymers. 95

Figure 3.9. Fast Scanning Calorimetry of Annealed IDT series. Heating traces of annealed (black) and reference (red) lines IDT copolymers with annealing temperatures listed on the right side in increments of 10 degrees °C. PIDT$_{C16}$-BT copolymers show side-chain softening and liquid-crystalline-like melting peaks with annealing, while PIDT$_{C16}$-BPD$_{C1}$ copolymers show weak endotherms that indicate limited liquid-crystalline-like ordering, but no side-chain softening peaks. 96

Figure 3.10. Physical Aging of Planar IDT Copolymers. 97

Figure 3.11. Annealing and Aging Protocol for Side-chain crystal ordering. (left) Flash DSC annealing and aging protocol in create side-chain crystals and then age below the glass transition temperature (right) Flash DSC reference curves from annealing protocol. $PIDT_{C16}$-BT and $PIDT_{C16}$-BT_{C20} both show side-chain softening endotherms and liquid-crystalline-like melting endotherms. 98

Figure 3.15. 2D GIWAXS spectra for all polymer systems. 99

Figure 3.16. $PIDT_{C16}$-TPD_{C1} thin-film fractured before it could be loaded onto the strain stage. This occurred each of the twenty times it was attempted. 101

Figure 3.17. Representative OFET curve of $PIDT_{C16}$-BT thin films. 102

Figure 3.18. Representative OFET curve of $PIDT_{C20}$-BT thin films. 103

Figure 3.19. Representative OFET curve of $PIDT_{C16}$-TPD_{C1} thin films. 103

Figure 3.20. Representative OFET curve of $PIDT_{C16}$-TPD_{C8} thin films. 104

Figure 3.21. Representative OFET curve of $PIDT_{C16}$-TPD_{C13B} thin films. 104

Figure 3.19. ^{1}H NMR spectrum of IDT_{C20}. 105

Figure 3.20. ^{1}H NMR of $PIDT_{C16}$-BT. 106

Figure 3.21. ^{1}H HNMR spectra of $PIDT_{C20}$-BT. 107

Figure 3.22. ^{1}H NMR spectrum of TPD_{C8}-Br_2 108

Figure 3.23. ^{1}H NMR spectrum of TPD_{C13B}-Br_2. 109

Figure 3.24. ^{1}H NMR spectrum of $PIDT_{C16}$-TPD_{C1} 110

Figure 3.25. ^{1}H NMR spectrum of $PIDT_{C16}$-TPD_{C8} 111

Figure 3.26. ^{1}H NMR spectrum of $PIDT_{C16}$-TPD_{C13B} 112

Figure 4.1. BT-containing and TPD_{C13B}-containing TIF- and BTIDT-copolymer targets. 115

LIST OF TABLES

Table 2.1. BPD Incorporation Amount and SEC Data for Each Synthesized IDT Copolymer 38

Table 2.2 Ratios of monomers utilized during the synthesis of each IDT-copolymer system. 50

Table 2.3. Differences in energy between minima ($\Delta E_{syn\text{-}anti}$), the Boltzmann probability ratio of each conformer, and the barrier heights of rotation from each minimum ($Ea_{,rot}$) are reported. 51

Table 2.4 The CoS and μ_h for each IDT-copolymer. 56

Table 2.5. The reliability factor (rlin), on/off current ratio (Ion / Ioff) and threshold voltage (VT) is shown for each polymer. 56

Table 3.1 Size exclusion chromatography results for each polymer system. 75

Table 3.2 Optoelectronic properties of each IDT-copolymer system. 79

Table 3.3. The mechanical properties and $\mu_{,hole}$ of each IDT-copolymer are tabulated. 85

Table 3.4 OFET data is reported for all IDT-copolymers. 102

LIST OF SCHEMES

Scheme 2.1 Structure of Monomers and Resultant Random IDT Copolymers. 38

Scheme 3.1. Synthesis of BT-containing IDT-copolymers. 91

Scheme 3.2 Synthesis of TPD-containing IDT-copolymers. 93

Scheme 3.3 Synthesis of monomers TPD_{C8} and $TPD_{C13B.}$ 94

Scheme 3.4 Synthesis of monomer $IDT_{C20.}$ 94

Chapter 1. Introduction

1.1 Conjugated Polymers

Conjugated polymers (CPs) are polymeric material containing conjugation within their backbone repeat structure.[1] The conjugated backbone structure provides a long p-orbital network through which electrons can be delocalized.[2] Figure 1.1 displays how the growth of an extended π-bonding network through increased conjugation leads to the formation of Polyacetylene (PA) with band-like orbital structures. PA is the simplest conjugated polymer, consisting of only hydrocarbons with the molecular formula $(C_2H_2)_n$.[3] By increasing the conjugated length, there is an increase in the number of discrete occupied and unoccupied orbital energy levels. When the molecule grows large enough, the electronic behavior of the molecule becomes as if the discrete energy levels transition to band like valence band (VB) and conduction band (CB) structures.[4] These band like structures are analogous to that of inorganic semiconductors.[4] The gap between the highest occupied molecular orbital (HOMO) within the VB and the lowest unoccupied molecular orbital (LUMO) in the CB is the optical bandap (E_g).[5] The existence of the E_g is responsible for the semiconducting nature of CPs and is caused by the Peierls distortion.[6] Injection of charge carriers into a CP thin-film through chemical doping or application of a voltage can lead to the mobility of charge carriers within a CP thin-film.[7,8] As a result, conjugated polymers can be utilized as the charge transport layer in a wide array of electronic devices including organic field effect transistors (OFETs), sensors, organic solar cells, robotics, lighting and displays.

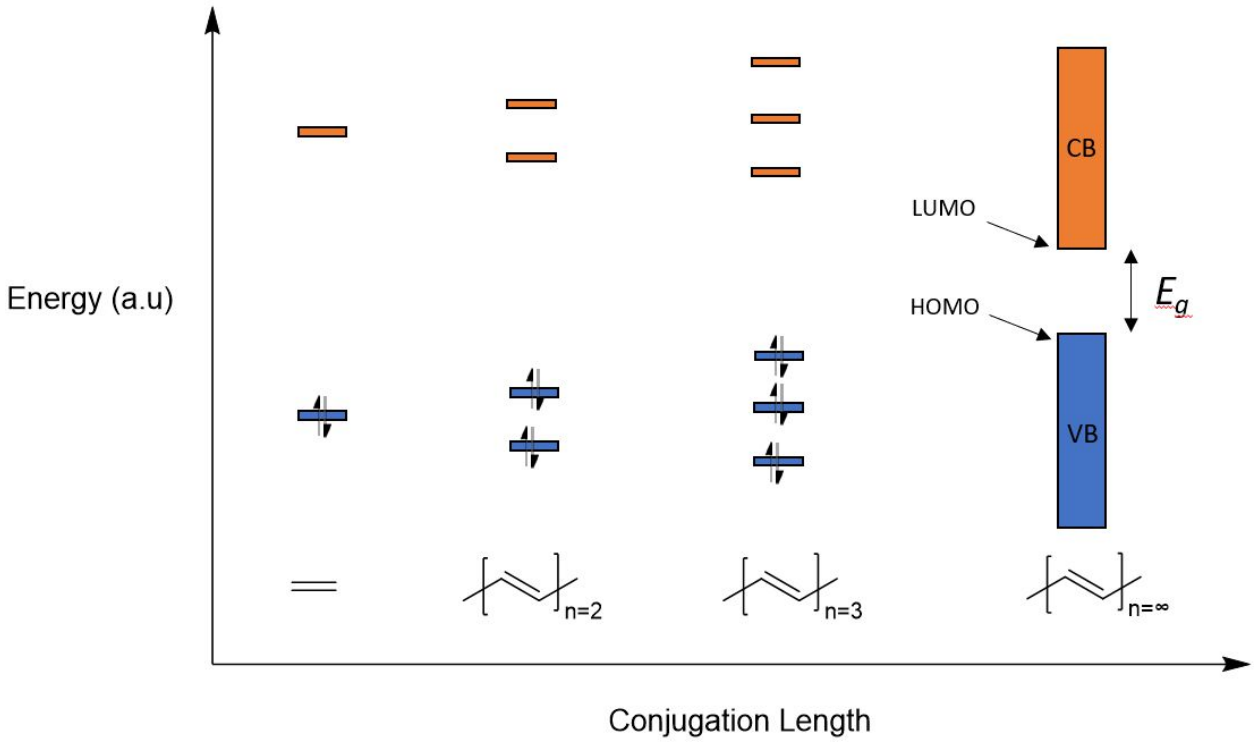

Figure 1.1. MO diagram for oligo-ethylenes and polyacetylene demonstrating the formation of bandlike structures due to increasing conjugation length.

CPs are typically incorporated into devices as thin-films cast from solution.[9] As a result, it is prudent to discuss how charges are transported throughout a thin-film. Figure 1.2 shows a schematic of charge transport along the backbone of an individual polymer chain (intra-molecular, blue arrow) and between the aromatic rings of distinct polymer chains (inter-molecular, red arrow). In such devices, charges must be transported to the drain electrode, which necessitates they travel up to hundreds of nanometers to reach electrode contacts.[10] This distance is longer than which than any single polymer chain in the thin-film. This necessitates that there must be pathways through which both intra- and inter-molecular charge transport must occur for a charge to reach the drain electrode.[11] Intra-molecular charge transport occurs when charge is transfer between aromatic units within the same polymer backbone. This is typically much more efficient than inter-molecular charge transport, which requires

π-π interactions between the aromatic units of neighboring polymer chains.[12] Intra-molecular charge transport is predominantly effected by the amount of torsion between monomer repeat units, with increasing torsion between repeat units leading to a decrease in intra-molecular μ,hole.[13] Inter-molecular charge transport is effected by the conformational properties of the chain as well as the amount of disorder within the thin-film microstructure and is considered the limiting factor in terms of the overall efficiency of charge transport within a conjugated polymer thin film.[12,14] Trap states are constituted of structural defects on a polymer chains, locations of local disorder, and interactions between polymer chains by O_2 and H_2O.[15,16] Charges that arrive at and occupy a trap state must overcome a now larger energy of activation in order to hop to an another position on the same chain or on an adjacent chain.[10,17] Decreasing the amount of energetic disorder within a polymer's thin-film microstructure can lead to increased charge mobility.[18,19] Altogether, charges move along their backbones until reaching chain ends where they must undergo intermolecular charge transport, continue through intramolecular charge transport along the new polymer backbone, and repeat this process until they reach the drain electrode.[20]

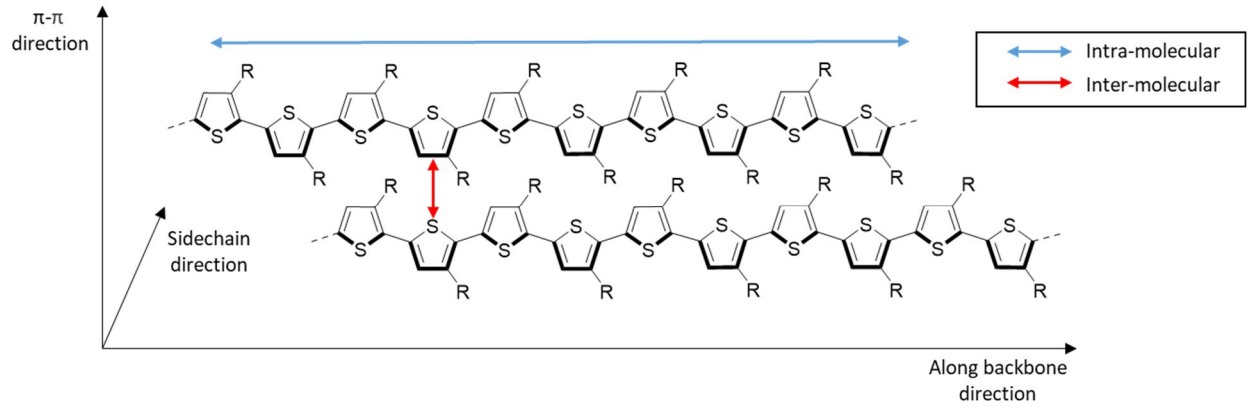

Figure 1.2. Schematic representation of two neighboring P3HT polymer chains, illustrating the direction of intra-molecular charge transport (blue) along the backbone and inter-molecular charge transport (red) between the conjugated rings of neighboring polymer chains.

Compared to organometallic semiconducting materials like amorphous or crystalline silicon, CPs have the distinct advantage of structural tunability due to their organic composition.[21] Conjugated polymers are comprised of a conjugated backbone structure, containing one or multiple unique repeating units as well as side chains that serve to solubilize the stiff and aromatic backbone.[22] Solubilization of the aromatic polymer backbone allows CPs to be solution processed for printed and large area electronics applications.[23,24] Modification and substitution of both monomer units and side chains of a CP can be used as a technique to modulate the mechanical and electronic properties of these materials.[16,25] Given their organic composition and structural tunability, physical properties of CPs can be achieved including being soft, lightweight, biocompatible, and transparent, while retaining their light-absorbing, light-emitting, and charge transporting properties.[26,27] Individual commodity polymers find their different industrial uses because of their unique mechanical properties. Like commodity polymers, CPs with different properties will be utilized in different plastic electronic applications. Because of this "right polymer for the right application" philosophy, the development of many different CP systems with varied mechanical and electrical properties is a valuable pursuit. For CPs to be commercialized as organic semiconductors they must leverage the qualities that differentiate them mechanically from organometallic semiconductors.

1.2 Conjugated Polymers as transport layer in OFET Devices

An organic field effect transistors (OFET) is a type of electronic device used to amplify weak signals or to switch electronic signals in logic circuits where the composition of the charge transporting layer is of organic small molecules or CPs.[8,28] Structurally, it is composed of a charge transporting layer, a dielectric layer, and three electrodes: a source, drain, and gate electrode. The structural schematic of a bottom-gate-top-contact (BGTC) OFET device is shown in Figure 1.3. An OFET can

be turned on by applying voltage to the gate electrode, which causes charge carriers to build at the interface between the dielectric and semiconducting layer.[24] When a voltage is applied between the source and drain electrodes, the accumulated charges will flow through the device in the source to drain direction.[28] When this occurs the transistor can be considered on.

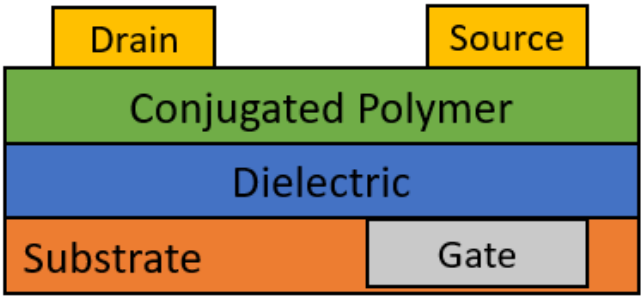

Figure 1.3. Schematic of a bottom-gate top-contact (BGTC) organic field effect transistor (OFET) consisting of a substrate (orange), gate electrode (grey), dielectric layer (blue), conjugated polymer semiconductor layer (green) and source and drain electrodes (gold).

The performance of an OFET is primarily assessed by measuring the mobility of a device. The mobility is the ability of a charge carrier to move through a device under an electric field and is measured in units of $cm^2\ V^{-1}\ s^{-1}$.[29] It also represents the proportionality constant between carrier velocity and an the given electric field.[30] CP-based OFETs can be n-type or p-type depending on their molecular structure and resulting HOMO and LUMO energy levels, but the development of p-type CPs has outstripped the development of n-type CPs.[31] Herein we will focus primarily on hole mobility ($\mu_{,hole}$), as the materials discussed in later chapters are p-type semiconductors themselves.

The most commonly utilized field effect transistor in commercial applications are metal-oxide semiconductor field effect transistors (MOSFETs), which commonly utilize amorphous silicon as their semiconducting layer.[28,32] Two main advantages of OFETs compared to amorphous silicon MOSFETs is potential low cost-processing and the tunable mechanical properties of CPs that unlock deformable

electronics applications. Deposition of amorphous silicon requires high temperature and vacuum conditions, while in contrast, CPs can be deposited through solution processing techniques including roll-to-roll printing.[33] Amorphous silicon is extremely brittle and has elastic moduli between few and several orders of magnitude larger than CPs.[34,35] The opportunity to leverage the solution processibility and mechanical properties of CPs in electronic devices has led to the development of deformable electronics which are more suited for dynamic mechanical environments than MOSFET based devices.[36]

Human-computer interactions are a routine part of the day for billions of people worldwide. We take these devices with us as we move, literally, through our day. Unlike our skin, which is flexible, stretchable, lightweight, soft and self-healing, our computers are brittle, rigid, heavy, fragile, and expensive to repair. Consumers go to great lengths to shield laptops and cell phones from mechanical damage, putting laptops in sleeves and padded backbones and phones in shockproof cases. We protect these devices because of the incompatibility between the mechanical properties of our devices and the dynamic means by which we go about our day. The next wave of computing development and invention will directly interact with the human body, which requires that these electronic devices be deformable in some capacity.[37] These deformable applications include soft-robotics, interfacial health monitoring, electronic skin, biosensors, and wearable internet of things devices.[38–43] These are applications which require the semiconducting material to bend and stretch as it conforms to the curvilinear human body.[27] Intrinsically stretchable CPs are a class of CPs that can withstand the stresses experienced in deformable electronics because of an intrinsic ability to dissipate stress through reorganization of their thin-film microstructure.[44] Many intrinsically stretchable systems low degrees of crystallinity that endows them with lower moduli and the qualities of being soft and more easily stretched.[27] In an effort to develop intrinsically stretchable CPs with mechanical properties more

compatible with human skin, the field is targeting materials with 100% fracture strain, a $\mu_{,hole}$ of 1 $cm^2\ V^{-1}\ s^{-1}$, and an elastic modulus less than 10MPa.[34] To date, the generation of intrinsically stretchable CPs with high fracture strain and $\mu_{,hole}$ has been achieved, but not with sufficiently low elastic modulus.[34] This is because increasing molecular weight is a known strategy to increase $\mu_{,hole}$ to promote more intra-molecular charge transfer and to increase elongation at break through the formation of entanglement, but at the cost of an increased elastic modulus.[45] To achieve materials with all three properties of interest, structural changes need to be made so that polymer systems that are not entangled can undergo deformation.

1.3 Mechanical property evaluation

In order to develop semiconducting materials suited for use in stretchable electronics, we must design CPs to have structural characteristics to existing CPs that aide them in deforming while under strain. To do so, it is necessary to understand how CP chains reorganize due to strain. A schematic of polymer chain reorganization due to strain is shown in Figure 1.4. Initially polymer backbones extend in all directions while participating in weak Van der Waals interactions.[10] When strain is applied, the polymer backbones undergo elastic deformation and align in the direction of strain.[46,47] When the strain is increased, polymer chains will begin to undergo plastic deformation if they are not inhibited from doing so by crystalline domains or interactions between polymer backbones.[48,49] As plastic deformation occurs, polymer chain slide past each other entirely which causes the formation of a microvoid through chain pullout.[50] It is around these microvoids, in the orthogonal axis to the strain, that stress is concentrated. As the film continues to stretch the microvoid grows until the film eventually ruptures.[51] Failure through chain pullout is the common damage mechanism for CP samples with M_n below their entanglement molecular weight (M_e) and at the boundary between crystalline and amorphous fractions of thin-films.[50] Samples with M_n above their entanglement molecular weight also

will undergo chain scission if enough entanglements exist between polymer chains in a sample.[52] CPs that are incapable of deforming plastically will dissipate stress only through elastic deformation before undergoing brittle failure. Brittle failure of thin-films can be observed by witnessing characteristic fracturing of the thin-film across the entire height of the film nearly instantaneously.[50] In contrast, CPs that are capable of plastic deformation undergo ductile failure.[50] Ductile failure can be observed by witnessing characteristic formation of microvoid pinholes whose aspect ratios grow, as a result of plastically deforming chains around them.[50] Endowing a CP with the ability to deform plastically allows it the ability to mechanically withstand strain and retain charge mobility, as brittle failure severs completely the electronic pathways between electrodes.

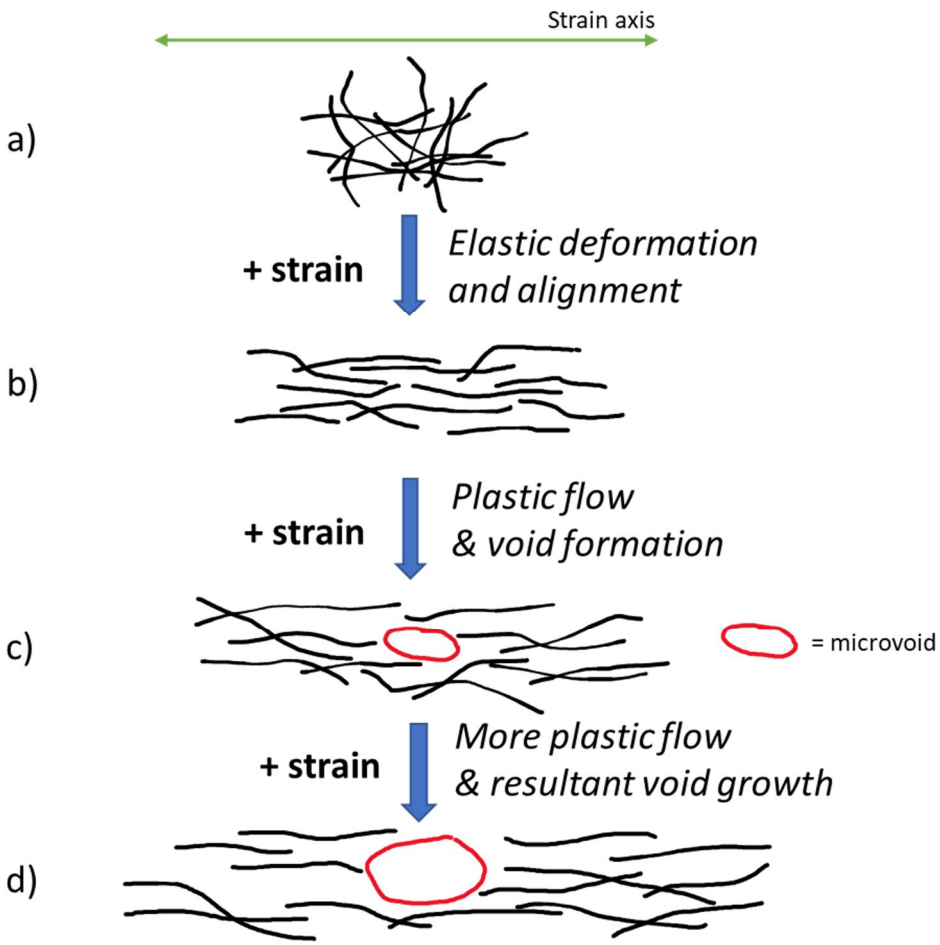

Figure 1.4. A schematic detailing the reorganization of polymer chains (black) beginning with initial strain (a) which causes elongation of the film through elastic deformation and chain alignment (b), followed by plastic flow if available to the system, which ultimately results in initial void formation (c) and void propagation that leads to rupture of the thin film (d).

Pull testing is a common means of assessing a CPs ability to undergo deformation. Elongation at break, the measure of a materials ability to elongate before mechanical failure, is an important metric that can be garnered through pull testing. Two common means of evaluating CPs in this regard are film-on-elastomer (FOE) and film-on-water pseudo free-standing tensile tests (FoW).[52] In FOE testing a CP thin film is transferred onto an elastomeric substrate, placed between cantilevers, and stretched. Typically, an optical microscope is used to determine the strain at which the thin film cracks, which is how the crack-onset strain (CoS), a measure of the elongation at break of the material, is determined.[53] FOE testing provides a means to evaluate the elongation at break of a thin-film, but it must be taken into account that the support of the elastomeric substrate leads to larger elongation break values compared to when CP thin films are measured on their own.[54]

FoW methods are deemed pseudo-free standing because the CP film rests on the surface of water, which is relatively frictionless.[54] FoW testing stages commonly allow for the measurement of stress while performing elongation. This allows for the generation of stress-strain curves of CP thin films. A representative schematic of a stress strain curve is shown in Figure 1.5.[55] Evaluating stress-strain curves are an informative and useful means by which to evaluate the mechanical properties of different CPs.[48] By evaluating stress-strain data, the elastic modulus, elongation at break, yield point, tensile strength, and other relevant properties can be obtained that allow for the development structure property relationships. Differences in these properties distinguish CP systems as suitable for stretchable electronics application or not.[55]

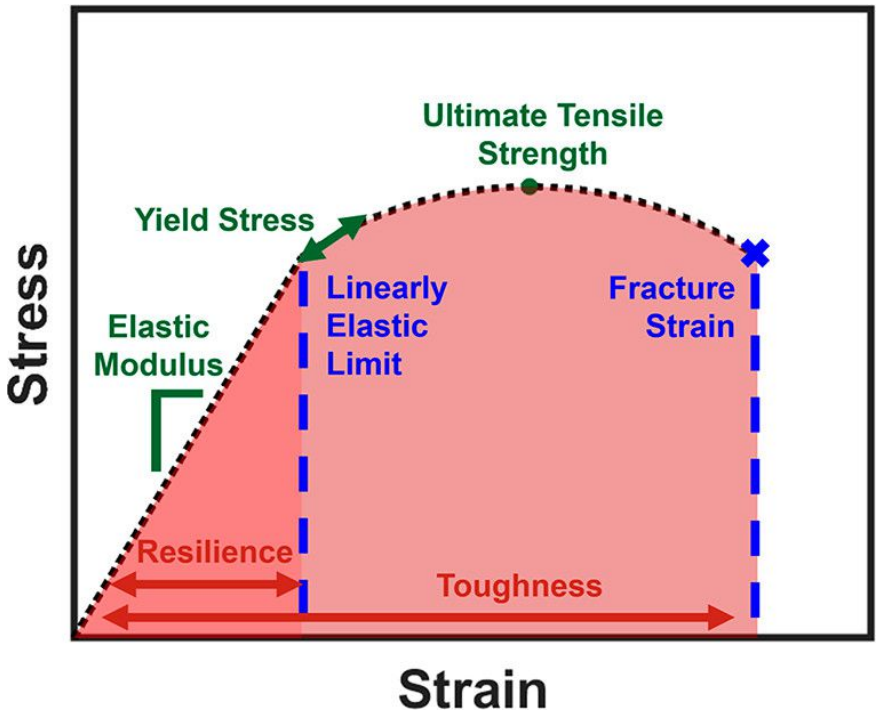

Figure 1.5. A generic stress–strain curve. Labeled are mechanical properties of interest associated with strain (blue), stress (green), and energy (red). The units associated with each, respectively, are generally given in % strain, MPa, and MJ/m^3. Reproduced from reference 55 with permission from the American Chemical Society.

1.4 A conjugated polymer paradigm: An overall relationship between polymer structure, conformational properties, thin-film microstructure, and the electromechanical properties of conjugated polymers

Having a paradigm to aide in the rationalization of the structure property relationships of conjugated polymers, which are effected by a myriad of factors, can be helpful in determining new relationships. Thus, the conjugated polymer paradigm works as follows (Figure 1.6): The chemical structure of conjugated polymers directly influences the conformational properties of the CP chains.[56–58] These conformational properties effect the intermolecular interactions between CP chains and thus

determine the nature of their solid state microstructure, which plays a significant role in determining the materials properties of conjugated polymer thin films and devices.[59,60] These four categories constitute the four grey blocks in Figure 1.6. Assessing the impact of structural changes on downstream grey qualities of a conjugated polymer in this linear fashion is necessary, but so too is assessing how each grey block impacts downstream and even upstream blocks. For example, increasing torsion between monomer units will directly impact the efficiency of intra-molecular charge transport and thus the $\mu_{,hole}$ of the thin-film (green arrow).[19,61] Also, changing the side chains of a conjugated polymer may not adjust the topological shape or coplanarity of the resultant polymer significantly, but may alter the packing structure between CP backbones (yellow arrow between chemical structure and solid state microstructure).[59,62] CP backbones have conformational properties like torsional potential energy landscapes that are modulated by the microstructural arrangement. For instance, amorphous poly-(3-alkyl)thiophene (P3AT) chains lack coplanarity, but are forced into more planar arrangements within the crystalline arrangements that they can form; an example of microstructural arrangements impacting conformation properties (red arrow).[63] Given the complexities of these relationships, the next three subsections will highlight the current relationships between chemical structure, conformational properties, solid-state microstructure, and materials properties that are relevant to the work described in Chapters 2 and 3.

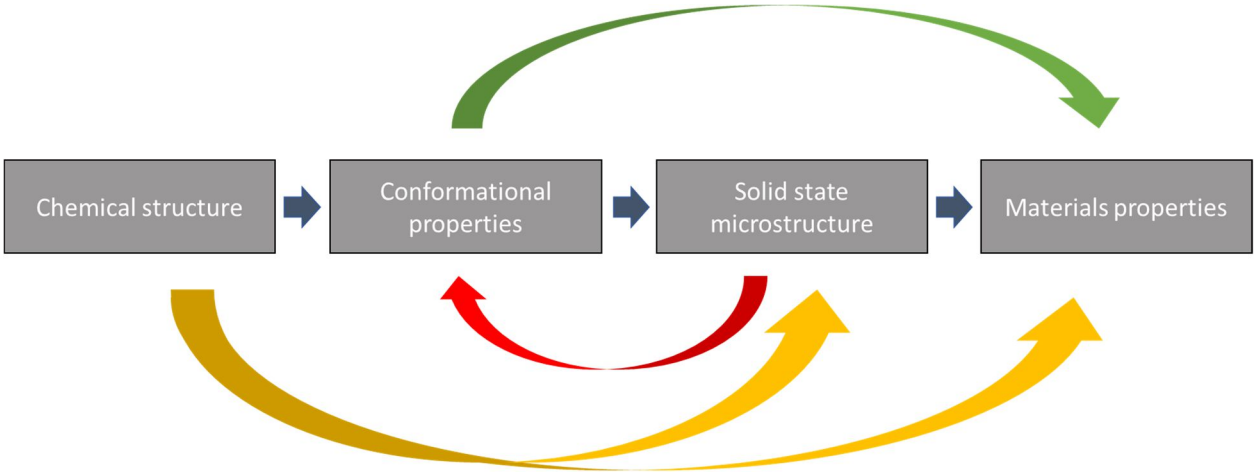

Figure 1.6. A visual representation of the conjugated polymer paradigm.

1.4.1 Chemical structure

CPs have conjugated backbones as well as solubilizing side chains. The backbone repeat structure is what separates CPs into classes. Figure 1.7, which has the structure of poly-(3-hexyl)thiophene (P3HT) and Poly(4-methyl-7-(4,4,9,9-tetrahexadecyl-7-methyl-4,9-dihydro-s-indaceno[1,2-b:5,6- b']dithiophen-2-yl)benzo[c][1,2,5]thiadiazole) ($PIDT_{C16}$-BT), illustrates the remarkable differences in chemical structure within this singular class of semiconducting materials. P3HT is a homopolymer, where the repeat unit is kept same throughout the backbone. It belongs to a family of CPs called poly(3-alklythiophenes) (P3ATs), within which the thiophene backbone motif is unchanged, but the solubilizing side chain that is covalently bound to the 3-position of every monomer is substituted.[64,65] $PIDT_{C16}$-BT is an alternating copolymer, where the conjugated backbone structure alternates between the indacenodithiophene (IDT) and benzothiadiazole (BT) monomer units. Since IDT_{C16} is a donor monomer and BT is an acceptor monomer, $PIDT_{C16}$-BT is a donor-acceptor copolymer (D-A CP).[66,67] D-A CPs have a donor monomer unit that is electron rich, and an acceptor monomer unit that is electron poor, which creates a HOMO-LUMO relationship in the D-A CP where

the HOMO energy level is closer to that of the donor unit, and the LUMO energy level is closer to that of the acceptor monomer.[68] This relationship facilitates more efficient charge transfer and extraction in OFETs.[16] The differences in side chain character between P3HT and $PIDT_{C16}$-BT is striking. In P3HT there is one side chain on every monomer repeat unit, while in $PIDT_{C16}$-BT there are four side chains that are each significantly longer than the side chains of P3HT on the IDT monomer, but the BT monomer is un-alkylated. Differences in the size, attachment density, and type side-chains (purely hydrocarbon or not) has direct impacts on the conformational, microstructural, and materials properties of conjugated polymers.[69–71] P3HT and $PIDT_{C16}$-BT have significant structural differences in both their aromatic repeat unit and side chains, yet both are conjugated polymers and can be utilized in similar application spaces. This necessitates the development of structure-property relationships for each individual family of CPs, rather than more generally for CPs as a singular class of materials.

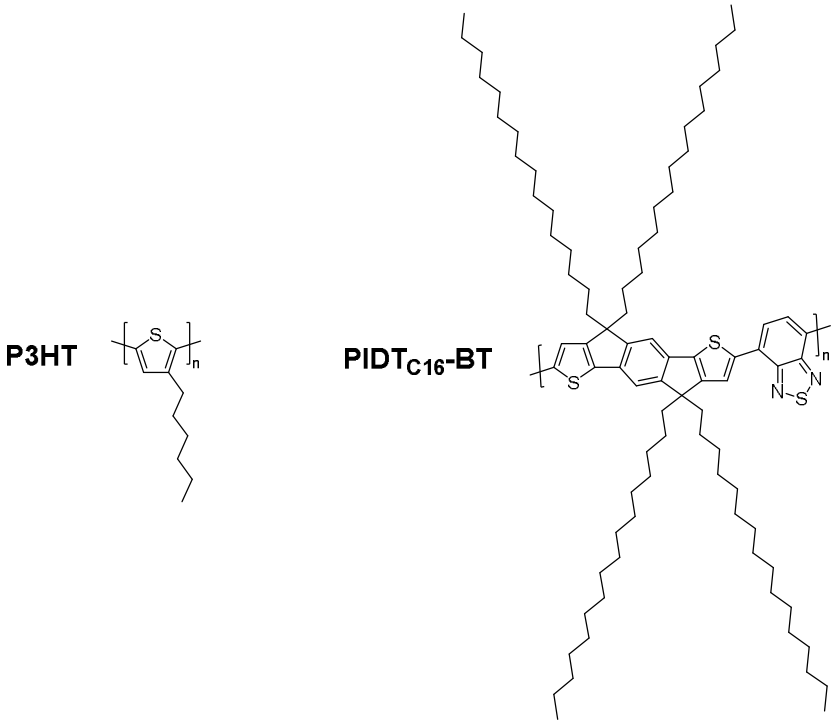

Figure 1.7. The chemical structures of P3HT (left) and $PIDT_{C16}$-BT (right).

1.4.2 Conformational properties

The conformational properties of conjugated polymers are primarily dictated by their molecular structure. Two important conformational characteristics are the backbone topology and coplanarity between monomer units. The backbone topology is determined by the persistence length (L_p) of the polymer.[72] The persistence length is intrinsic to each polymer system and is effectively a measure of the rigidity of a polymer backbone. If the length of a polymer chain, is significantly greater than the L_p, the polymer behaves topologically as if it were on a random walk, if the contour length is similar to the L_p, then it behaves like a semiflexible chain, and if the contour length is much smaller than the L_p, then it behaves like a rigid rod.[73] The topological behavior of the backbone can play a deterministic role in the microstructure of CPs in solid state by determining the M_e of a polymer and its ability to form intra-chain crystallites.[74]

CP systems differ in the coplanarity of the monomer repeat units within their backbone. This is due to their in their individual torsional potential energy wells which determine the dihedral angles their monomer-monomer bonds adopt.[58] This energetic landscape is determined by steric interactions between monomer units.[75] If the torsional potential energy well between the monomer units are centered close to 0° or 180°, the polymer backbone will be coplanar.[76] The further the wells are centered from 0° or 180° degrees then the less coplanar the polymer backbone units will be (Figure 2.1). The monomer-monomer bonds will occupy dihedral angles that are thermally accessible within their energy well; so the narrower the well, the tighter the distribution of occupied dihedral angles and less conformational disorder.[77] Co-planarity of the monomers within a CP correlates with $\mu_{,hole}$, as intramolecular charge transport is made easier due to the increased orbital overlap of neighboring aromatic units.[78] CPs with non-linear topologies and non-coplanar backbones can form entanglements

if above their M_e.[79] Entanglements provide points within a microstructure around which polymer chains unentangle, leading to an increase in elongation at break and tensile strength, but also in elastic modulus.[48] Thus, polymer systems with $M_n<M_e$ and thus no entanglement of polymer chains, may be more suitable candidate for soft electronics or e-skin.

1.4.3 Solid state microstructure

CPs are incorporated into OFET devices in the form of thin-films. These thin-films are typical cast from solution through spin-coating.[80] The CP is dissolved in volatile organic solvent, pipetted onto a substrate, which is then spun to remove the solvent leaving a thin-film of solid state CP. As the solvent evaporates the conjugated polymers attempt to adopt as stable a solid state microstructure as possible given the time it takes for solvent to evaporate. CPs will adopt varied degrees of order as they form a thin-film, as dictated by their conformational properties.[81] Figure 1.8 displays a schematic of CP microstructural ordering with varying degrees of crystallinity.[11] P3HT's conformational properties allow it to coil back on itself and form large crystalline regions,[82] but structural defects including variability in molecular weight ensure that there is a fraction of amorphous chains outside of those crystalline domains.[11] Inside crystalline domains, P3HT exhibits higher intra- and inter-molecular charge transport than amorphous chains because they are forced into coplanarity.[83] Because crystallites do not span the length of the device, longer molecular weight chains, called tie-chains must bridge crystalline domains to provide electrical connectivity to the thin-film (red lines in Figure 1.8).[84] This is why P3HT thin-films display a stepwise increase in $\mu_{,hole}$ once the molecular weight of the sample is high enough to enable the formation of tie-chains between crystallites.[84]

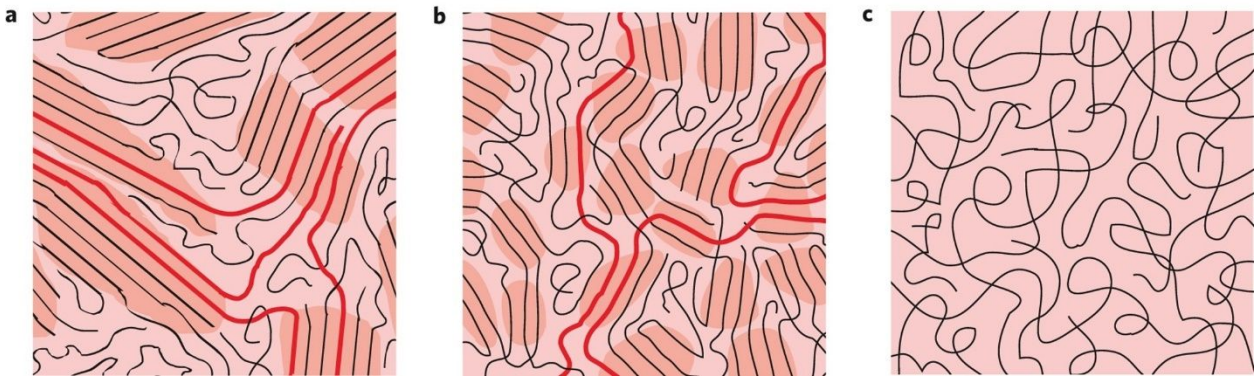

Figure 1.8. Schematics of the microstructure of a semicrystalline polymer film, for example P3HT (a) disordered aggregates (b) and a completely amorphous film (c). Reproduced from reference 11 with permission from Nature Publishing Group.

PIDT$_{C16}$-BT on the other hand is considered a near-amorphous CP.[85] Figure 1.9 displays a schematic drawing of rigid and semiflexible near amorphous morphologies. The schematic illustrates the effect of L_p on topology and thus on packing structure. Both are representations of near-amorphous microstructures because they lack long range order, but there is in each case intermolecular contacts where inter-molecular charge transport could occur. PIDT$_{C16}$-BT has an exceptionally long persistence length as a result of its colinear monomer bond arrangement and linearly fused IDT monomer.[73] As a result, it is expected that PIDT$_{C16}$-BT samples with a M_n less than about 200kg/mol arranges in a near-amorphous morphology represented by Figure 1.9a, rather than Figure 1.9b.[45] The four hexadecane side chains on each IDT monomer are the structural motif that inhibit π-π interactions between, and thus the crystallization of, polymer backbones in the (010) direction.[25] The large $\mu_{,hole}$*'s* observed for PIDT$_{C16}$-BT necessitates that some degree of π-π interaction occurs frequently enough to enable intermolecular charge transport, but not to the same degree of P3HT which has prominent x-ray diffraction signals in the (010) direction representative of long range π-π interactions.[86] CPs with near-amorphous thin-film morphologies hold more promise for use in stretchable electronics than other semicrystalline CPs, because they lack large crystalline domains which inhibit reorganization of

polymer backbones during deformation.[87] Still, not all polymers bearing near-amorphous thin films have exhibited ductile behavior, signifying that other interactions between polymer chains that cannot be deemed crystalline are inhibiting stress dissipation mechanisms.[53]

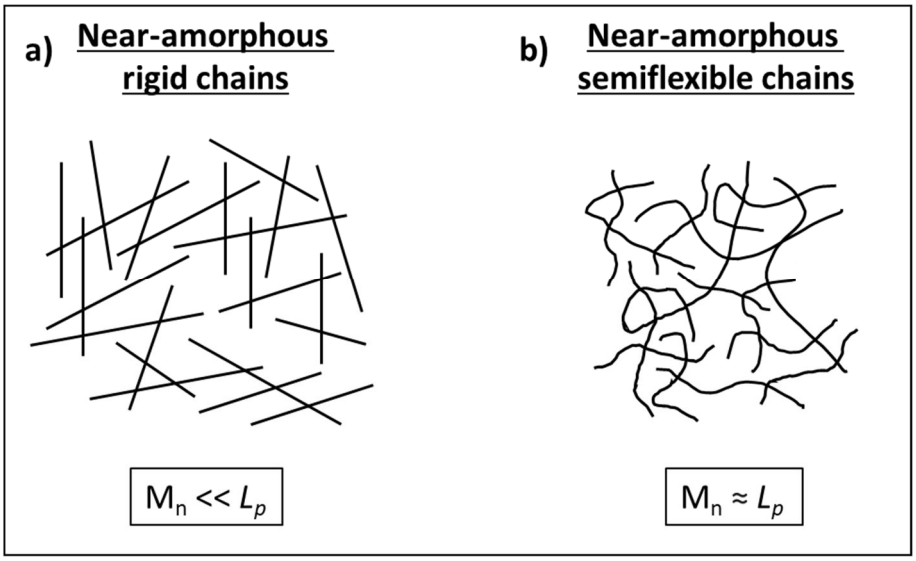

Figure 1.9. Schematic representations of near-amorphous thin film morphologies of rigid (a) and semiflexible (b) polymer chains.

CPs can display glass transition temperatures (T_g's) that represent a transition from polymer chains kinetically trapped in a glassy state (below T_g) and a non-glassy state in which polymer chains can flow past each other due to thermal activation. The T_g is an important parameter to consider for deformable electronics and is a signal of a CP's ability to reorganize its polymer chains during mechanical deformation. CPs with above room temperature T_g's and therefore glassy thin-films are not candidates for use in stretchable electronics due to their inherent brittleness.[57] However, CPs with sub-room temperature T_g's have significantly more potential to reorganize their microstructures during deformation.[48] Increasing the length of alkyl side chains, and thus the ratio of more flexible side-chain atom content relative to the more rigid backbone atom content, has proven a reliable strategy to

decrease the T_g of CPs.[57] Decreasing the T_g in this manner can lead to enhanced polymer chain mobility, granting resultant thin-films with longer elongation at breaks and decreased elastic moduli.[88]

1.5 Indacenodithiophene (IDT) copolymers

$PIDT_{C16}$-BT was first synthesized in 2010 by the McCulloch group.[89] It was discovered that this material had a $\mu_{,hole}$ of 1.0 $cm^2\ V^{-1}\ s^{-1}$ despite displaying only broad and diffuse crystallographic signals. These results countered the prevailing notion at the time within the field that long-range order was a requirement for high mobility.[25] Further investigation into the structure property relationships of $PIDT_{C16}$-BT revealed that the coplanarity of its polymer backbone endows it with exceptionally low energetic disorder, which promotes efficient charge transport.[85] $PIDT_{C16}$-BT thin films have since surpassed mobilities of 3.0 $cm^2\ V^{-1}\ s^{-1}$.[85]

Wadsworth et al. have recently published an excellent review on the impact of structural modifications on the charge mobility of PIDT-BT-based copolymers.[25] The four types of modifications covered in the review are shown in Figure 1.10.[25] When the IDT monomer's side chains were modified by shortening the alkyl chains and branch point introduction, the $\mu_{,hole}$ decreased in every case, relative to $PIDT_{C16}$-BT.[89] Fluorination of the BT monomer unit did lead to increased coplanarity due to the S-F interactions between neighboring conjugated monomers, but lead to decreased $\mu_{,hole}$ because of an increased amount of water induced traps.[90] The only modification that lead to an increase in $\mu_{,hole}$ was the extension of the IDT monomer fused ring core a new donor monomer called dithiopheneindenofluorene (TIF) monomer.[91] These studies provide useful insight into the importance of specific structural motifs on the determination of $\mu_{,hole}$, but the impact of structural changes on the mechanical properties of IDT-copolymers must be explored in greater detail.

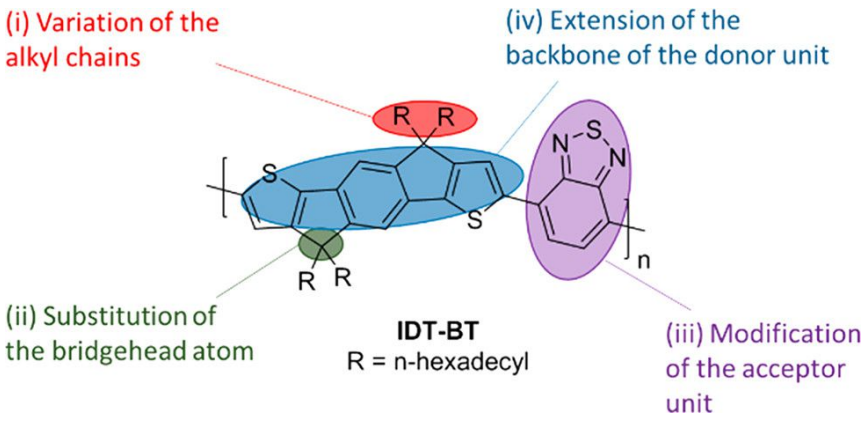

Figure 1.10. Basic design strategies for modification to the structure of IDT-BT. Republished from reference 25 with permission from the American Chemical Society.

Given their combination of near-amorphous microstructures, coplanar backbones, (true for many IDT-copolymers, but not all) and relatively linear topology (due to high L_p's), the relationships between structure and the mechanical properties of IDT-copolymers must be rationalized differently to other CPs. As is the case for any polymer system, the molecular weight plays a significant role in determining the mechanical properties of IDT-copolymers. Figure 1.11 demonstrates the effect of entanglement on the deformation of PIDT$_{C16}$-BT thin-films.[45] The M_e of PIDT$_{C16}$-BT appears to be just under 200 kg/mol,[45,92] which is quite large, yet expected for such a rigid polymer. Illustrating the effect of entanglement in PIDT$_{C16}$-BT polymers, low M_n (49 kg/mol) thin-films fracture at strains less than 2%, while ultra-high M_n thin films displaying entanglements fracture at 23% strain, and displays an elastic modulus of over 1000 MPa.[45] These results indicate that PIDT$_{C16}$-BT, while moderately stretchable at ultra-high M_n, is not intrinsically suited for e-skin or soft electronics applications due to its high elastic modulus.[34]

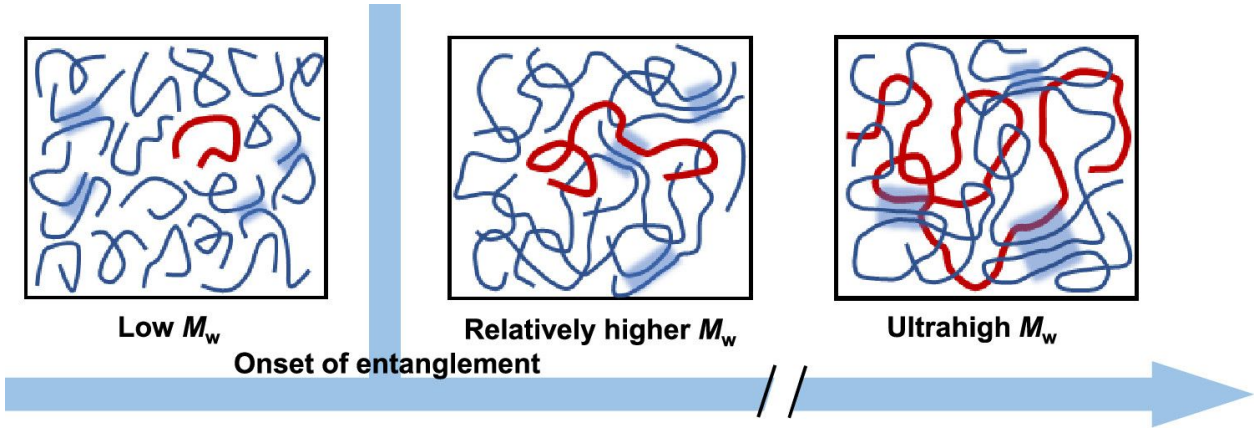

Figure 1.11. Schematic illustration of the film microstructure of IDT-BT with low M_w (left), relatively higher M_w (middle), and ultrahigh M_w (right), where the red chain in each illustration represents chains of specific M_w, and the aggregate structures are marked by the blue areas. Republished from reference 45 with permission from the American Chemical Society.

While the relationship between M_n and the mechanical properties of PIDT$_{C16}$-BT is well established, it is not the case that every IDT-copolymer has the same relationship. Poly(2-methyl-4-(4,4,9,9-tetrahexadecyl-4,9-dihydro-s-indaceno[1,2-b:5,6-b']dithiophen-2-yl)isoindoline-1,3-dione (PIDT$_{C16}$-BPD$_{C1}$) is an IDT copolymer with the BPD$_{C1}$ comonomer in place of the BT comonomer.[93] This monomer substitution leads to the introduction of torsion along the backbone. As a result of reduced backbone coplanarity, these PIDT$_{C16}$-BPD$_{C1}$ thin films exhibit *CoS* values of over 75% at M_n = 29 kg/mol,[53] which is larger than PIDT$_{C16}$-BT of nearly ten times greater M_n.[45] CPs with torsion between monomer units, especially ones that are beneath their M_e, often display brittle behavior under strain. The fact that IDT-copolymers can have such similar mechanical properties at drastically different chain lengths warrants the investigation into the impact of torsion on the deformation mechanisms of BPD$_{C1}$-containing IDT-copolymers. Chapter 2 of this work describes the synthesis of PIDT$_{C16}$-BT-r-BPD$_{C1}$ copolymers to assess how gradual introduction of torsion to the backbone of an IDT-copolymers effects its mechanical and electronic properties.

Poly(5-methyl-1-(4,4,9,9-tetrahexadecyl-4,9-dihydro-s-indaceno[1,2-b:5,6-b']dithiophen-2-yl)-4H-thieno[3,4-c]pyrrole-4,6(5H)-dione) ($PIDT_{C16}$-TPD_{C1}) is an IDT-copolymer derived through substitution of the BT comonomer with TPD_{C1}.[53] $PIDT_{C16}$-TPD_{C1} is more planar that $PIDT_{C16}$-BT according to density functional theory (DFT) calculations and has displayed $\mu_{,hole}$ equal to $PIDT_{C16}$-BT at similar M_n and processing conditions.[53] Like $PIDT_{C16}$-BT, $PIDT_{C16}$-BT is a brittle system at low molecular weight.[53] In contrast to the BT monomer, the sp^3 N-position on the TPD monomer possesses a synthetic handle to which side chains (other than methyl) can be attached. Because of this, it is possible to introduce more alkyl side chain character to TPD-containing IDT-copolymers. Chapter 3 of this work describes the side chain substitution on the IDT-monomer in BT-containing IDT-copolymers and on the TPD-monomer of TPD-containing IDT-copolymers. This was performed in an attempt to generate coplanar IDT-copolymers with a newfound ability to undergo plastic deformation during elongation and to probe the impact of side chain substitution on the conformational, microstructural, and materials properties of planar IDT-copolymers.

Chapter 2. Elucidating the Influence of Side-Chain Circular Distribution on the Crack Onset Strain and Hole Mobility of Near-Amorphous Indacenodithiophene Copolymers

*The work in Chapter 2 is adapted from a previously published article: *Macromolecules* **2020**, *53* (17), 7511–7518; DOI:10.1021/acs.macromol.0c00512.

2.1 Abstract

Poly(indacenodithiophene-benzothiadiazole) has received significant interest because of its exceptional hole mobility despite its near-amorphous thin-film morphology and brittleness at low M_n. In comparison, poly(indacenodithiophene-benzopyrollodione) ($PIDT_{C16}$-BPD_{C1}) has a lower hole mobility but is exceptionally ductile at similar M_n. Herein, we synthesize random indacenodithiophene (IDT) copolymers with varying amounts of incorporated benzothiadiazole and benzopyrollodione (BPD_{C1}), which introduces varied degrees of backbone twist to each respective polymer system. This allows us to elucidate how the BPD_{C1} monomer introduction leads to conformational and morphological changes that influence the crack onset strain (CoS) and hole mobility of these near-amorphous IDT copolymers and the rates by which each material property responds to sequentially larger BPD_{C1} incorporation. Results of density functional theory calculations suggest that BPD_{C1} introduction does not lead to significant differences in backbone linearity between the studied polymers, and grazing incidence wide-angle X-ray scattering demonstrates that the degree of crystallinity within thin films is not significantly altered. It does, however, lead to a more varied circular distribution of the hexadecyl side chains around the polymer backbone. With increasing BPD_{C1} incorporation, a crossover point between CoS and hole mobility emerges. At this crossover point, a random copolymer with 30% BPD introduction displays increased CoS and an average hole mobility

value equal to that of the $PIDT_{C16}$-BPD_{C1} system, suggesting that hole mobility is more sensitive to torsion along the polymer backbone, while the response of the CoS is relatively delayed. The data also suggest that the increase in CoS with increasing BPD_{C1} content does not arise because of differences in rigidity but because the more circular distribution of the side chains makes polymer chains with sufficient BPD_{C1} content better able to flow.

2.2 Introduction

π-Conjugated polymers (CPs) are being investigated as electronic components in a wide range of applications including organic field effect transistors (OFETs)[94] and organic photovoltaics.[95] The motivation for the usage of CPs in electronic devices includes their low mass density, solution processability, and compatibility with high-throughput manufacturing techniques.[36] Moreover, some CPs are suitable materials for use in deformable electronic devices because of their inherent mechanical properties and electronic properties.[48] Initially, it was believed that highly crystalline polymer films would be necessary to achieve efficient charge transport, and a significant effort was made to increase the degree of crystallinity of CP films.[70,96] A more recent understanding has uncovered that a long-range order is not strictly necessary [19] as CPs with low degrees of crystallinity and highly efficient charge transport along planar conjugated backbones have displayed mobilities in excess of 1 $cm^2 V^{-1} s^{-1}$. [97] These CPs fall into the class of near-amorphous CPs, forming only small local aggregates rather than larger crystallites.[98] The existence of local aggregates plays a crucial role in charge transport because they provide the necessary locations where interchain charge transfer can occur.[99] These highly amorphous systems that demonstrate high charge mobility are interesting as they may allow effective strain dissipation. [50,100] Near-amorphous CPs have, thus, the potential to strike a balance between mechanical properties and electronic properties, which makes them target polymers for deformable material applications, including wearable consumer and medical electronics. [37,61]

To warrant its use in a deformable device, a CP must display effective and robust electrical mobility and be able to withstand mechanical deformation. CP thin films are subjected to stress during deformation. As stress builds, polymer chains will attempt to dissipate stress incrementally by reorganizing into new conformations,[101] often aligning in the direction of strain before undergoing plastic deformation. [50] If the chains are prohibited from reorganizing because of the strength of intermolecular forces between polymer chains, then undissipated stress may be released through more sudden events such as chain pullout, [101] which can induce brittle failure of CP thin films. [50] Therefore, it is important to distinguish between the intermolecular forces that must be overcome to allow for reorganization of chains. Van der Waals interactions between the alkyl side chains of CPs are weaker and more easily overcome than interactions between rigid CP backbones, [102] which are considered load bearing.[48] The manifestation of this difference in strength on the ductility of CP materials is that backbone–backbone interactions inhibit reorganization of chains more than alkyl–alkyl interactions, which increases the likelihood of stress dissipation by chain pullout. Damage to the thin-film microstructure severs the electrical connection between polymer chains that necessarily span a thin film, leading to device degradation and ultimately failure.

To rationalize why mechanical differences exist between CP samples as a result of structural changes, it is important to gain insight into the conformation of these materials. Figure 2.1 illustrates two of the conformational factors, backbone linearity and twist (or conversely, coplanarity) between monomer units, which may vary between CP samples. CPs can be inhibited from reorganizing during deformation if their conjugated backbones are rigid, which is determined by the linearity of the conjugated backbone. CP chains that are less rigid have been shown to have a greater propensity to form kinks in their backbone, which increases their ductility because of entanglement.[103] The degree of coplanarity between monomer units in the backbone can also vary between polymer samples

because of differences in the torsional potential energy curves between different bonds. Greater twist between monomer units can inhibit intermolecular interactions between polymer backbones but does not preclude chains from being linearly extended.

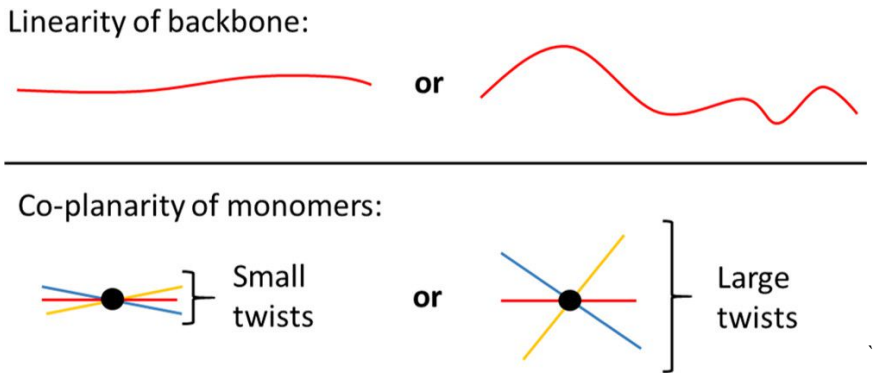

Figure 2.1. Topological drawings of polymer chains, shown in red, that are relatively linear and nonlinear (top). Drawings of trimers viewed down the long axis of the polymer backbone with different degrees of coplanarity between monomer units because of varying magnitudes (small or large) of twist between monomer units (bottom). Red, yellow, and blue lines represent the conjugated rings of separate monomers.

The solid-state structure of CP thin films also plays a role in determining the ability for polymer chains to deform. Characteristics of thin-film morphologies are affected by the size, shape, and distribution of solubilizing side chains attached to the polymer backbone.[104–106] For instance, it has been shown that introducing twist to polymer backbones decreases the number of interactions between polymer backbones during deformation, which leads to softer and more deformable materials.[107]

Crack onset strain (CoS) measurements provide a means to evaluate the ability for a polymer thin film to be extended before significant damage occurs. A polymer with a larger CoS displays a greater ability to be extended to larger strains before experiencing bulk failure.[108] In previous investigations, we had shown that two near-amorphous indacenodithiophene (IDT) copolymers, poly(indacenodithiophene-benzothiadiazole) ($PIDT_{C16}$-BT, frequently referred to as IDTBT) and

poly(indacenodithiophene-benzopyrollodione) ($PIDT_{C16}$-BPD_{C1}), display markedly different mechanical properties while maintaining good charge mobility.[53] Specifically, the CoS of $PIDT_{C16}$-BT and $PIDT_{C16}$-BPD_{C1} was found to be 7 and >75%, respectively, despite having only marginal differences in their crystallinity profile.[53] Without differences in the crystalline volume fraction to point to as the reason for major differences in the CoS between these materials, the difference between $PIDT_{C16}$-BT and $PIDT_{C16}$-BPD_{C1} is likely resultant from variations in other factors, such as differences in polymer backbone conformation and the overall solid-state structure that alter the material's ductility. Synthesis of random copolymers with varying amounts of the BPD monomer can allow us to ascribe changes in conformation because of gradual BPD incorporation to other factors that determine the material properties of CP thin films, which ultimately govern the hole mobility and CoS.

In this work, we synthesized a series of random IDT copolymers by varying the amount of benzothiadiazole (BT) and benzopyrollodione (BPD) comonomers. The incorporation was varied from 0 to 100% BPD content. This has allowed for a better understanding of why $PIDT_{C16}$-BT and $PIDT_{C16}$-BPD_{C1} have markedly different material properties. As a result of BPD_{C1} incorporation, the colinearity of the polymers remains unchanged but the hexadecyl side chains are more circularly distributed surrounding the polymer backbone in comparison to the side chains of $PIDT_{C16}$-BT which are extended in specific directions. Our results indicate that the change in ductility in these IDT-containing polymers is likely not due to changes in polymer backbone rigidity but is instead resultant from alterations in local side-chain distribution which is made more circular as the BPD monomer is incorporated.

2.3 Results and Discussion

Direct arylation polymerization was performed to synthesize a series of random IDT copolymers (Scheme 1). By varying the feed ratios of comonomers BT and BPD while maintaining the IDT content (Table S1), we synthesized several polymers with IDT–comonomer distributions

ranging from $PIDT_{C16}$-BT (no BPD comonomer) to $PIDT_{C16}$-BPD_{C1} (only BPD comonomer). Incorporation of each monomer in the final polymer was assessed by ^{1}H NMR analysis (Table S5). Each random copolymer was named based on its BPD incorporation ratio; as such, the investigated polymer samples were named $PIDT_{C16}$-BT, 10% BPD, 35% BPD, 50% BPD, 75% BPD, 95% BPD, and $PIDT_{C16}$-BPD_{C1}. Each polymer sample was analyzed by size exclusion chromatography (SEC) to evaluate its number average molecular weight (M_n) and dispersity ($Đ$). The results of this analysis are shown in Table 1.

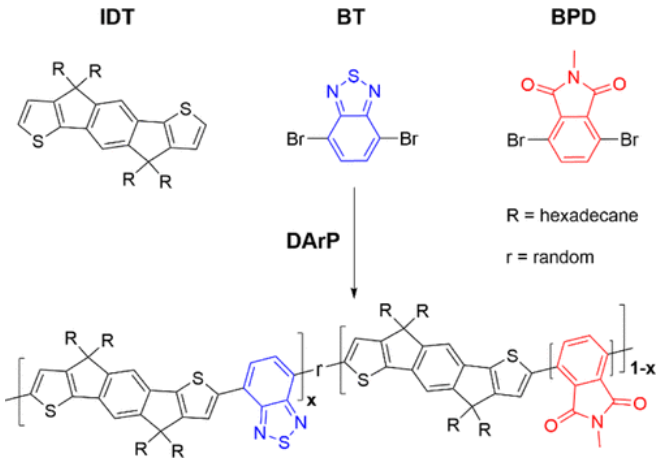

Scheme 2.1. Structure of Monomers and Resultant Random IDT Copolymers.

Table 2.1. BPD Incorporation Amount and SEC Data for Each Synthesized IDT Copolymer

BPD % by ^{1}H NMR	M_n (kg/mol)	$Đ$ (M_w/M_n)
0	9	1.6
10	10	1.7
35	11	1.6
50	14	1.8
75	18	1.8
90	18	2
100	29	1.8

With the polymers synthesized and monomer incorporation ratios and molecular size information having been established, we began to characterize the properties of each IDT copolymer, beginning with its optoelectronic properties. To do so, the polymers were subjected to ultraviolet–visible light absorption (UV–vis) and photoluminescence (PL) spectroscopy. Experiments were performed on both dilute solutions and spin-coated thin films, using chloroform as the solvent in both cases. Shown in Figure 2.2 are the thin-film UV–vis and PL spectra of all copolymers. In agreement with our previous studies,[53] the $PIDT_{C16}$-BT homopolymer displays an absorbance profile at much higher wavelengths than $PIDT_{C16}$-BPD_{C1} because of its coplanar conjugated backbone. In both the $PIDT_{C16}$-BT and 10% BPD samples, a vibronic transition is readily apparent. Only one transition is observed in the solution spectra of any sample (Figure 2.15). The red-shifted peak at 670 nm is likely the 0–0 transition resultant from highly planar $PIDT_{C16}$-BT chains that, due to aggregation, display greater J-type behavior in their absorption profiles.[109] Only one transition is observed for the 35% BPD sample and beyond. J-type aggregation behavior and effective conjugation length of the polymer can be reduced when polymer backbone planarity is reduced. Thus, the observance of only one peak for the greater than 35% BPD samples could be due to the incorporation of BPD_{C1} which could generate a twist between monomer units. The backbone twist is discussed later in the paper. The PL of the polymer systems gradually blue-shift as BPD_{C1} is incorporated. The blue shift between the 95% BPD sample and $PIDT_{C16}$-BPD_{C1}, in contrast, is much larger than the blue shifts between random copolymers. $PIDT_{C16}$-BPD_{C1}, having no BT monomer, emits at a much smaller wavelength than any sample with BT. This may be derived from favorable delocalization of excitons to BT monomers on the polymer chain, which causes emission to occur from that position most frequently. The blue shift of the PL maximum for the random copolymers may be caused by shifts in BT energy levels as a result of having neighboring BPD units in the polymer chains.

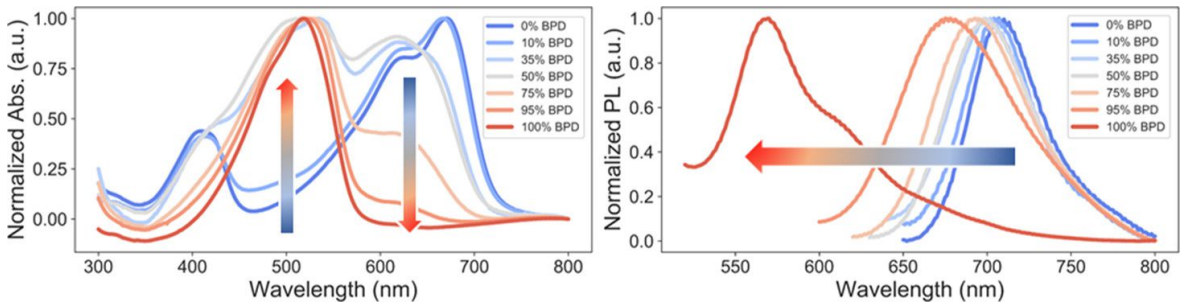

Figure 2.2. Thin-film (a) UV–vis absorbance and (b) PL data of all IDT copolymers.

Grazing incidence wide-angle X-ray scattering (GIWAXS) was performed to probe the crystallite d-spacings, crystallite orientations, and crystallite coherence lengths of each copolymer. The raw 2D GIWAXS spectra are shown in Figure 2.8. Although all samples are near-amorphous in terms of their overall solid-state structure, there are observable differences between the crystallographic features arising from these low-crystallinity materials. By observing these differences and rationalizing why they occur, inferences can be drawn about the conformational properties of each polymer sample. All copolymers show a mixture of face-on and edge-on orientation of polymer crystallites, evident by the appearance of both the side-chain (h00) and π–π diffraction peaks (010) in the out-of-plane direction. The (h00) and (010) peaks in all samples appear diffuse and broad, suggesting the highly disordered, amorphous-like nature of the polymers under investigation (Figure 2.8). The thickness-normalized diffraction intensity of the (010) signal (extracted from vertical linecuts), which arises from π–π stacking between polymer backbones, remains effectively constant throughout the spectrum (Figure 2.9). The π–π d-spacing between the crystallites rises steadily with BPD_{C1} incorporation from 35% BPD onward; from about 0.41 to 0.44 nm for 70% BPD and $PIDT_{C16}$-BPD_{C1}, respectively (Figure 3a). The 0.41 nm (010) d-spacing distance has been observed for $PIDT_{C16}$-BT previously.[98] Notably, in samples with high BT content, we observe a characteristic rod-like diffraction peak (001) near q ~ 0.4 A–1 corresponding to diffraction from the polymer backbone. The (001) peaks are observed

predominantly in the in-plane direction, indicating the highly in-plane orientation of the polymer backbone for all samples. Upon increasing BPD_{C1} content, there is also a steady decline of both the intensity and coherence length of the (001) signal (Figure 3b,c). The (001) signal is the along-backbone diffraction and arises when conjugated chain segments are coplanar,[85] either by their intrinsic conformational properties or through induced coplanarity because of aggregation with other chains.[110] This signal has been observed for rigid polymers, including $PIDT_{C16}$-BT, and has been shown to disappear because of increased twist between monomer units in the backbone.[60] The first significant change in intensity and coherence length of this peak relative to $PIDT_{C16}$-BT occurs at 35% BPD incorporation. The signal is greatly diminished in the 50% BPD sample and continues to decrease as BPD_{C1} is further incorporated. The observed changes in both the (010) and (001) signals, as a result of BPD_{C1} incorporation, signify that by increasing the twisting between monomer units along the polymer backbone, there is more space between them and that polymer chains become less coplanar.

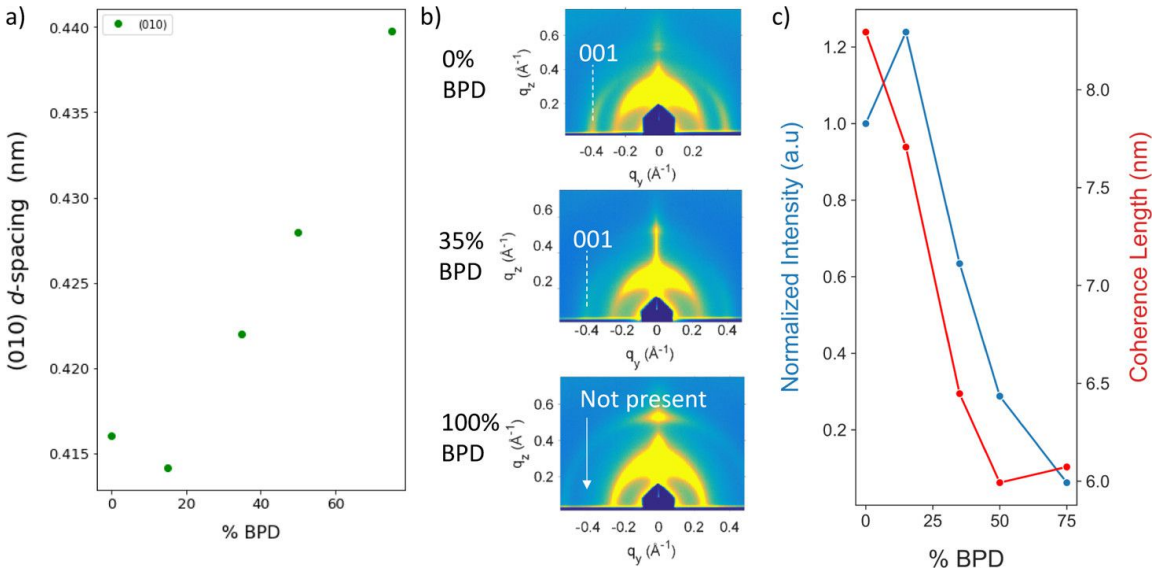

Figure 2.3. (a) (010) *d*-spacings, (b) zoomed-in regions of the raw-GIWAXS data, and (c) the normalized intensity and coherence length of the (001) backbone reflection signal.

With knowledge that BPD incorporation alters the microstructure of these IDT copolymer systems, the structures of three IDT copolymers were simulated to elucidate how incorporation of the BPD monomer would impact the conformations of polymer chains. Each polymer was modeled to have five IDT repeat units and a total of four BT and/or BPD units, as shown in Figure 2.4. The hexadecyl side chains on IDT have been replaced with ethyl groups, which are sufficiently long to accurately simulate the torsional potentials between monomers.[111] The chains in Figure 2.4 are in the favored all-anti configuration and as such will be the most linearly extended form of the polymer as the net direction of backbone deflection angles sum to zero.[72] Density functional theory (DFT) simulations suggest that this is appropriate as analysis of the potential energy of the torsional potential wells of each bond show that both polymers have a large preference for their anti-configuration (Figure 2.7). As a result, the low M_n chains are anticipated to display only anti-linkages, be linearly extended and not entangled, and therefore be rigid (Table 2.3).[72,111] Based on these results, we propose that the difference in CoS between PIDT$_{C16}$-BT, PIDT$_{C16}$-BPD$_{C1}$, and of the random copolymers should not be attributed to differences in backbone rigidity and thus entanglement, despite their differences in M_n.

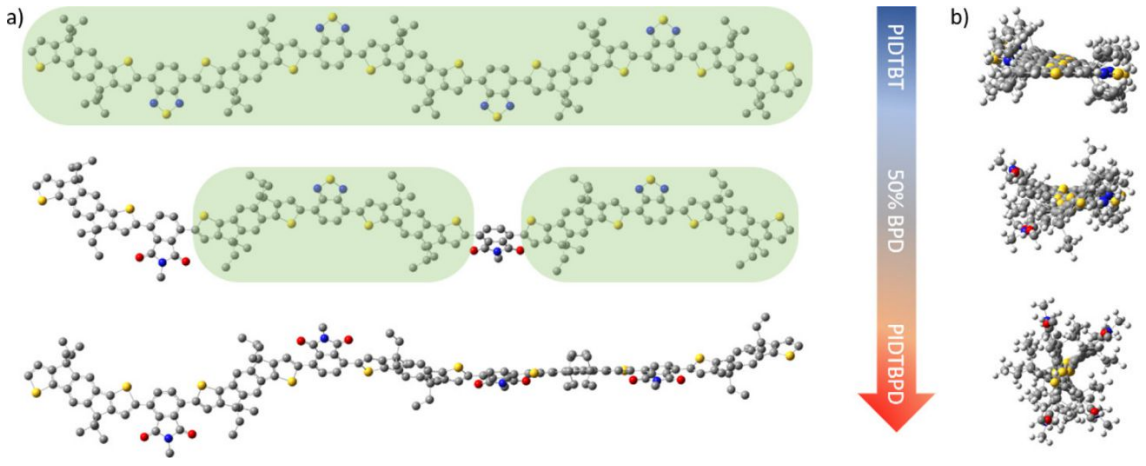

Figure 2.4. Density functional theory calculations of PIDT$_{C16}$-BT, 50% BPD, and PIDT$_{C16}$-BPD$_{C1}$ 9-mer optimized geometries from two perspectives: (a) from above the polymer backbone and (b) through the long axis of the polymer backbone.

There is a larger dihedral angle between IDT–BPD linkages compared to IDT–BT, which imparts a twist to the polymer backbone. The impact of induced change is evident in the 50% BPD 9-mer with two BT and two BPD_{C1} comonomers and is further exacerbated in $PIDT_{C16}$-BPD_{C1} which twists more aggressively. Although repeat units of IDT–BT–IDT (Figure 2.4a, highlighted in green) remain planar in the simulated 50% BPD_{C1} sample, BPD_{C1} monomer units interrupt this planarity between the conjugated rings and twist the planar segments out of plane from each other. This is proposed to be the reason behind the reduction in the (100) crystallographic signal intensity and coherence length. Because of increased twist along the backbone, charge transport will weaken,[112] unless the planar segments that do exist provide enough regions of sufficient planarity for long-range transport along the backbone, bolstering the mobility despite this conformational change. The planar segments may also provide locations for favorable interactions between where strong electronic coupling between chains may form, giving rise to intermolecular charge transport.[113]

Twist between IDT–BPD monomers along the polymer backbone also alters the circular profile by which side chains extend away from the polymer backbone. As can be viewed by looking down the long axis of the polymer backbone (Figure 2.4b), the side chains of $PIDT_{C16}$-BT extend in a more organized pattern compared to the side chains of $PIDT_{C16}$-BPD_{C1}, where the side chains extend away from the backbone across a larger range of angles. These side chains form a cylindrical tube that extends over the length of the polymer backbone. Increased shielding of the polymer backbone by alkyl side chains has been shown to decrease the occurrence of interactions between stiff backbones, favoring instead interactions between alkyl side chains, of non-CPs.[102] Greater disorder in side-chain extension has been shown to increase the elongation at break of thin films.[114] Incorporation of the BPD_{C1} monomer and the resultant change in the side-chain extension profile may disrupt $PIDT_{C16}$-

BPD_{C1}'s ability to exhibit interactions between polymer backbones during deformation,[105] relative to $PIDT_{C16}$-BT, thus improving the ductility of $PIDT_{C16}$-BPD_{C1} thin films.

Fast scanning calorimetry (FSC) was performed to determine the thermal behavior of our polymer systems, focusing on the homopolymers $PIDT_{C16}$-BT and $PIDT_{C16}$-BPD_{C1}, as it is known that important mechanical properties of polymers strongly depend on thermal transition temperatures such as glass transition temperature (T_g) and melting temperatures (T_m).[115] The T_g values of fully vitrified $PIDT_{C1}$-BT and $PIDT_{C16}$-BPD_{C1} were determined measuring the enthalpic relaxation overshoot of the amorphous phase of the films after physical aging (Figure 2.5).[116,117] Both polymers display a very comparable T_g (10 °C and 8 °C for $PIDT_{C16}$-BPD_{C1} and $PIDT_{C16}$-BT, respectively). Accordingly, IDT copolymers comprising BPD_{C1} moieties can be expected to have T_g's in the same temperature regime.

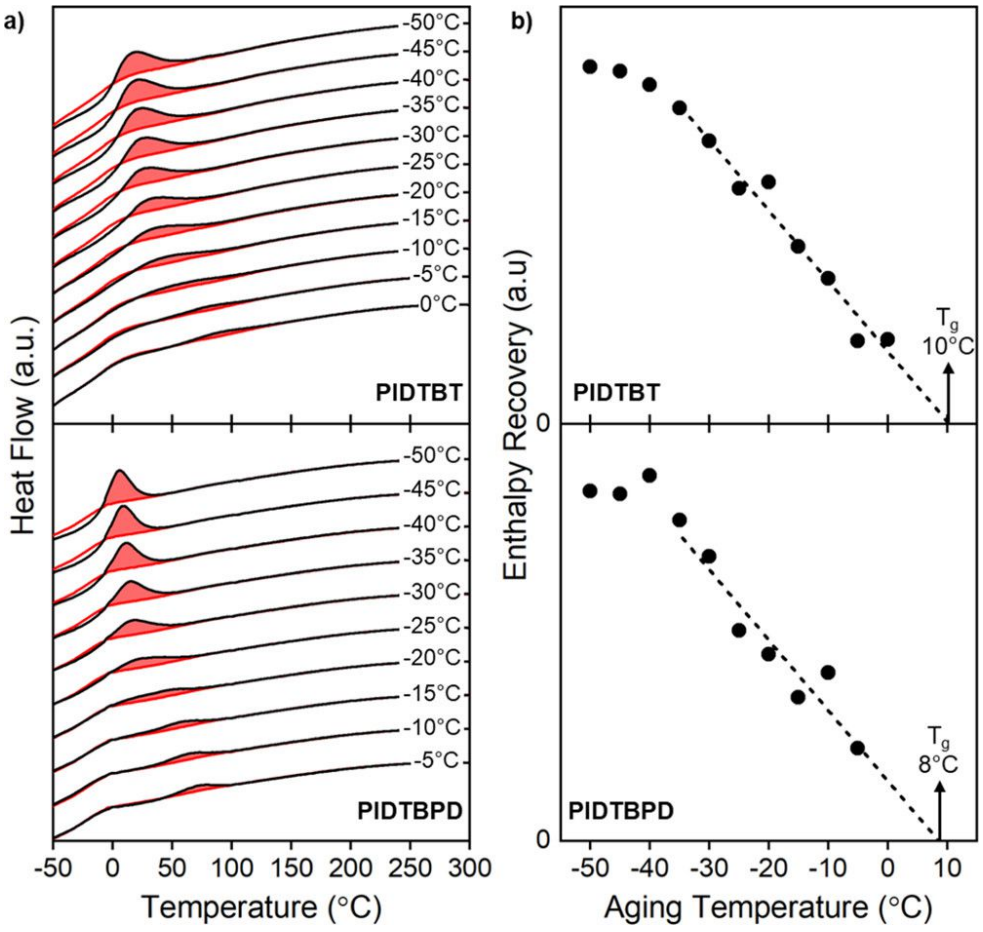

Figure 2.5. (a) FSC heating thermograms comparing aged (black) and unaged (red) $PIDT_{C16}$-BT (top panel) and $PIDT_{C16}$-BPD_{C1} (bottom panel). Enthalpic overshoots (red highlighted areas) are observed when the aging temperatures (indicated on the right of the graph) were below the glass transition temperature of the materials. (b) Extrapolating the enthalpy recovery between aged and unaged samples of $PIDT_{C16}$-BT (top panel) and $PIDT_{C16}$-BPD_{C1} (bottom panel) allows for determination of the temperature at which the enthalpy overshoot is zero. This temperature correlates to the onset of the glass transition temperature.

Considering their T_g's, these materials would be expected to soften at room temperature. However, it is important to note that two distinct endotherms appear when annealing the polymers above their T_g's (rather than aging below T_g; Figure 2.5). The presence of these enthalpic overshoots (compared to pristine samples) suggests possible liquid-crystalline or liquid-crystalline-like transitions, assisted by side-chain softening. Indeed, the lower temperature endotherms are reminiscent of sub-T_g transitions of CPs attributed to side-chain motion.[118,119] This process seems to occur at temperatures notably below room temperature (around 0 °C) for $PIDT_{C16}$-BPD_{C1}, while for $PIDT_{C1}$-BT, the transition is around room temperature with a tail reaching 100 °C, not unlikely to affect their mechanical behavior. The investigation of the physical origin of the observed thermal transitions is a subject of future study.

To evaluate how incremental substitution of the BPD_{C1} unit impacts electrical properties, OFETs were fabricated using each polymer system as the transport layer. The detailed results of OFET characterization are shown in Table 2.4 and Table 2.5, and several sample transfer curves are shown in Figure 2.12. As can be seen in Figure 2.6 in blue, the hole mobility immediately decreases with 10% BPD_{C1} incorporation, followed by a decline to nearly that of $PIDT_{C16}$-BPD_{C1} at a level of only 35% BPD incorporation. The 95% BPD sample has a lower mobility than that of $PIDT_{C16}$-BPD_{C1}. This is

likely caused by the small amount of BT monomer contributing little in the way of planarizing the molecule and only detrimentally acting like a structural defect. We ascribe the immediate decline in mobility to the increased twist between monomer units which weakens the electronic coupling between adjacent conjugated rings, thereby decreasing the efficiency of intramolecular charge transport.[120] As the BPD_{C1} monomer is further incorporated into the backbone, charge transport along the backbone worsens. The distance between π–π interactions in local aggregates also lengthens, as evidenced by the increase in (010) d-spacing beginning at 35% BPD_{C1} incorporated and beyond, making intermolecular charge transfers less efficient.[56] Both effects contribute to the rapid decline of hole mobility and stem directly from the impact of the large twist between IDT and BPD units. The 9-mer DFT structural optimizations suggest that planar IDT–BT–IDT repeat units would remain in random copolymers, but the magnitude of hole mobility for the 35% BPD sample and the fact that the normalized intensity of the (010) π–π stacking signal is not significantly different across all samples, demonstrate that charges must be transported along coplanar chain segments of greater length, longer than those that exist in the 35% BPD samples, to retain the hole mobility of $PIDT_{C16}$-BT.

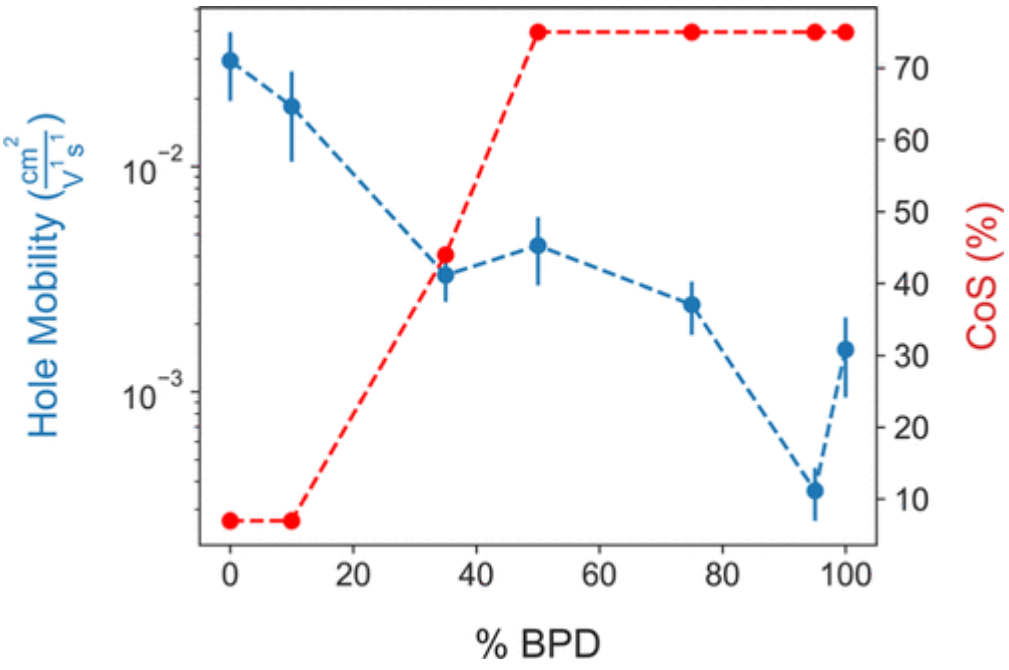

Figure 2.6. Hole mobility data from OFET measurements (blue) and CoS (red) vs % BPD of each IDT copolymer. The 50% BPD, 75% BPD, 90% BPD, and PIDT$_{C16}$-BPD$_{C1}$ samples were each extended to the limit of our strain stage (75% strain) without observed cracking.

CoS testing was performed to evaluate the elongation at break of thin films made using each polymer. The results are shown on the red curve of Figure 2.6. The 10% BPD sample has an equivalent CoS to that of PIDT$_{C16}$-BT, signifying that the ductility of the polymer sample is not as sensitive to random incorporation of BPD$_{C1}$ as the electronic properties are. The 35% BPD sample, however, displayed a larger CoS of 44%. Because analysis of the DFT simulations of torsional potentials suggests that the polymer chains are expected to be linearly extended and the initial change in CoS occurs between polymers of similar M_n, this rise is likely affected by the twist between monomer units alone, rather than a difference in linearity or M_n. This conformational change was shown to impact the profile by which alkyl side chains extend away from the polymer backbone, such that greater BPD$_{C1}$ incorporation leads to a more cylindrical coverage of the polymer backbone. The 50% BPD, 75% BPD, 90% BPD, and PIDT$_{C16}$-BPD$_{C1}$ samples were each extended to the limit of our strain stage (75% strain) without observed cracking. Because interactions between rigid backbones can inhibit reorganization, we predict that the greater shielding of polymer backbones with increased BPD$_{C1}$ incorporation, because of the resultant circular extension of alkyl side chains, allows them to deform by decreasing the interactions between neighboring polymer backbones. In other words, as these chains reorient because of strain, they are deflected from their neighbors before localizing stress between polymer backbones.[107] The polymer backbones of chains with more circular alkyl side-chain extension are thus more able to slide past each other during deformation. This contributes to a higher CoS, by weakening the overall intermolecular interactions and alleviating stress through chain flow rather than chain pullout.

2.4 Conclusion

BPD_{C1} incorporation alters the conformational properties of IDT polymer chains by increasing the average twist angle between monomer units. Despite this, DFT calculations suggest that BPD_{C1} incorporation does not impact the rigidity of the polymer backbone. The hole mobility of these random IDT copolymers was highly sensitive to introduced twist because of the decrease in intramolecular charge transport efficiency. The increased twist also leads to a more varied circular distribution of IDT hexadecyl side chains extending away from the backbone. As a result, the side chains surround the backbone to a greater extent for more BPD_{C1}-rich samples than for $PIDT_{C16}$-BT. Interestingly, FSC experiments demonstrate that this conformational change does not significantly alter the T_g's of these materials. We suggest that increased shielding of the polymer backbone with alkyl side chains, as a result of increased twist between monomer units due to BPD_{C1} incorporation, shields the rigid backbones from load-bearing interactions between polymer backbones which would otherwise inhibit chain reorganization and lead to chain pullout. This allows the polymer chains with more circular side-chain distribution to slide past each other more easily during elongation of the film, which increases their CoS. Also, FSC results suggest that other thermal transitions may play a role in differentiating the mechanical properties of IDT copolymers. These descriptions of possible deformation mechanisms require experimental confirmation, but we believe them to be important in understanding the links between conformational properties, thin film morphologies, and the mechanical properties of near-amorphous CPs and provide a pathway to design high charge mobility polymeric materials with increased ductility.

2.5 Supplementary Information

2.5.1 Chemical synthesis

All chemicals used in this study were purchased from commercial resources and were used as received. All reactions were carried out in air unless otherwise specified. A mixture of IDT (58.2 mg, 0.05 mmol), BPD and/or BT (see table below, 0.05 mmol total), tris(dibenzylideneacetone)dipalladium(0) (2.3 mg, 5 mol%), tris(o-anisyl)phosphine (1.8 mg, 10 mol%), cesium carbonate (81 mg, 0.25 mmol) and pivalic acid (2.6 mg, 0.025 mmol) in o-xylene (1 mL) was degassed and filled with nitrogen in a pressure reaction tube. The tube was sealed, and the mixture was heated at 100 °C for 24 h, followed by cooling to room temperature and precipitation into methanol (100 mL). The precipitate was filtered through a Soxhlet thimble and then purified by Soxhlet extraction with methanol, acetone and hexanes. The hexanes fraction was collected, and the solvent was removed by rotary evaporation. The residue was dissolved in chloroform and precipitated into methanol. The precipitate was collected by filtration and dried under vacuum to afford the final polymer, in yields specified in the table 3 below.

Poly(4-methyl-7-(4,4,9,9-tetrahexadecyl-7-methyl-4,9-dihydro-s-indaceno[1,2-b:5,6-b']dithiophen-2-yl)benzo[c][1,2,5]thiadiazole) ($PIDT_{C16}$-BT) ^{1}H NMR (500 MHz, $CDCl_3$, δ, ppm): 8.11 (s, 2H), 7.95 (s, 2H), 7.41 (s, 2H), 2.11 (s, 4H), 1.97 (s, 4H), 1.21-1.17 (m, 112H), 0.87-0.84 (t, 12H).

Poly(2-methyl-4-(4,4,9,9-tetrahexadecyl-4,9-dihydro-s-indaceno[1,2-b:5,6-b']dithiophen-2-yl)- isoindoline-1,3- dione) ($PIDT_{C16}$-BPD_{C1}) S4 ^{1}H NMR (500 MHz, $CDCl_3$, δ, S4 ppm): 7.91 (s, 4H), 7.39 (s, 2H), 3.25 (s, 3H), 2.10 (s, 4H), 1.92 (s, 4H), 1.23-1.21 (m, 112H), 0.88-0.85 (t, 12H).

Poly(4-methyl-7-(4,4,9,9-tetrahexadecyl-7-methyl-4,9-dihydro-s-indaceno[1,2-b:5,6-b']dithiophen-2-yl)-r-benzo[c][1,2,5]thiadiazole)-(4-methyl-7-(4,4,9,9-tetrahexadecyl-7-methyl4,9-dihydro-s-indaceno[1,2-b:5,6-b']dithiophen-2-yl)-r- dithiophen-2-yl)-isoindoline-1,3- dione) ($PIDT_{C16}$-r-BT-IDT_{C16}-r-BPD_{C1})

The integration of signals at 8.11ppm and 7.91ppm for each random copolymer sample are located in Table S5. 1 H NMR (500 MHz, $CDCl_3$, δ, S4 ppm): 8.11 (s), 7.91 (s), 7.39 (s, 2H), 3.25 (s, 3H), 2.10 (s, 4H), 1.92 (s, 4H), 1.23-1.21 (m, 112H), 0.88-0.85 (t, 12H)

Table 2.2. Ratios of monomers utilized during the synthesis of each IDT-copolymer system.

BPD%	BPD	BTD	Yield
0%	0 mg, 0 mmol	14.7 mg, 0.05 mmol	66%
10%	1.6 mg, 0.005 mmol	13.2 mg, 0.045 mmol	82%
30%	4.8 mg, 0.015 mmol	10.3 mg, 0.035 mmol	72%
50%	8.0 mg, 0.025 mmol	7.3 mg, 0.025 mmol	82%
70%	11.2 mg, 0.035 mmol	4.4 mg, 0.015 mmol	80%
90%	14.4 mg, 0.045 mmol	1.5 mg, 0.005 mmol	89%
100%	15.9 mg, 0.05 mmol	0 mg, 0 mmol	91%

2.5.2 DFT Calculations

All structures were drawn in Chemdraw™ and imported into Gaussview™ in order to set up the calculations. The calculations were performed using Gaussian™ version 16.b01. The 9- mers were optimized with the Becke, 3-parameter, Lee–Yang–Parr (B3LYP) functional and 6- 31g(d) basis set. The potential energy scans of the torsional angle between IDT-BT and IDT-BPD bonds were performed using the ωB97X-D functional and 6-31+G(d,p) basis set.

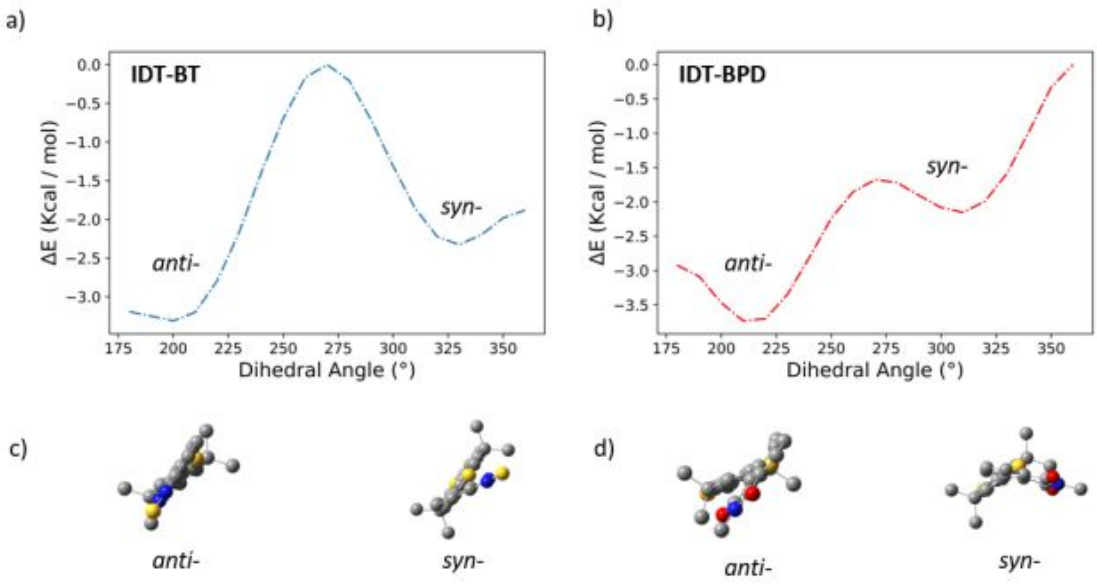

Figure 2.7. The torsional potentials of the a) IDT-BT and b) IDT-BPD bonds. Edge-on views of the anti- and syn- conformers of the c) IDT-BT and d) IDT-BPD bonds.

Table 2.3. Differences in energy between minima ($\Delta E_{syn\text{-}anti}$), the Boltzmann probability ratio of each conformer, and the barrier heights of rotation from each minimum ($Ea_{,rot}$) are reported.

IDT Comonomer	$i\ E_{syn\text{-}anti}$ (Kcal/mol)	$\frac{Panti}{Psyn}$ (@ 298K)	$E_{a\ rot,\ syn\ to\ anti}$ (Kcal/mol)	$E_{a\ rot,\ anti\ to\ syn}$ (Kcal/mol)
BT	1.58	5.4	0.48	2.33
BPD	0.99	12.7	2.06	3.31

Bonds between conjugated rings in CPs are either in the syn- or anti-conformation. Conjugated polymers display energetic preferences for the anti-conformation because it offers less steric interactions between conjugated rings. Repeated anti-linkages lead to straighter polymers due to the averaging of the vector directions of repeated backbone deflections to a net-linear direction. When a syn-linkage does occur, the deflection of the prior linkage and the current linkage sum to a value twice

the deflection angle and deflect the polymer away from a linear path.[72] For these reasons a smaller deflection angle and a greater preference for anti-linkages between monomers lead to more linear polymer chains. The polymers synthesized for our study are of low M_n. Torsional potential energy scans of each linkage suggest that the anti-conformer of the IDT-BPD linkage is greatly favored, and the barrier to rotation from the anti-conformer is too large to overcome at room temperature.5 The deflection angle of the IDT-BT linkage is near zero, and the IDT-BPD linkage is also expected to be minimal due to the para-substitution about the BPD monomer.3 With this in mind, all samples are expected to be linear and of similar rigidity.

2.5.3 Crystallographic measurements

GIWAXS measurements were performed at 8-ID-E beamline of the Advanced Photon Source, Argonne National Laboratory with 10.86 keV (λ = 0.11416 nm) synchrotron radiation. Film thickness of the samples in GIWAXS measurement was kept between 120 – 200 nm as confirmed by spectroscopic ellipsometry. Samples were measured inside a low vacuum chamber (<10-3 mbar) to prevent radiation damage and background scattering from ambient air. For each sample, 3 data sets were taken from 3 adjacent spots on the sample and then summed to improve the signal-to-noise ratio. Each spot was exposed to the X-ray beam for 10 s. During the measurement, the samples were tilted at an angle of incidence of 0.14° with respect to the incoming beam. This angle was chosen to be above the estimated critical angle of sample (ca. 0.13°) but below the critical angle of the Si substrates (ca. 0.17°). The scattering signal was recorded with a Pilatus 1MF pixel array detector (pixel size = 172 μm) positioned 228 mm away from the sample. Each data set was stored as a 981x1043 32-bit tiff image with 20-bit dynamic range. The Pilatus detector has rows of inactive pixels at the border between detector modules. In order to fill these gaps, after each measurement the detector was moved to a new vertical direction and the measurement on each spot was repeated, then the gaps were filled by

combining the data from two detector positions. Each image was further subjected to nonuniformity, detection efficiency, the polarization effect and solid-angle variation correction. All the data processing and extraction were executed using the GIXSGUI package for MATLAB.[121]

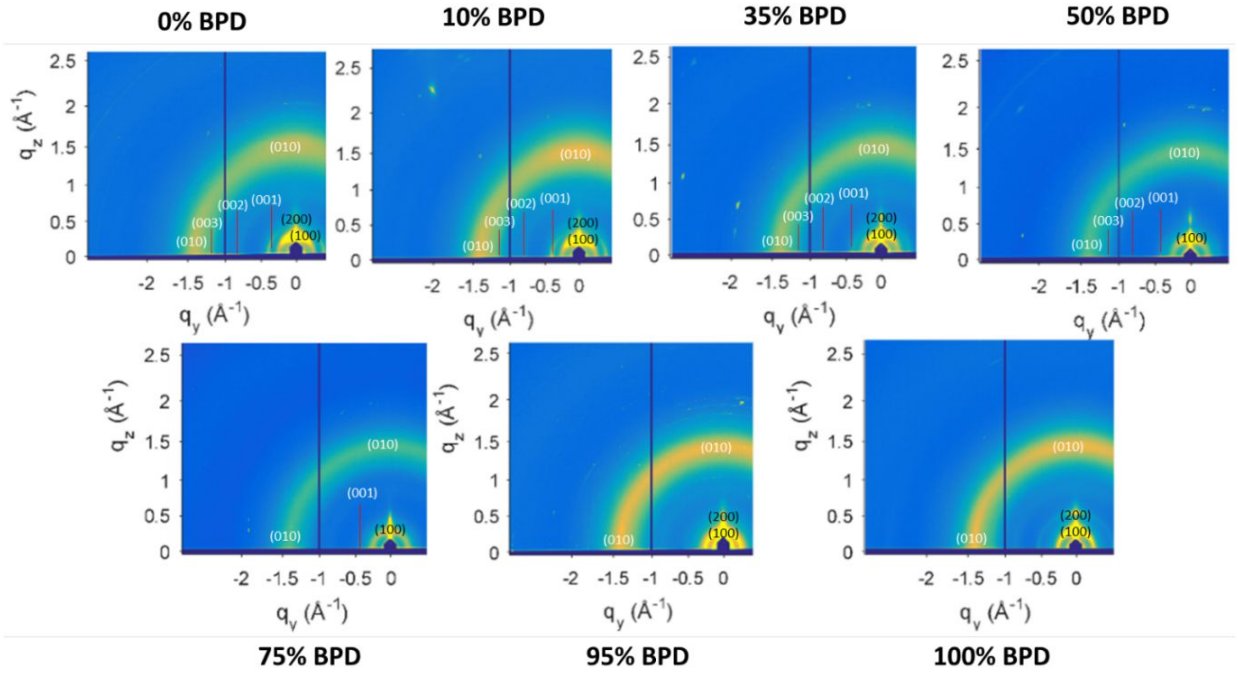

Figure 2.8. 2D GIWAXS spectrum of each IDT-copolymer. The crystallographic plane of each signal has been labeled.

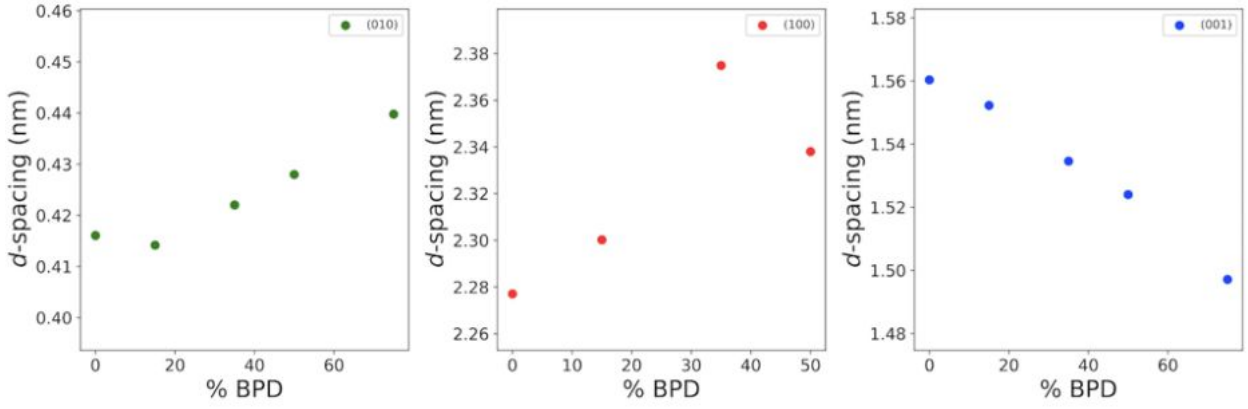

Figure 2.9. The d-spacing of the π-π (010), alkyl stacking (100), and interchain (001) signals from GIWAXS experiments.

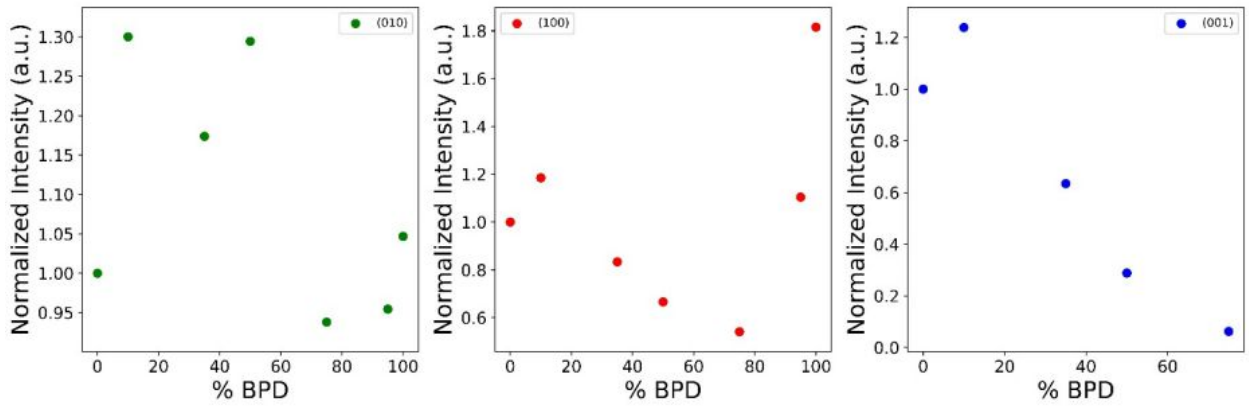

Figure 2.10. The thickness normalized intensity of the π-π (010), alkyl stacking (100), and interchain (001) signals from GIWAXS experiments.

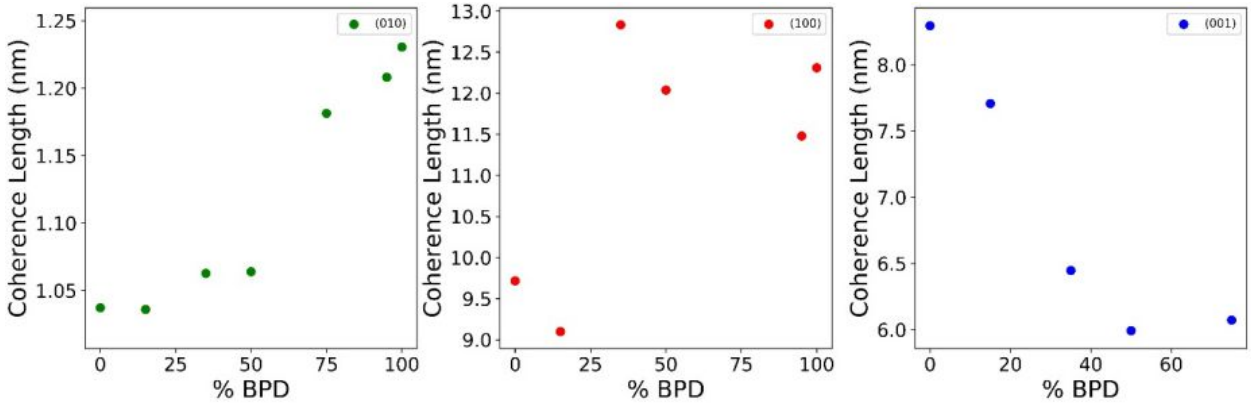

Figure 2.11. The coherence lengths from Scherrer analysis of the π-π (010), alkyl stacking (100), and backbone (001) signals from GIWAXS experiments.

2.5.4 Charge Transport Property Measurement

Heavily boron-doped silicon substrates with a 300 nm (± 5 nm) thick thermal oxide layer (WRS Materials) as a gate dielectric were used for the organic field-effect transistors (OFETs). Substrates S7 were first scrubbed with detergent and water and then sonicated in DI water, acetone, and IPA for 15 min per solvent, followed by drying under a stream of compressed air. The substrates were then cleaned in a plasma cleaner for 15 min using air plasma. In order to passivate the thermal oxide, a vacuum

vapor deposition of octadecyltrichlorosilane (OTS) on the cleaned substrates was used. After the OTS deposition, the substrates were rinsed with chloroform and IPA to remove any physisorbed OTS from the surface. The polymer layer was then spin-coated from chlorobenzene at 3000 RPM for 60 s onto the OTS passivated substrate. Gold electrodes were thermally evaporated onto the active layer to a thickness of 60 nm at a rate of 1 Å·s-1. The gold was evaporated from an alumina coated Mo boat and the electrodes were deposited through a shadow mask. After electrode deposition, the devices were tested for charge mobility and current on/off ratio. The devices had a top-contact bottom-gate architecture with a channel width of 1000 µm and a channel length of 50 µm. They were tested in a N2 atmosphere using a Signatone Probe Station. The transfer curves were collected in the saturation regime, where the linear section of the I_{DS}-V_G curve was fitted to estimate the charge mobility using

$$I_{DS} = \frac{\mu \cdot W \cdot C}{2L} \cdot (V_G - V_t)^2 \quad (1)$$

where IDS is the drain-source current; µ is the charge mobility; W is the channel width; L is the channel length; C is the capacitance per unit area of the insulator (SiO2, 300 nm, 10 nF·cm−2); VG is the gate voltage; and Vt is the threshold voltage. Using the passivated substrates, optimization experiments were run to determine the best conditions for processing the polymer into OFETs. The conditions that were optimized include casting solvent and spin speed. Due to their low Tg, the devices were not annealed. A final batch of devices was made using the optimized S8 conditions. At least 5 devices across 3 substrates were tested to obtain an average value for the charge mobility and current on/off ratio.

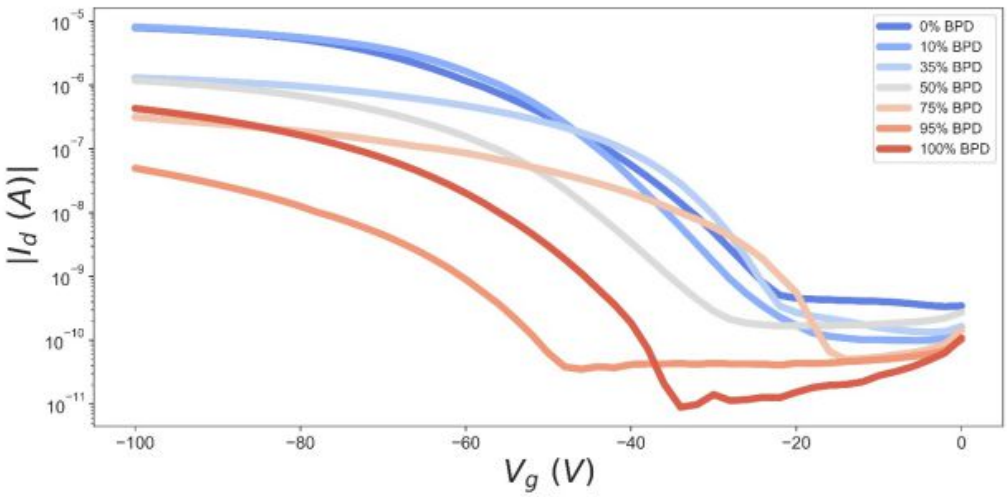

Figure 2.12. Representative drain current versus gate voltage (IdVg) curves for each polymer system.

Table 2.4. The CoS and μ_h for each IDT-copolymer.

% BPD	*CoS* (%)	μ_h (cm² V⁻¹ s⁻¹)
0	7	2.96E-02 ± 1.0E-02
10	7	1.85E-02 ± 8.0E-03
35	44	3.29E-03 ± 7.8E-04
50	>75	4.47E-03 ± 1.5E-03
75	>75	2.44E-03 ± 6.5E-04
95	>75	3.64E-04 ± 9.6E-05
100	>75	1.54E-03 ± 6.0E-04

Table 2.5. The reliability factor (rlin), on/off current ratio (Ion / Ioff) and threshold voltage (VT) is shown for each polymer.

% BPD	r_{lin} [4]	I_{on} / I_{off}	V_T (V)
0	0.50	1.23E+05	-49
10	0.69	1.11E+04	-25
35	0.63	1.80E+04	-44
50	0.58	1.59E+05	-41
75	0.61	1.54E+05	-55
95	0.50	8.47E+05	-68
100	0.57	5.11E+05	-64

The rlin value in Table S4 is the reliability factor averaged across all OFET devices per each polymer sample. The values of rlin for our devices suggest that the fitted data is off sufficient quality.[122]

2.5.5 Crack Onset Strain Measurements

Glass substrates were first scrubbed with detergent and water and then sonicated in DI water, acetone, and IPA for 15 min per solvent, followed by drying under a stream of compressed air. The substrates were then cleaned in a plasma cleaner for 15 min using air plasma. Following plasma cleaning, a sacrificial PEDOT:PSS (Clevios P VP AI 4083, Heraeus) layer was spin-coated at 3,000 RPM for 60 s from 120 µL of PEDOT:PSS suspension, then annealed at 140 °C for 15 minutes. Prior to spin-coating PEDOT:PSS suspension was first sonicated for 60 s, then filtered through a 0.45 µm pore size PTFE syringe filter. Following annealing, the IDT copolymers were spin-coated from 80 µL in CHCl3 at a concentration of 5 mg/mL under an inert atmosphere at a spin speed of 2,000 RPM for 60 s. PDMS substrates were prepared from a Sylgard 184 kit, at a mix ratio of 10:1 of silicone elastomer to curing agent, at the designation of the manufacturer. Following mixing, the material was poured into the casting mold, and then placed under high vacuum for 2-4 hours, to completely degas the mixture. Following degassing, the PDMS was cured for 4 h in air at 60 °C. The side of the PDMS that was facing the air during curing was the side that the IDT copolymer films were laminated to, to minimize

substrate roughness. Film transfer was performed by laminating the IDT copolymer to the PDMS substrate, then immersing in water to dissolve the sacrificial PEDOT:PSS layer and release the IDT copolymer. Following film transfer, the PDMS was dried under a stream of air to remove residual water. To measure the *CoS*, the PDMS substrate was placed into a homemade strain stage underneath a Zeis AX10 optical microscope. The samples were observed under a constantly increasing strain, being monitored for the formation of cracks. For several samples, no cracks were observed at the limit of the strain stage (<75%), and so a value of >75% was recorded for such samples.

2.5.6 Fast Scanning calorimetry Measurements

Fast Scanning Calorimetry was conducted under nitrogen using a Mettler Toledo Flash DSC 1 equipped with a Huber TC100 cooler to control the temperature between -90 and +450 °C. Powder of the two polymers were deposited onto Flash DSC chips with the use of a silicone oil that has no significant thermographic features in the temperature range of interest. Samples were subjected to a thermal aging process via 30 minute isotherms in the range of -90 to +160 °C, followed by 2 sequences of 4000 °C/s heating and cooling from -90°C to +350 °C as outlined in Fig. SX2. The overshoot between the heat flow of the first heating and second heating was used to calculate the glass transition temperature. Figure 2.5 depicts the aging method used to determine the glass transition temperature of $PIDT_{C16}$-BT and $PIDT_{C16}$-BPD_{C1}. This method is analogous to the one used in previous studies.[116,117] Samples were initially heated to +350 °C (TH in Figure 2.5) and immediately cooled to the aging temperature (Ta in Figure 2.5) at a rate of -4000 °C /s. At this temperature, samples were aged for 30 min and subsequently cooled at -4000 °C to -90 °C (TL in Figure 2.5). The subsequent heating scan at +4000 °C/s to TH was recorded (heating cycle a in Figure 2.5). This scan delivered the heat flow rate of aged samples. Finally, samples were cooled at -4000 °C/s to -90 °C and immediately heated to +350

°C at +4000 °C/s to TH to obtain the reference thermogram for an unaged sample (heating cycle b in Figure 2.5).

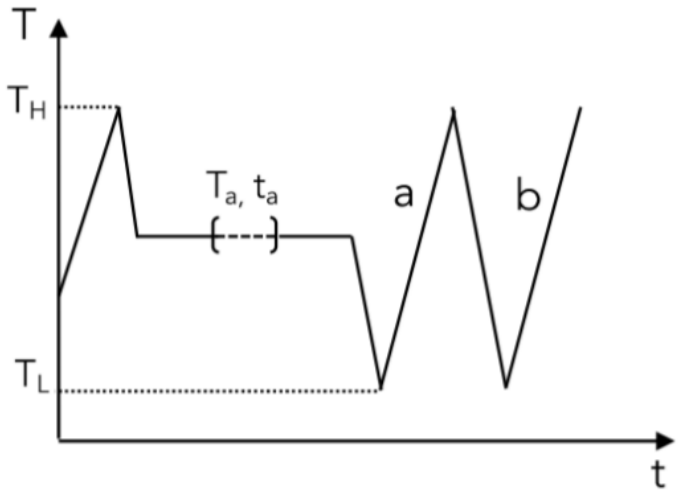

Figure 2.13. Temperature program followed for the aging of polymer samples conducted with Mettler Toledo Flash DSC 1.

To determine the onset of the glass transition temperature, the enthalpy overshoot was calculated via Equation 1. When plotting the enthalpy recovery versus aging temperature, a linear extrapolation can be performed to determine the temperature at which Eqn 1 is zero. This temperature correlates to the onset of the glass transition temperature.[116,117]

$$\Delta H(T_a, t_a) = \int_{T \ll T_g}^{T \gg T_g} \left(C_p^{aged}(T) - C_p^{unaged}(T) \right) dT \qquad (2)$$

where C_p indicates the heat capacity of the aged and unaged samples, and ΔH is the recovered enthalpy from the aging process. Only the positive overshoot was considered, since the aging temperatures neared the lower temperature limit of the instrument, thus, creating a fluctuating baseline prior to the transition.

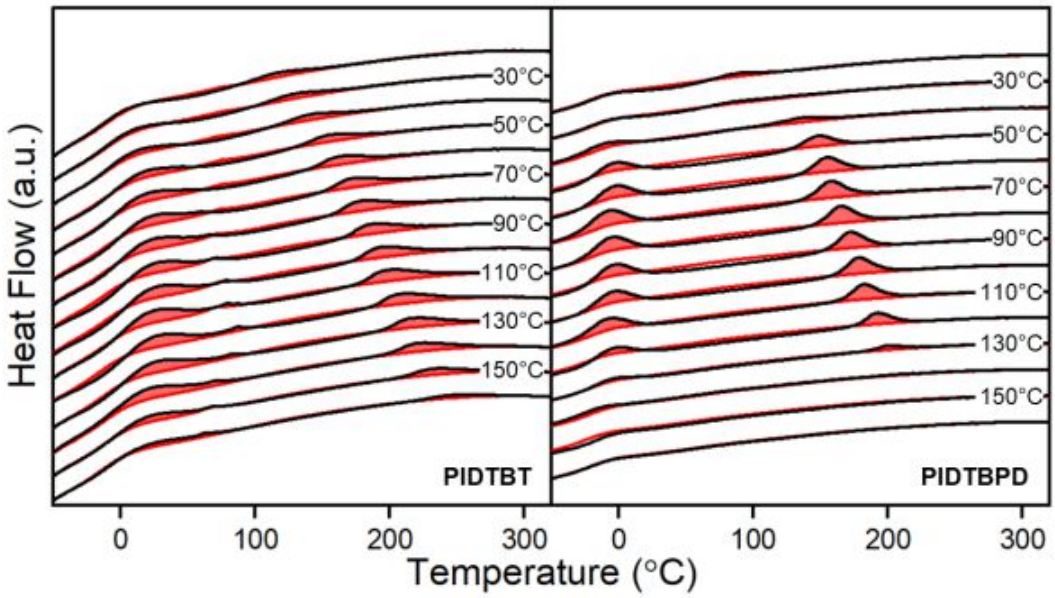

Figure 2.14. Fast scanning calorimetry heating thermograms measured for $PIDT_{C16}$-BT (left) and $PIDT_{C16}$-BPD_{C1} (right) using 'aging' temperatures above the glass transition temperature. Two distinct endotherms appear when annealing samples above the glass transition temperatures, indicating possible liquid-crystalline or liquid-crystalline-like transitions. These occur at temperatures notably below room temperature (around 0 °C) for $PIDT_{C16}$-BPD_{C1}, while for $PIDT_{C16}$-BT the transition is around room temperature with a tail reaching 100 °C.

2.5.7 Optoelectronic measurements

UV-Vis and PL spectra were measured on a Varian Cary 5000 UV-Vis-NIR spectrometer and a Horiba Fluorolog FL-3 spectrometer, respectively. Solution measurements were performed in chloroform solutions with a polymer concentration of 0.05 mg/mL. Thin films used for measurement were spin cast from a chloroform solution with a polymer concentration of 5 mg/mL onto cut glass substrates.

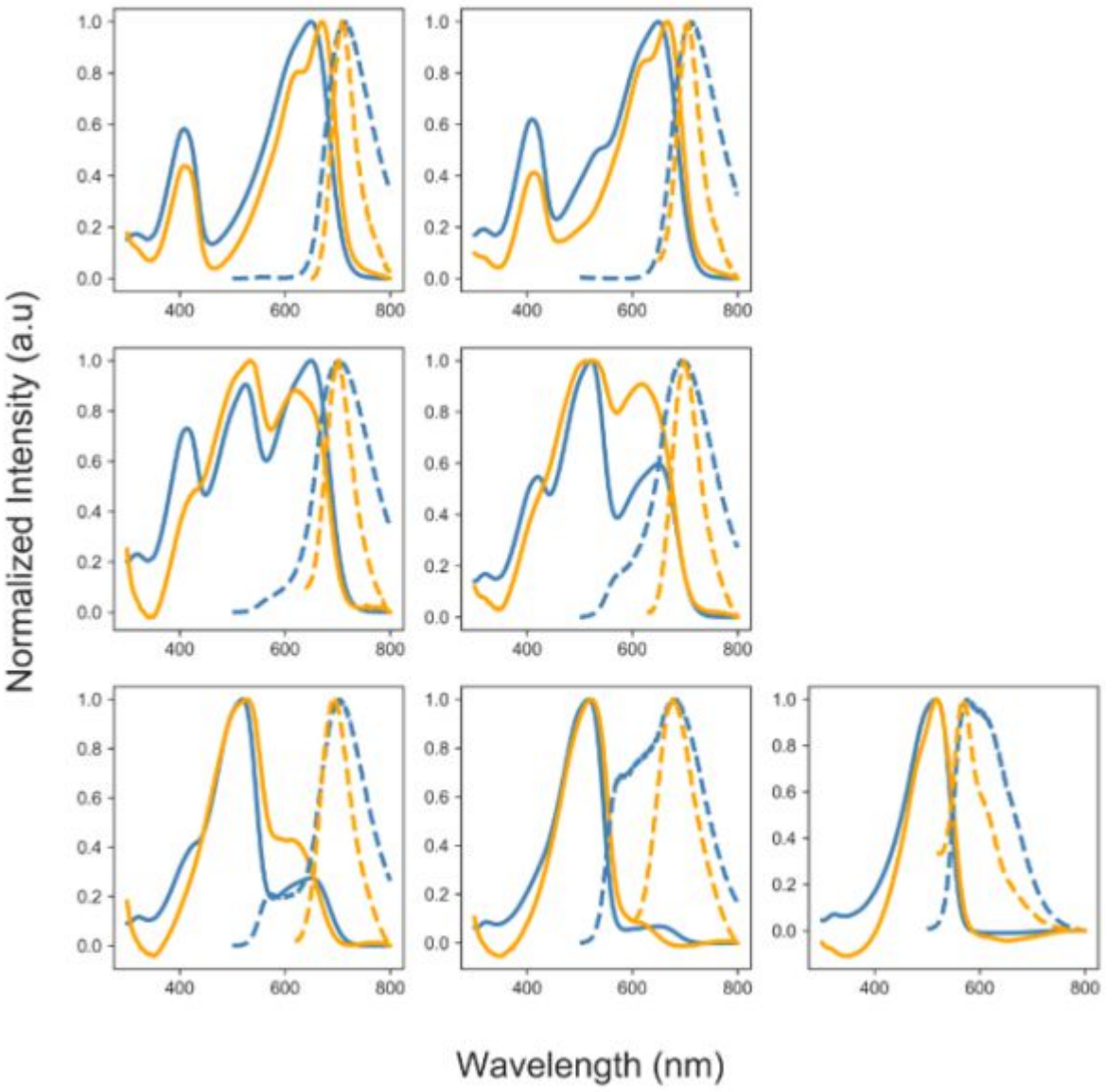

Figure 2.15. The $CHCl_3$ solution (blue) and thin-film (orange) UV-Vis (solid) and PL (dashed) spectra of each copolymer is shown.

2.5.8 ^{1}H NMR Spectra

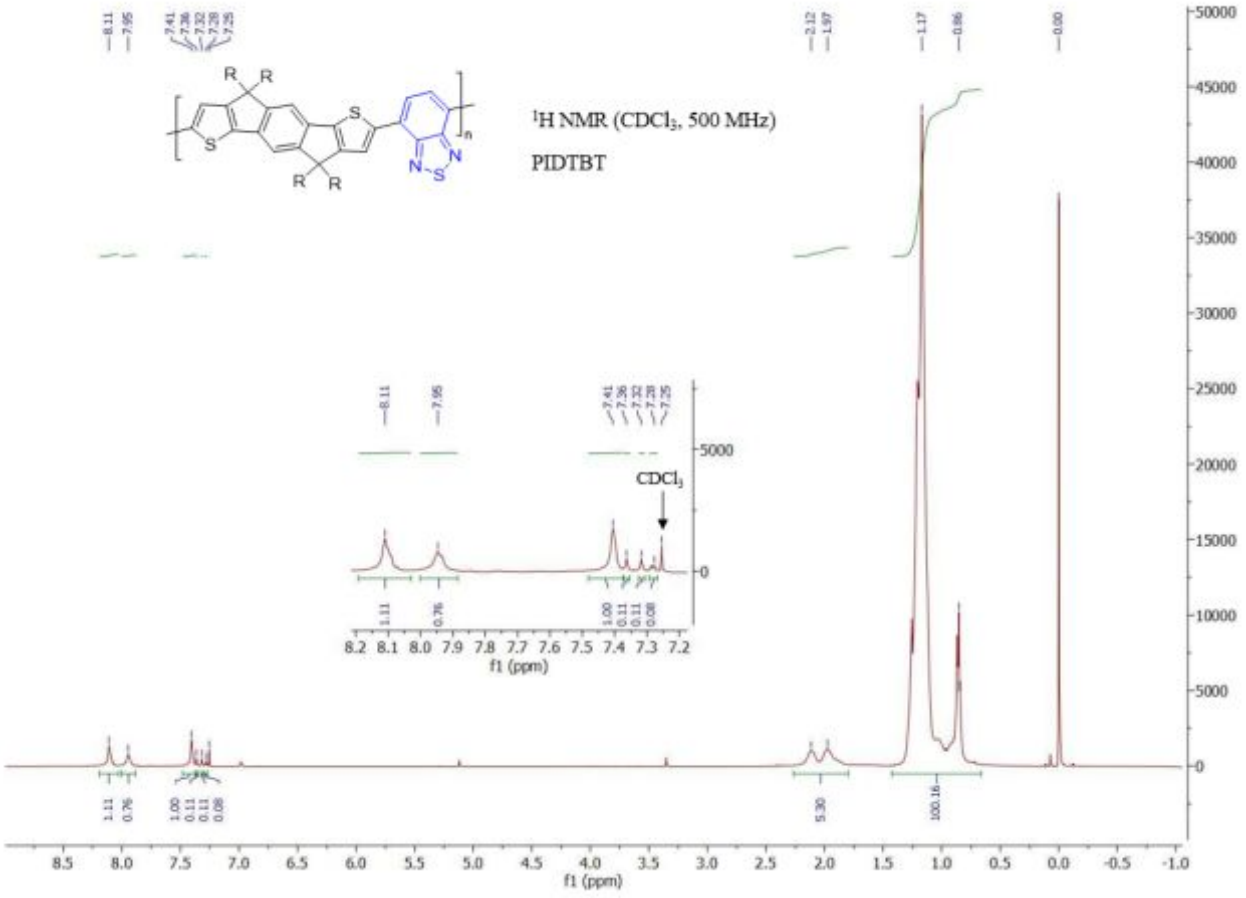

Figure 2.16. ^{1}H NMR spectra of $PIDT_{C16}$-BT.

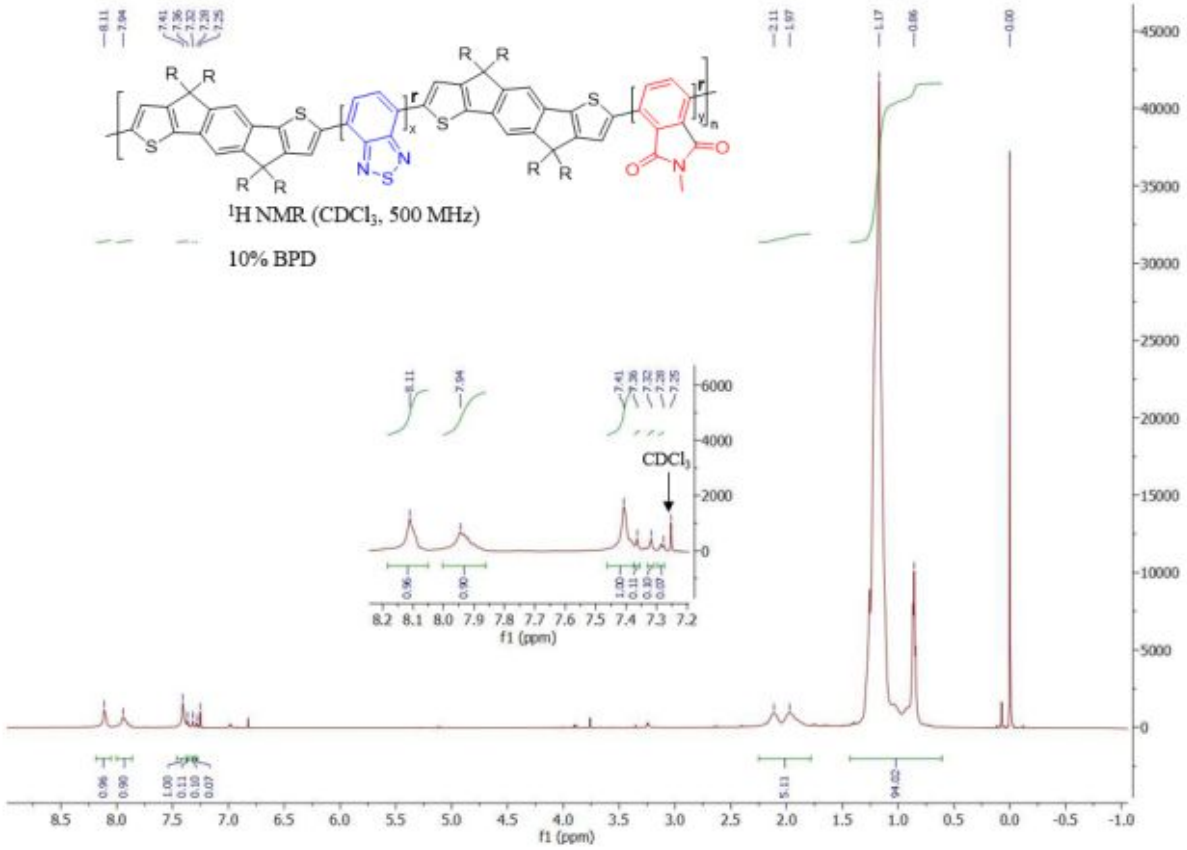

Figure 2.17. ^{1}H NMR spectra of 10% BPD.

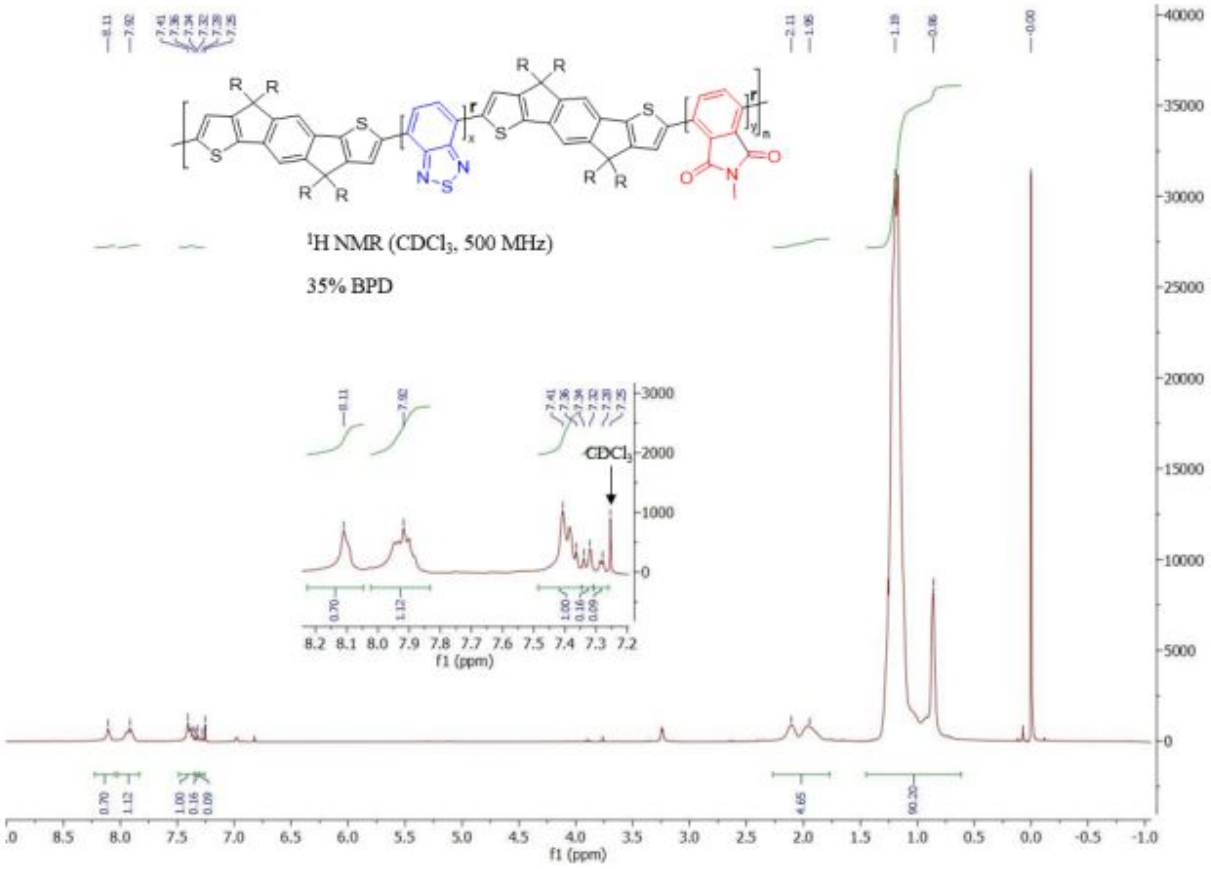

Figure 2.18. ^{1}H NMR spectra of BPD 35%.

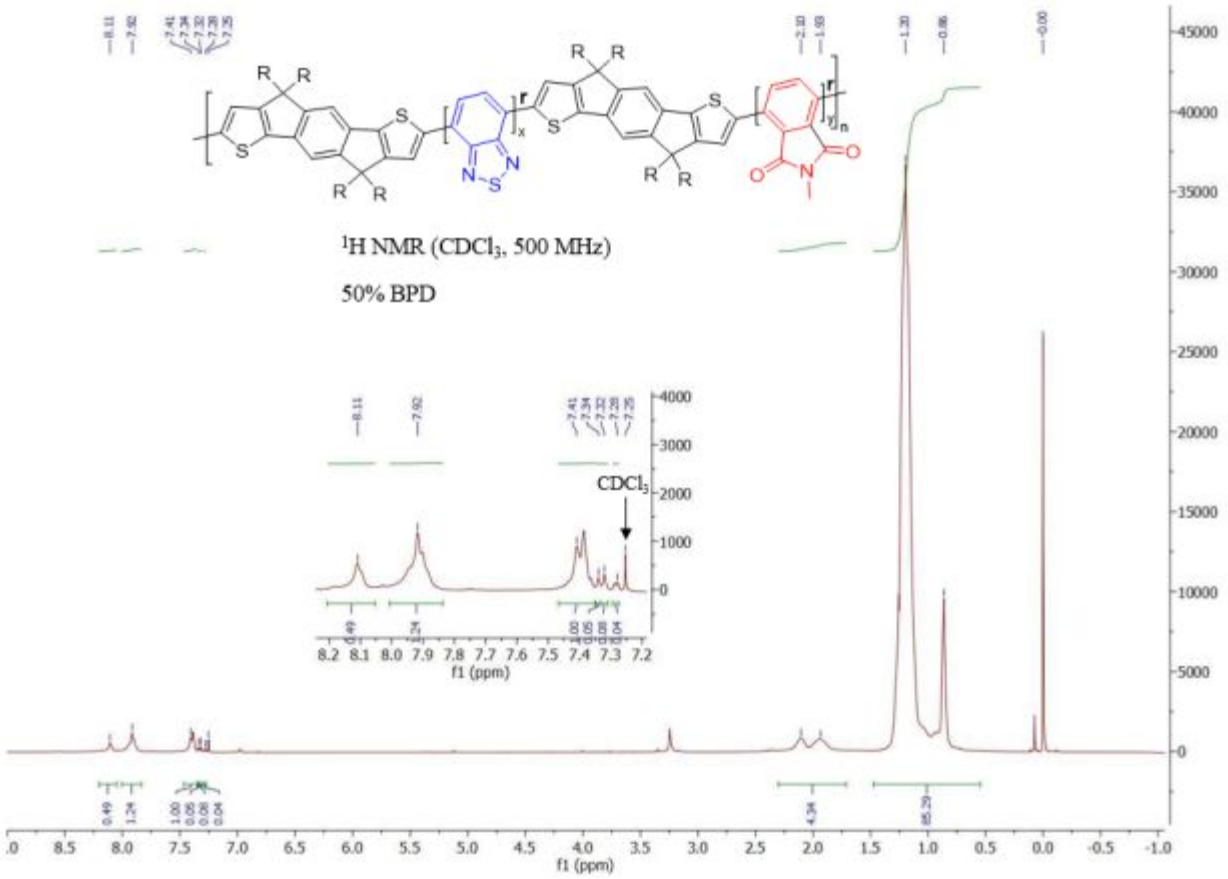

Figure 2.19. ^{1}H NMR spectra of BPD 50%.

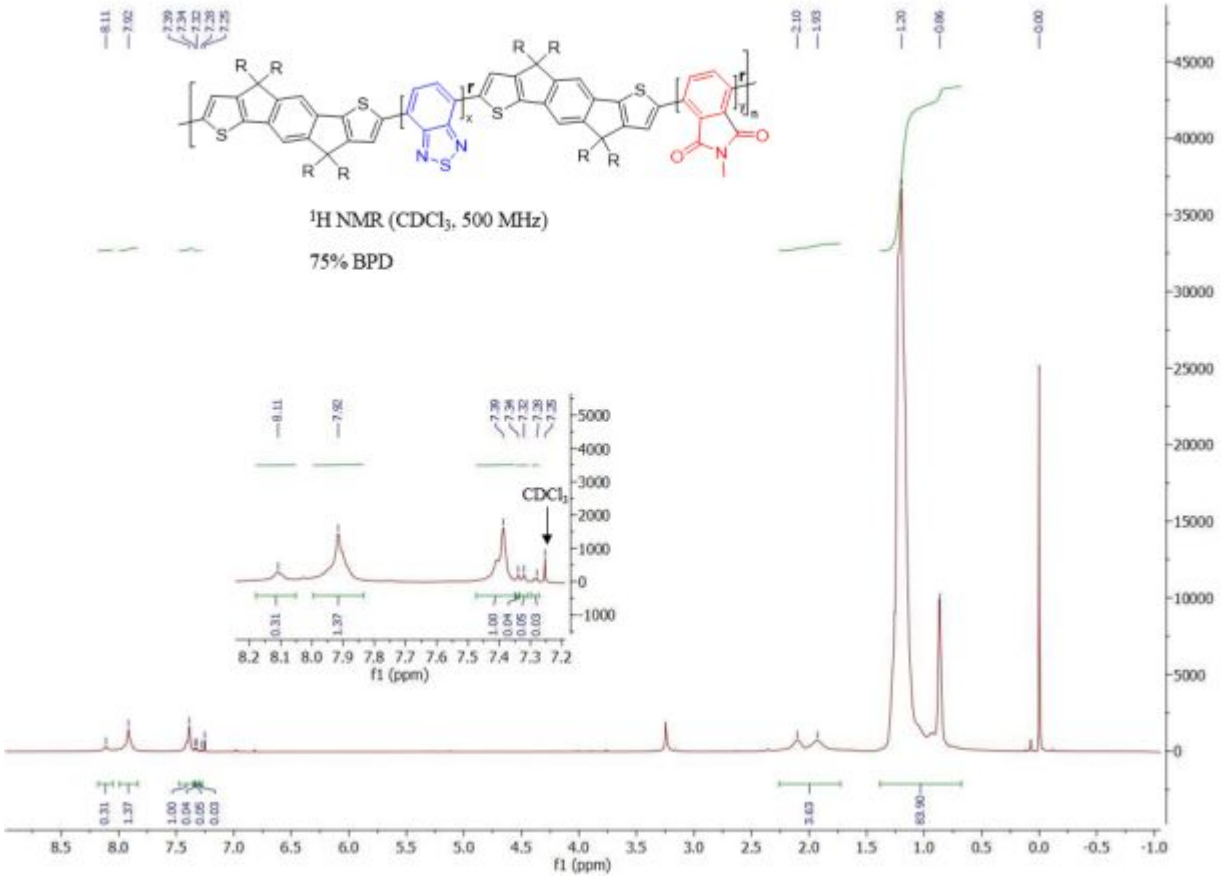

Figure 2.20. ^{1}H NMR spectra of BPD 75%.

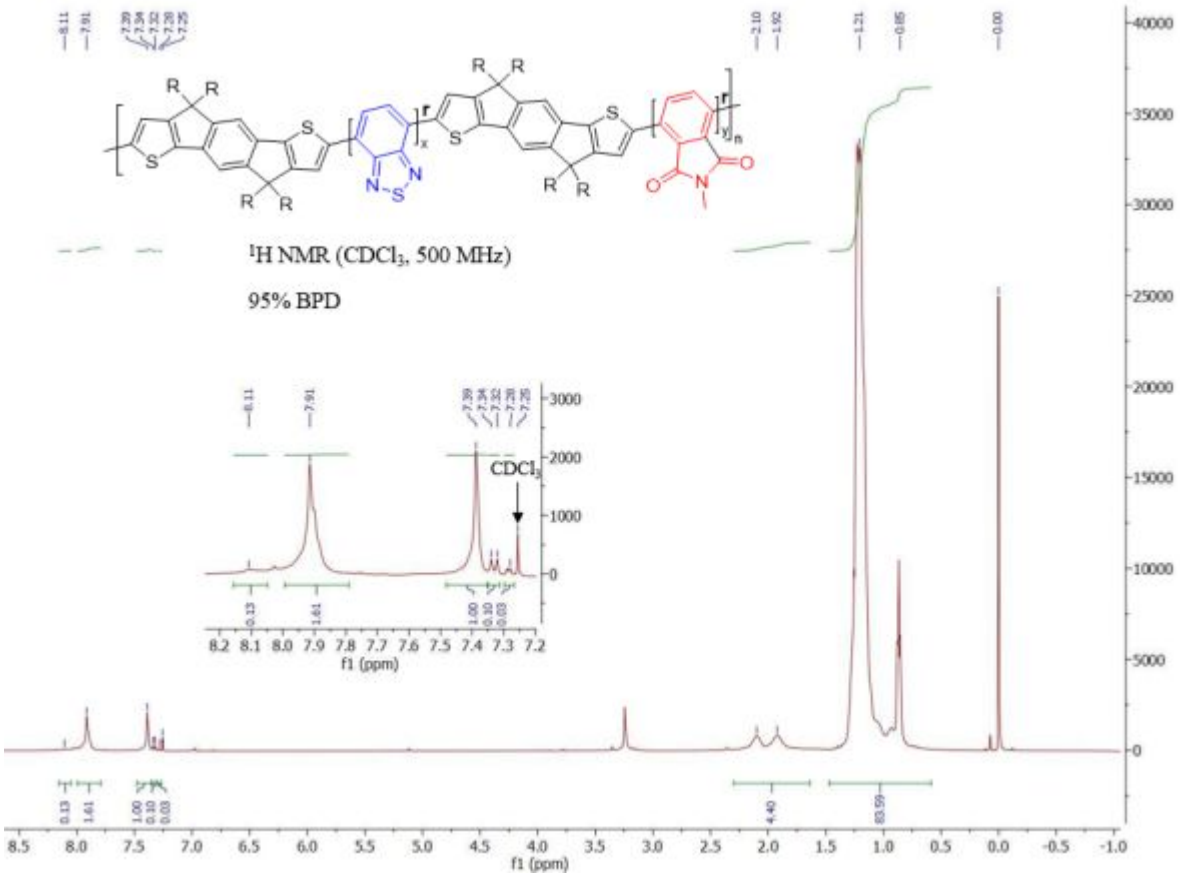

Figure 2.21. ^{1}H NMR spectra of BPD 95%.

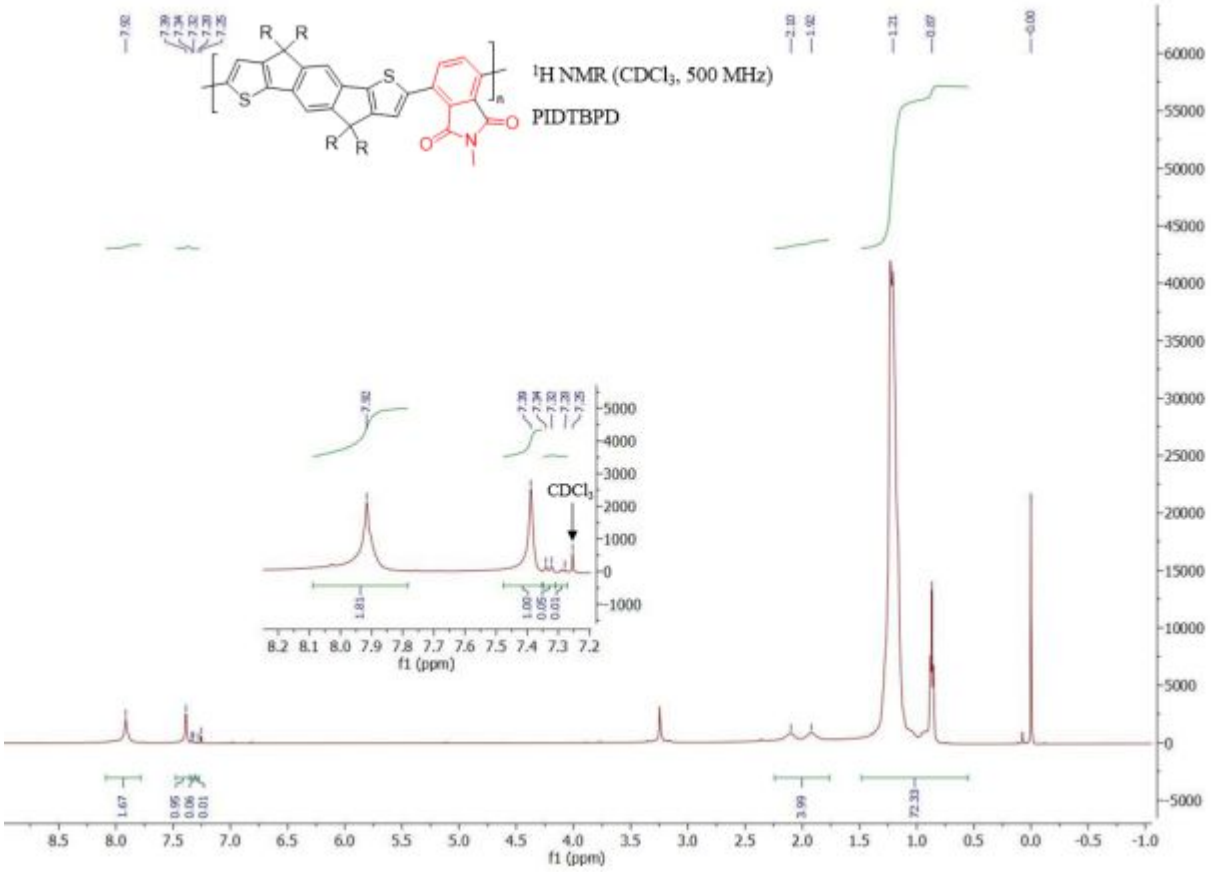

Figure 2.22. ^{1}H NMR spectra of BPD 100%.

Chapter 3. Uncovering the impact of side-chain interdigitation in determining the response to strain and hole mobility of planar indacenodithiophene copolymers through side chain substitution

3.1 Abstract

Indacenodithiophene (IDT)-copolymers are a class of conjugated polymers with near-amorphous thin-film morphologies and high hole mobilities, which makes them promising candidates for use in deformable electronic devices. Key to their high hole mobilities is the coplanarity monomer repeat units within the backbone. Poly-indacenodithiophene benzothiadiazole ($PIDT_{C16}$-BT) and poly-indacenodithiophene-thiapyrollodione ($PIDT_{C16}$-TPD_{C1}) are two IDT-copolymers with backbone planarity, but are brittle at low molecular weight and have unsuitably high elastic moduli. Substitution of the hexadecane (C_{16}) side chains of the IDT monomer with isocane (C_{20}) side chains was performed to generate a new BT-containing IDT Copolymer: $PIDT_{C20}$-BT. Substitution of the methyl (C_1) side chain on the TPD monomer for an octyl (C_8) and 6-ethylundecane (C_{13B}) afforded two new TPD-containing IDT copolymers named $PIDT_{C16}$-TPD_{C8} and $PIDT_{C16}$-TPD_{C13B}, respectively. Both $PIDT_{C16}$-TPD_{C8} and $PIDT_{C16}$-TPD_{C13B} undergo plastic deformation, have early yield points, and significantly reduced elastic moduli. These mechanical properties manifest themselves because the lengthened side chains extending from the TPD-monomer inhibit side chain interdigitation in these materials, which affords these materials plastic deformation as a stress deformation mechanism while under strain. Side chain interdigitation can occur in $PIDT_{C16}$-BT, $PIDT_{C20}$-BT and $PIDT_{C16}$-TPD_{C1} because side chain character remains only on the IDT-subunit, resulting in brittle thin-films. Unfortunately, because of the role interdigitation plays in ordering IDT-copolymers, $PIDT_{C16}$-TPD_{C8} and $PIDT_{C16}$-TPD_{C13B} display lower hole mobilities compared to the other IDT copolymers. These results demonstrate that

disrupting interdigitation in IDT-copolymers through comonomer side chain extension leads to more ductile thin films wither lower elastic moduli, but decreased hole mobility because of altered morphological ordering in their respective thin-films.

3.2 Introduction

Increased interest in deformable electronic devices such as e-skin, wearable sensors, stretchable organic photovoltaics, soft robotics, and stretchable organic field effect transistors warrants the development of intrinsically deformable electronic materials.[94,123–125] Π-conjugated polymers (CPs) can be utilized as a semiconducting material within deformable devices because of their tunable electronic properties and wide variance of mechanical properties.[48] As is the case for commodity polymers and their applications, a single CP will not satisfy the various optoelectronic, semiconducting, or mechanical requirements of different deformable electronic applications. Different polymers with varying elastic moduli, fracture strains, rheological properties, stress-strain profiles, solubilities, optoelectronic profiles, and hole mobilities will be required for different applications. This warrants the further development of structure property relationships for conjugated polymer systems to guide the design of new intrinsically deformable conjugated polymers to address this need.

The structure of the polymer backbone and solubilizing side chains of conjugated polymers dictate their materials properties.[126] Alterations in the chemical structure of both the backbone and side chains of CPs impact the intrinsic electronic characteristics, conformational, thermal, and morphological properties of the systems;[105,127] changes to these properties directly influence materials properties of interest including hole mobility ($\mu_{,hole}$), fracture strain, and elastic modulus.[128] These three metrics are among those considered when determining the application for which a particular CPs are best utilized.[34]

Side chain substitution has been shown to impact the materials properties of semicrystalline conjugated polymers. For both poly-3-alkylthiophene (P3ATs) and DPP-based CPs it has been shown that increasing the length or increasing branching of side chains results in increased elongation at break and decreased elastic modulus.[105,129,130] This is caused primarily because of a resultant decrease in both glass transition temperature (T_g) and the amount of load bearing interactions that occur between polymer backbones during deformation, with both effects affording these materials an enhanced ability to reorganize polymer chains during strain.[48] It is important to consider however that side chain modifications can also lead to changes in thin film morphology that manifest differences in $\mu_{,hole}$.[127,131]

Near-amorphous conjugated polymers are prime candidates for use in deformable electronics because their low degree of crystallinity, relative to semicrystalline CPs, affords them the potential to dissipate strain energy through polymer chain rearrangement without the encumbrance of disrupting large crystalline domains and the concomitant decrease in $\mu_{,hole}$.[132] Indacenodithiophene (IDT) copolymers are a class of donor acceptor CPs that are near amorphous due to the presence of four, often hexadecane (C_{16}), side chains that flank the IDT monomer unit and inhibit long-range crystallinity in IDT-copolymer thin films.[98] It has become well established that the backbone planarity of an IDT-copolymer's backbone gives rise to low energetic disorder and quasi-one dimensional charge transport along the backbone.[25,85] Poly-indacenodithiophene-benzothiazdiazole (PIDT$_{C16}$-BT) is the most studied IDT-copolymer and has displayed charge mobilities up 3.6 $cm^2\ V^{-1}\ s^{-1}$.[25] In terms of mechanical properties, PIDT$_{C16}$-BT is exceptionally brittle at low molecular weight (M_n = 12 kg/mol) with a crack onset strain (*CoS*) of just 3%,[53] stretchable up to 22% of its original length at significantly higher molecular weight (M_w = 295 kg/mol),[98] and has elastic moduli ranging from 150-750 MPa depending on molecular weight.[53,98] Similarly to PIDT$_{C16}$-BT, Poly-indacenodithiophene-thiopyrollodione (PIDT$_{C16}$-TPD$_{C1}$) has a highly coplanar backbone, a near-amorphous thin-film

morphology, a *CoS* of 3%, an elastic modulus ranging between 110 to 410 MPa, and has displayed equal $\mu_{,hole}$ to that of PIDT$_{C16}$-BT when processed under the same conditions.[53] In contrast to both PIDT$_{C16}$-BT and PIDT$_{C16}$-TPD$_{C1}$, the more torsioned IDT-copolymer poly-indacenodithiophene-benzopyrollodione (PIDT$_{C16}$-BPD$_{C1}$) is much more stretchable than PIDT$_{C16}$-BT, displaying a *CoS* of 75% at low molecular weight (M_n = 14 kg/mol).[53] The backbone torsion in PIDT$_{C16}$-BPD$_{C1}$ has the positive effect of generating a circular side chain extension profile which allows the system to undergo plastic deformation, but negatively impacts charge mobility drastically.[133] Comparing the mechanical and electronic properties of these IDT-copolymers highlights the necessity of backbone planarity for low energetic disorder and thus high $\mu_{,hole}$, as well as the impact that side chains have on the deformation of IDT-copolymers. Therefore, altering the side chains of PIDT$_{C16}$-BT and PIDT$_{C16}$-TPD$_{C1}$, which are both coplanar, is a potential strategy to endow each polymer system with increased elongation at break and decreased elastic moduli without significantly altering their $\mu_{,hole}$.

Five distinct IDT-copolymer systems are synthesized and investigated herein to determine the impact that side chain substitution has on the mechanical and electronic properties of planar IDT copolymers. Two are BT-containing IDT copolymers, called PIDT$_{C16}$-BT and PIDT$_{C20}$-BT, and the three others are TPD-containing IDT-copolymers called PIDT$_{C16}$-TPD$_{C1}$ PIDT$_{C16}$-TPD$_{C8}$, and PIDT$_{C16}$-TPD$_{C13B}$. The structures of these polymers are shown in Figure 3.1. We observe that IDT-copolymers with none or methyl side chains on their acceptor unit (PIDT$_{C16}$-BT, PIDT$_{C20}$-BT, and PIDT$_{C16}$-TPD$_{C1}$) display a (001) signal in their GIWAXS profile that is representative of parallel alignment of polymer backbones within their thin films. For parallel arrangement of polymer backbones to occur, it is necessary for the long and linear side chains stemming from the IDT unit to interdigitate with the side chains of neighboring chains. Fast scanning calorimetry (FSC) experiments also demonstrate that PIDT$_{C16}$-BT, PIDT$_{C20}$-BT, and PIDT$_{C16}$-TPD$_{C1}$ display liquid crystalline-like

ordering of the backbone which supports the GIWAXS evidence. The lengthened and branched side chains on the TPD-monomer unit in PIDT$_{C16}$-TPD$_{C8}$ and PIDT$_{C16}$-TPD$_{C13B}$ prohibit polymer backbones from interdigitating. This is because the side chains on the TPD$_8$ and TPD$_{C13B}$ monomer units occupy the space that IDT$_{C16}$ side chains on neighboring polymer chains would need to occupy. Lacking interdigitation, PIDT$_{C16}$-TPD$_{C8}$ and PIDT$_{C16}$-TPD$_{C13B}$ have improved ductility and decreased elastic moduli. This is because interdigitation of the long IDT-side chains inhibits plastic flow of chains during elongation. Despite retaining their backbone planarity, these systems display reduced $\mu_{,hole}$, providing further evidence for the importance of parallel alignment of IDT-copolymer backbones to high $\mu_{,hole}$. In contrast, PIDT$_{C16}$-BT, PIDT$_{C20}$-BT, and PIDT$_{C16}$-TPD$_{C1}$ have higher $\mu_{,hole}$'s but are exceptionally brittle. These results demonstrate that side chain substitution of IDT-copolymers effects their ability to interdigitate, and thus, to align in parallel. As a result, IDT-copolymers with too dense of side chain attachment thereby display reduced $\mu_{,hole}$, reduced elastic modulus, and increased fracture strain.

3.3 Results and Discussion

Five different IDT-copolymer samples were prepared using direct arylation polymerization (Scheme 3.1 and Scheme 3.2). The structures of the IDT-copolymers are shown in Figure 3.1. There are two polymer samples with the PIDT$_{C16}$-BT backbone structure. They differ in the length of the alkyl side chain on the IDT unit of backbone. These two polymers, which are referred to as the BT-containing IDT-copolymers, are PIDT$_{C16}$-BT and PIDT$_{C20}$-BT due to the hexadecane (C_{16}) and isodecane (C_{20}) side chains covalently bound to the IDT monomer unit. Three polymer systems were synthesized with the PIDT$_{C16}$-TPD$_{C1}$ conjugated backbone structure. These systems, which are referred to as TPD-containing IDT copolymers, differ in the length and degree of branching of alkyl side chains stemming from the TPD monomer unit. These TPD-containing systems are referred to as PIDT$_{C16}$-

TPD_{C1}, $PIDT_{C16}$-TPD_{C8}, and $PIDT_{C16}$-TPD_{C13B} due to the methyl (C_1), octyl (C_8), and (6-ethyl)-undecane (C_{13B}) side chains that are covalently bound to the TPD monomer unit of each respective polymer. The "13B" notation of $PIDT_{C16}$-TPD_{C13B} signifies that the side chain contains 13-carbons in total and is branched. Each of the TPD-containing systems have IDT monomers with C_{16} side chains.

Un-alkylated IDT- and TPD-monomers, and the alkylated monomers IDT_{C16} and TPD_{C1}, were synthesized as previously reported.[53] The monomer IDT_{C20} was synthesized by alkylating the IDT core with 1-bromoicosane instead of 1-bromohexadecane (Scheme 3.4). The TPD_{C8} and TPD_{C13B} monomers were synthesized by alkylating the TPD core with 1-bromooctane and 6-(bromoethyl)-undecane, respectively, in place of methyl iodide (Scheme 3.3). Following our previously utilized procedures, direct arylation polymerization was used to synthesize $PIDT_{C16}$-BT, $PIDT_{C20}$-BT, $PIDT_{C16}$-TPD_{C1}, $PIDT_{C16}$-TPD_{C8}, and $PIDT_{C16}$-TPD_{C13B}.[133] These polymers were subjected to ^1H nuclear magnetic resonance spectroscopy (Figures Figure 3.19-3.26) and size exclusion chromatography to characterize their chemical structure and M_n. The degree of polymerization (D.P.) can be used to compare the size of each polymer system, given the fact that the mass of the donor-acceptor (D-A) repeat unit varies greatly due to the variation in alkyl chain content in each system. Based on D.P., all polymers can be designated as belonging to the low-molecular weight regime (Table 3.1).

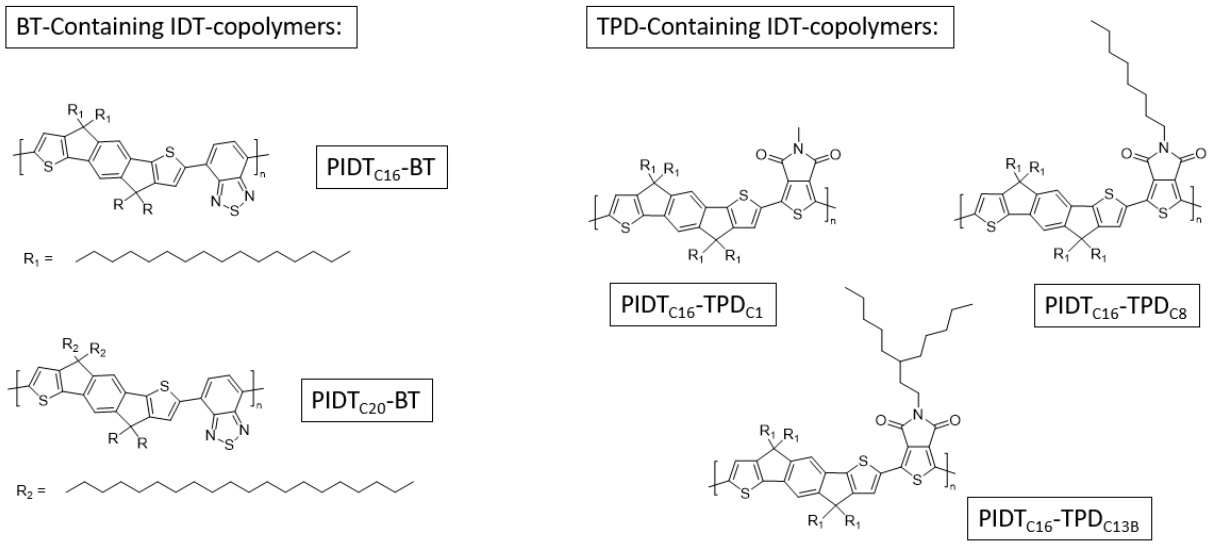

Figure 3.1. The structures of the BT-containing IDT copolymers which vary in the length of each side chain extending from the IDT monomer (left) and the TPD-containing IDT-copolymers which have the same side chains at the IDT monomer and vary in side chain character at the TPD-position. (right).

Table 3.1. Size exclusion chromatography results for each polymer system.

Polymer Sample	M_n (kg/mol)	$Đ$	Combined M.W. of Comonomer Units (u)	*D.P.*
PIDT$_{C16}$-BT	11000	1.8	1297	8
PIDT$_{C20}$-BT	21000	2.8	1521	14
PIDT$_{C16}$-TPD$_{C1}$	9000	1.7	1326	7
PIDT$_{C16}$-TPD$_{C8}$	11000	1.8	1426	8
PIDT$_{C16}$-TPDC$_{13B}$	14000	2.1	1496	9

GIWAXS measurements were performed to assess the crystallinity of each polymer system's thin films (Figure 3.12). As is expected for IDT copolymers, each polymer studied herein displayed

broad and diffuse crystallographic signals and can therefore be deemed near-amorphous.[85] There are no appreciable differences in the (010) or (100) signals between any of the polymers. The similarity in the (010) signal suggests that all of these copolymers show similar amounts of π-π interactions in their respective thin-films.

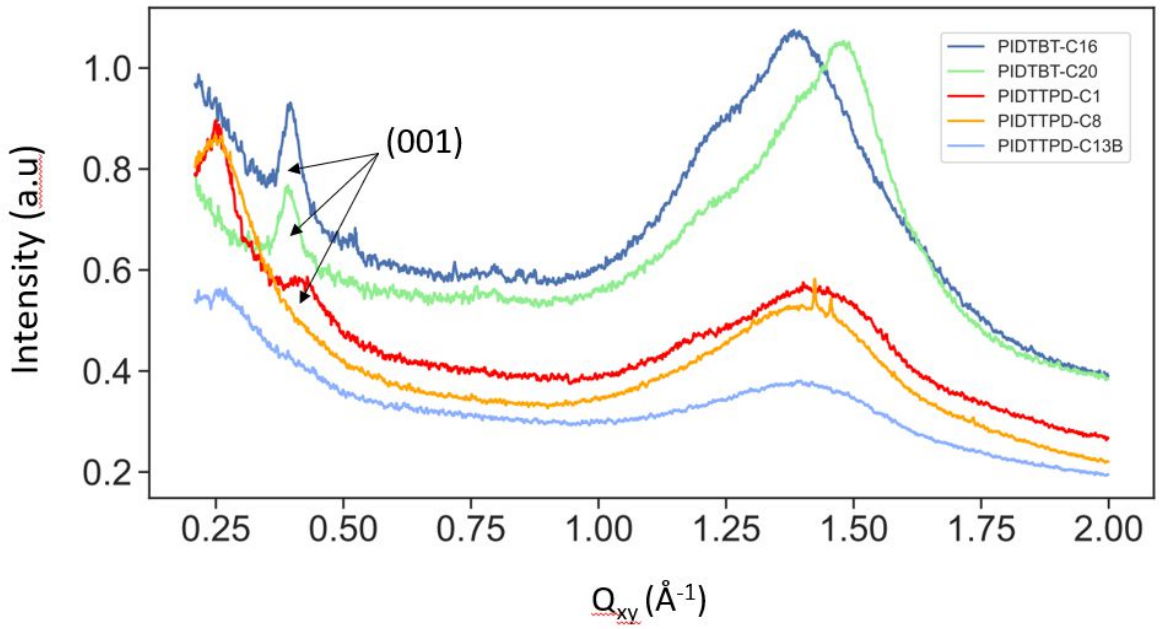

Figure 3.2. Linecuts of the 2D GIWAXS spectra in the Q_{xy} direction of each IDT-copolymer is shown. The (001) signal is labeled for clarity.

$PIDT_{C16}$-BT, $PIDT_{C20}$-BT, and $PIDT_{C16}$-TPD_{C1} displayed the (001) signal, which indicates the parallel arrangement of rigid IDT-copolymer segments.[134] The (001) peak position of the BT-containing systems is at a slightly higher Q-value than observed for $PIDT_{C16}$-TPD_{C1} due to slight differences in repeat unit length. It has been observed in scanning tunneling microscopy measurements that side chains of $PIDT_{C16}$-BT interdigitate tightly when aligned in parallel.[135] The interdigitation of alkyl side chains is perhaps a necessary condition for the parallel alignment of IDT copolymer backbones, and thus for the appearance of the (001) crystallite. Having long side chains on every monomer rather than every other monomer is effectively an increase in the side chain attachment

density, which has been shown to inhibit interdigitation of CPs.[70] Thus, it is reasonable to suggest that the lack of appearance of a (001) signal in PIDT$_{C16}$-TPD$_{C8}$ and PIDT$_{C16}$-TPD$_{C13B}$ thin films is due to the long, and branched in the case of PIDT$_{C16}$-TPD$_{C13B}$, alkyl side chains extending from the TPD monomers, which disrupts the uniform pattern by which side chains extend away from the IDT copolymer backbone when only the IDT monomer is alkylated. The regular extension of alkyl chains from the IDT monomer unit alone, provides enough space for interdigitation with side chains of neighboring, and parallelly aligned, polymers. Representations of interdigitating IDT-copolymers with lower side chain attachment density and non-interdigitating IDT-copolymers with increased side chain attachment density are shown in Figure 3.3a and Figure 3.3b respectively. While the existence of the (001) signal in a thin film arises from just a fraction of polymer chains, the parallel alignment of IDT copolymers is an arrangement that does impact the electronic properties of resultant thin-films,[134] and may impact the mechanical properties of IDT-copolymer thin films studied herein.

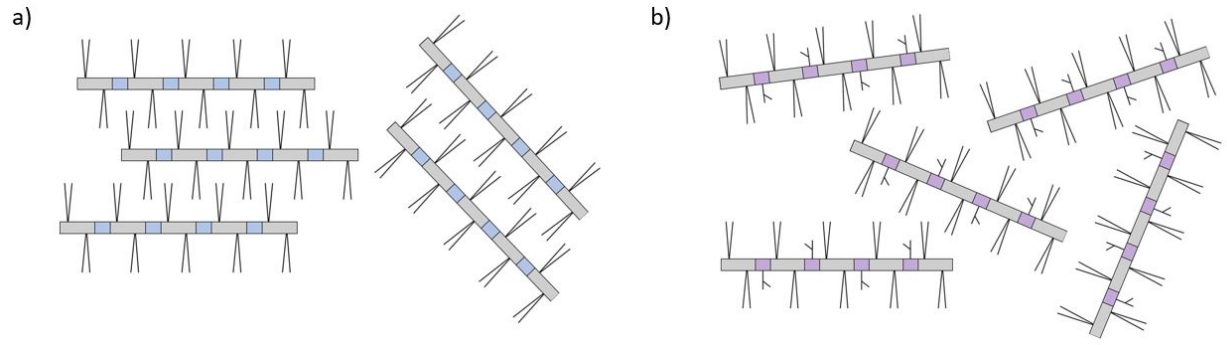

Figure 3.3. IDT-copolymers with side chains on only the IDT subunit (grey block) are able to interdigitate side chains and align in parallel (a) and IDT-copolymers with side chains on the IDT-monomer and TPD-monomer cannot interdigitate their side chains and therefore do not align in parallel (b).

Ultraviolet-visible light Absorbance (UV-Vis) and photoluminescence (PL) experiments were performed to see how the optoelectronic properties of the IDT-copolymers are impacted by side chain

substitution and to probe the conformational properties of each polymer system. UV-Vis and PL experiments were performed on each polymer system in chloroform solutions and thin-films cast from chloroform. The UV-Vis spectra of all polymers in solution and thin film are shown in Figure 3.4. Relevant metrics are tabulated in Table 3.2. Optoelectronic properties of each IDT-copolymer system.. BT-containing IDT-copolymers exhibit more pronounced redshifts in absorbance maximum than TPD-containing systems upon precipitation into thin-film from solution; suggesting that they undergo greater degrees of planarization in the solid state. In solution the BT-containing polymers have visible but less pronounced 0-0 transitions compared to the TPD-containing polymers, for which the transition is strongly pronounced. All polymers studied herein display a pronounced 0-0 transition in thin film. This 0-0 transition is indicative of J-aggregation behavior,[109] and has been observed in $PIDT_{C16}$-BT and $PIDT_{C16}$-TPD_{C1} previously.[53,133] The stokes shift of the TPD-containing IDT copolymers in solution is approximately half that of the BT-containing IDT copolymers. This suggests that the TPD-containing systems may in fact be more planar and rigid than the BT-containing systems,[136] which is in agreement with previously performed DFT calculations comparing $PIDT_{C16}$-BT to $PIDT_{C16}$-TPD_{C1}.[53] The similarity in stokes shift between $PIDT_{C16}$-TPD_{C1}, $PIDT_{C16}$-TPD_{C8}, and $PIDT_{C16}$-TPD_{C13B} is evidence that the planarity and rigidity is not altered by side chain substitution. Within each IDT copolymer family, the optoelectronic properties are strikingly alike, suggesting that side chain substitution at these positions minimally impacts the optoelectronic properties of IDT copolymers.

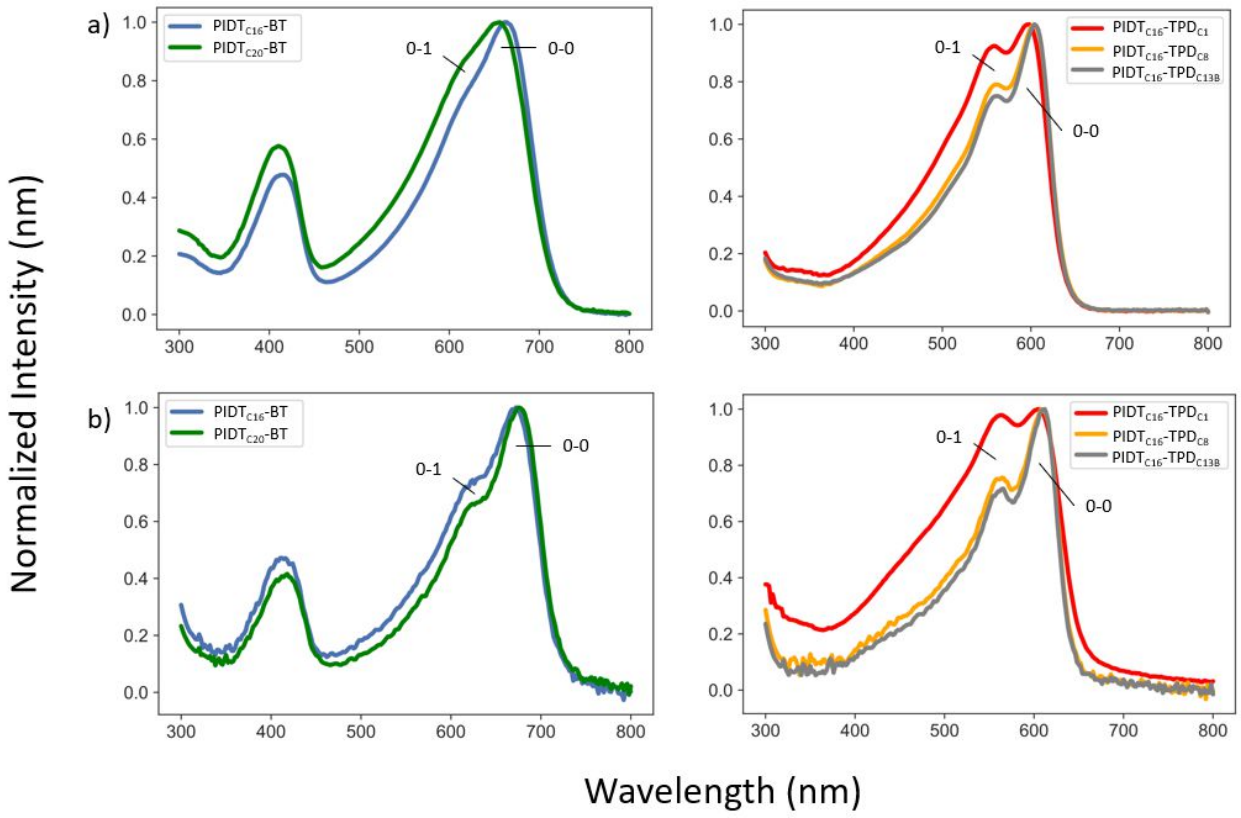

Figure 3.4. Solution (a) and thin-film (b) UV-Vis spectra for each IDT-copolymer.

Table 3.2. Optoelectronic properties of each IDT-copolymer system.

	Solution			Thin-film	
Sample	$\lambda_{max.Absorbance.}$ (nm)	$\lambda_{max.PL}$ (nm)	Stokes Shift (nm)	$\lambda_{max.abs.}$(nm)	Δ Solution to thin-film, Absorbance (nm)
PIDT$_{C16}$-BT	662	708	46	674	12
PIDT$_{C20}$-BT	656	705	49	676	20
PIDT$_{C16}$-TPD$_{C1}$	598	624	26	606	8
PIDT$_{C16}$-TPD$_{C8}$	604	626	22	608	4
PIDT$_{C16}$-TPDC$_{13B}$	604	626	22	612	8

To probe the thermal properties of these IDT copolymer systems fast-scanning calorimetry (FSC) was performed. The mechanical properties of conjugated polymers are known to be impacted

by the melting temperatures (T_m) and glass transition temperatures (T_g) of the material.[57] Intact crystallites and glassy morphologies both inhibit polymer chain reorganization during strain and lead to less stretchable thin films.[48] T_g values were determined through extrapolation of enthalpy recovery signatures from physical aging experiments (Figure 3.5). The T_g's of PIDT$_{C16}$-BT and PIDT$_{C20}$-BT were 10 °C and 20 °C respectively. The T_g's of PIDT$_{C16}$-TPD$_{C1}$ PIDT$_{C16}$-TPD$_{C8}$, PIDT$_{C16}$-TPD$_{C13B}$ were 31 °C, 4 °C and 0 °C respectively. The only system with an above-room temperature T_g is PIDT$_{C16}$-TPD$_{C1}$.For the four polymer systems which have T_g's less than room temperature, this signifies that reorganization of polymer chains is available to these systems at ambient temperatures. Decreasing T_g with increasing side-chain size is observed for the TPD-containing IDT-copolymers as has been observed for other conjugated polymer systems.[137] In contrast, for the BT-containing IDT-copolymers it is observed that elongation of the side chains on the IDT-monomer result in an increased T_g for PIDT$_{C20}$-BT compared to PIDT$_{C16}$-BT. It is possible that this result is derived from the side chains reaching a critical length, above which the relation inverses,[138] or due to its larger molecular weight.[139]

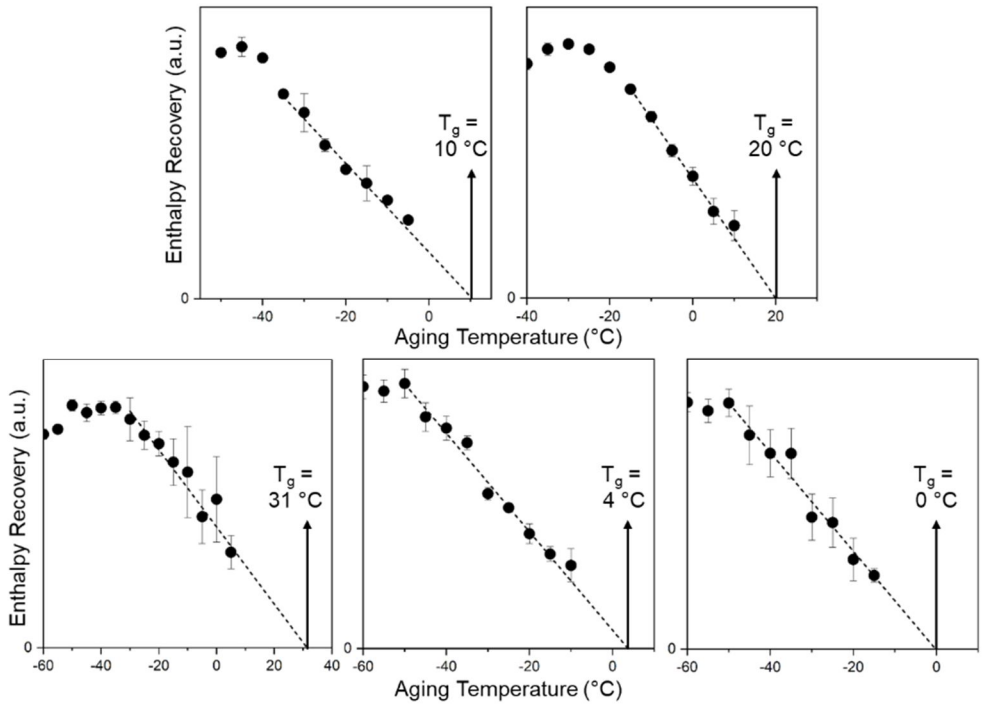

Figure 3.5. Enthalpic recovery curves of all IDT-copolymers with extrapolated T_g values.

The side chain softening temperature is known to impact the mechanical properties of conjugated polymer systems.[118] Annealing the polymer samples above their T_g's can be performed to induce organization of the side chains. Figure 3.11 displays the side-chain softening endotherms at about 20 and 50 °C for PIDT$_{C16}$-BT and PIDT$_{C20}$-BT, respectively. If thin-films of these materials are elongated at temperatures greater than their T_g but below their side-chain softening endotherm, there will be side-chain organizations which will hinder their ability to reorganize to some degree. The TPD-containing IDT-copolymers do not exhibit a side-chain softening endotherm. PIDT$_{C16}$-BT, PIDT$_{C20}$-BT, and PIDT$_{C16}$-TPD$_{C1}$ samples also exhibit a high temperature endotherm which is assigned to liquid-crystalline ordering of their backbones.[133] This ordering, which requires the parallel arrangement of neighboring polymer backbones is also apparent in the (001) signatures in GIWAXS measurements for PIDT$_{C16}$-BT, PIDT$_{C20}$-BT, and PIDT$_{C16}$-TPD$_{C1}$.

Mid-IR charge modulation spectroscopy (CMS) was performed probe the optical absorption of intrinsic, field-effect generated polarons, avoiding polaron interactions with dopant counter ions.[140] The CMS spectra of all IDT-copolymers is shown in Figure 3.6. Mid-IR polaron absorption is dominated by two broad peaks: the lower energy peak "A" centered below 1000 cm^{-1} and the higher energy peak "B" centered at 2000-3000 cm^{-1}. The intensity, spectral shape, and position of polaronic mid-IR transitions are sensitive to the nanoscale disorder experienced by charge carriers.[141,142] Generally, increases in the A/B peak ratio and associated red-shifting of the peaks correlate with polarons in more energetically ordered environments. All materials tested in this study show heavily red-shifted peak A's. Notably, the full shape of peak A sits beyond the edge of detection (below ~500 cm^{-1}) as can be seen especially in the TPD-containing polymers where the polaron absorption continuously increases from ~700cm^{-1} to 500cm^{-1}. Nevertheless, the significantly red-shifted peak A starkly contrasts behavior seen in classically semicrystalline polymers such as P3HT, where peak A is fully resolvable in the Mid-IR spectral range at ~700-1000cm^{-1}.[143] The red-shifting of peak A observed in both the BT and TPD-containing materials suggests that polarons are significantly delocalized in these polymers, and, in conjunction with the lack of a strong π-π stacking signal observed in GIWAXS of these polymers (Figure 3.12), we interpret this delocalization as predominantly intrachain. While peak A is not fully resolvable in this experiment, and so quantitative comparisons of peak A position cannot be made, we do note subtle differences in peak B. While a more quantitative analysis is beyond the scope of this current work, polaron absorption spectra suggest strongly that polarons experience significant intra-chain delocalization in both BT and TPD-containing materials, with possibly even greater intra-chain delocalization in the TPD-containing materials. This signifies that differences in OFET performance between these materials should primarily be ascribed to differences in their respective thin-film microstructure, which governs the ease of intermolecular transport.

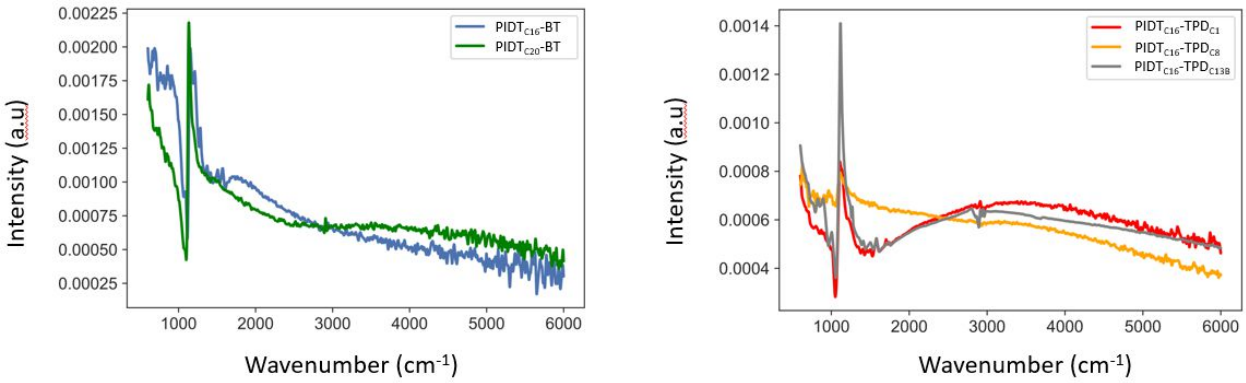

Figure 3.6. The CMS spectra of the BT-containing IDT copolymers (a) and TPD-containing IDT copolymers are shown.

Film on water measurements were performed to characterize and compare the mechanical properties of the IDT-copolymers under strain.[54] The stress-strain curves of all polymer systems except $PIDT_{C16}$-TPD_{C1} are shown in Figure 3.7 and their relevant mechanical metrics are tabulated in Table 2. $PIDT_{C16}$-TPD_{C1} was too brittle to load onto the strain stage for measurement (Figure 3.13). Comparing $PIDT_{C16}$-BT to $PIDT_{C20}$-BT, a slight increase in elongation at break is observed when increasing the length of the alkyl side chains on the IDT subunit. The $PIDT_{C16}$-BT sample effectively undergoes zero elastic deformation before fracture occurs. The $PIDT_{C20}$-BT sample does elastically deform until fracture is observed at 2% strain. It can be concluded that the reorganization of their respective thin film morphologies are inhibited by the interdigitation of its side chains which embrittle the material by preventing plastic flow.[144,145] The larger fracture strain of the brittle $PIDT_{C20}$-BT system compared to $PIDT_{C16}$-BT can be ascribed to its higher average D.P., rather than any significant internal plasticization from the longer side chains, which its increased T_g demonstrates is unlikely. $PIDT_{C16}$-TPD_{C1}, was brittle due the glassy morphology at room temperature. Increasing the length of the IDT-unit side chain does not lead to a significant decrease in elastic modulus because side chain

interdigitation was not inhibited, nor was the backbone of PIDT$_{C20}$-BT more plasticized than PIDT$_{C16}$-BT.

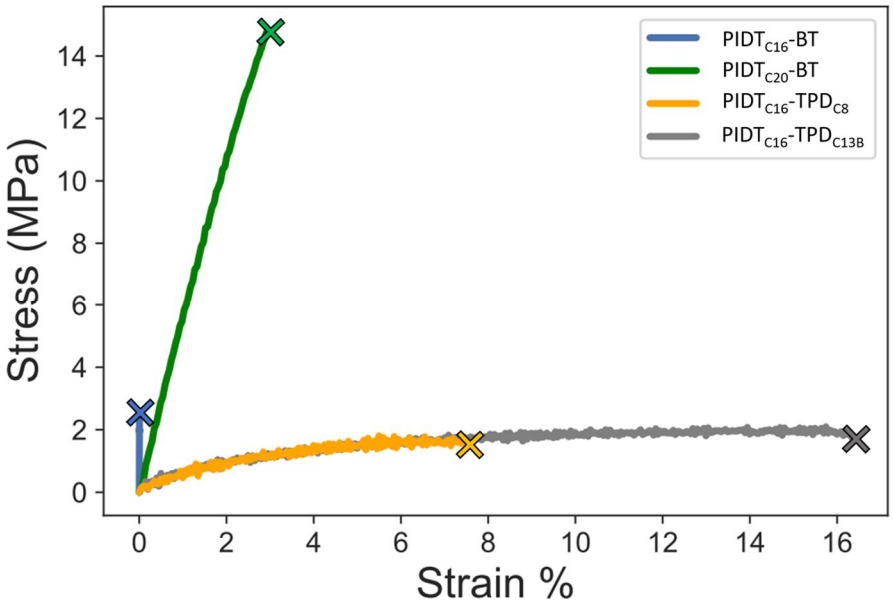

Figure 3.7. Representative stress-strain curves obtained through film-on-water elongation measurements for all IDT-copolymers except PIDT$_{C16}$-TPD$_{C1}$, which was too glassy to be tested. The colored 'X' on each line denotes fracture strain of each material for clarity.

In contrast, both PIDT$_{C16}$-TPD$_{C8}$ and PIDT$_{C16}$-TPD$_{C13B}$ were able to undergo plastic during elongation. As a result, these polymers displayed average elongation at break values of 7% and 16% for PIDT$_{C16}$-TPD$_{C8}$ and PIDT$_{C16}$-TPD$_{C13B}$, respectively. Side chain substitution at the TPD-position led to significant reductions in elastic moduli, with PIDT$_{C16}$-TPD$_{C8}$ and PIDT$_{C16}$-TPD$_{C13B}$ displaying an elastic moduli of 14 MPa and 50 MPa respectively. These elastic moduli values are remarkably small despite their backbone rigidity. These improvements increase their suitability in wearable or e-skin devices due to a modulus which more closely reflects that of skin.[146] The decreased elastic moduli of PIDT$_{C16}$-TPD$_{C8}$ and PIDT$_{C16}$-TPD$_{C13B}$ and demonstration of plastic deformation, is due to the inhibition of side chain interdigitation through the inclusion of longer side chains on the TPD unit.[147] From a structural perspective, it is the increased attachment density of alkyl side chains on PIDT$_{C16}$-

TPD_{C8} and $PIDT_{C16B}$-TPD_{C13B} that inhibits interdigitation and provides these materials a greater ability to reorganize polymers within thin films through plastic deformation.[70] Interestingly, inclusion of the branching side chain leads to an increase in elastic modulus, signifying that there may be increased interactions between the branched side chain on the TPD monomer and other side chains in the system. Slight increases in elastic moduli have been observed in prior studies of donor-acceptor copolymers when swapping linear for branched side chains.[148] The fracture strain of $PIDT_{C16}$-TPD_{C13B} compared to $PIDT_{C16}$-TPD_{C8} is potentially due to the larger and branched side chain of the TPD_{C13B} monomer shielding the polymer backbone more than the linear side chain of the TPD_{C8} monomer. By increasing the attachment density of alkyl side chains from every other to every monomer repeat unit, through inclusion of long alkyl side chains on the TPD unit, IDT copolymers can be made more stretchable and with significantly decreased elastic moduli. This occurs because of inhibited interdigitation of side chains and thus more facile reorganization of polymer chains during elongation.

Table 3.3. The mechanical properties and $\mu_{,hole}$ of each IDT-copolymer are tabulated.

Name	M_n (kg/mol)	D.P.	Elastic modulus (MPa)	Avg. Elongation at break (%)	$\mu_{,hole}$ ($cm^2 \cdot V^{-1} \cdot s^{-1}$)
$PIDT_{C16}$-BT	11	8	N.A. [a]	0 ± 0	0.068 ± 0.020
$PIDT_{C20}$-BT	21	14	520 ± 70	2 ± 1	0.023 ± 0.003
$PIDT_{C16}$-TPD_{C1}	8	7	N.A. [b]	N.A.[b]	0.051 ± 0.030
$PIDT_{C16}$-TPD_{C8}	11	8	14 ± 2	7 ± 2	0.007 ± 0.005
$PIDT_{C16}$-$TPDC_{13B}$	14	9	56 ± 5	16 ± 4	0.006 ± 0.002

[a]The elastic moduli of $PIDT_{C16}$-BT is effectively infinite because of the verticality of the stress strain curve

[b]The $PIDT_{C16}$-TPD_{C1} material was too glassy to be loaded onto the strain stage for measurement.

OFETs were fabricated so that the electronic properties of each IDT copolymer could be assessed. These results are displayed in Table 3.4. OFET data is reported for all IDT-copolymers.. All polymer samples display threshold voltages similar to our previous reports on IDT-copolymers.[133]

When assessing average $\mu_{,hole}$, lengthening of alkyl side chains decreases the $\mu_{,hole}$ and on/off current ratio in every case. The $\mu_{,hole}$'s of PIDT$_{C20}$-BT and PIDT$_{C16}$-BT remain on the same order of magnitude. In contrast, the $\mu_{,hole}$'s of PIDT$_{C16}$-TPD$_{C8}$ and PIDT$_{C16}$-TPD$_{C13B}$ are reduced by an order of magnitude compared to PIDT$_{C16}$-TPD$_{C1}$. It is observed that PIDT$_{C16}$-TPD$_{C1}$ and PIDT$_{C16}$-BT have the same OFET characteristics, which corroborates our previous reports.[53] The CMS results demonstrate that the BT-containing and TPD-containing IDT copolymers have similar polaron delocalization under static charge accumulation. If the electronic environment of polarons within the thin films are similar, then this indicates that the intra-molecular charge transport may be unaffected by side chain substitution at the TPD-nitrogen position. Thus, decreases in $\mu_{,hole}$ are due to an lessened ability to form intermolecular arrangements that facilitate intermolecular charge transport. The inhibited arrangements may be the parallel alignment of chains that resultantly allows for lamellar crossing of parallelly aligned polymer backbones that presumably pervade the films of PIDT$_{C16}$-TPD$_{C1}$, PIDT$_{C20}$-BT and PIDT$_{C16}$-BT.[134] In this way, the inability to interdigitate side chains, and thus form parallel chain arrangements is directly responsible for the decrease in $\mu_{,hole}$ of PIDT$_{C16}$-TPD$_{C8}$ and PIDT$_{C16}$-TPD$_{C13B}$.

3.5 Conclusion

Increasing the side chain attachment density of IDT-copolymers from every other monomer to every monomer has widespread effects on electronic and mechanical properties of their thin films. With increased side chain attachment density comes an inability for neighboring polymer backbones to interdigitate side chains. This is supported by the lack of the (001) crystallographic signal in PIDT$_{C16}$-TPD$_{C8}$ and PIDT$_{C16}$-TPD$_{C13B}$, which suggests they have an inability to form parallel arrangements of backbones, and the lack of side chain ordering observed in FSC experiments, which suggests that the increased side chain attachment density

is inhibiting side chain organization. As a consequence, these systems display order of magnitude lesser $\mu_{,hole}$'s than PIDT$_{C16}$-BT, PIDT$_{C20}$-BT, and PIDT$_{C16}$-TPD$_{C1}$, which do exhibit interdigitation of their side chains and thus display parallel ordering of their backbones. In contrast, because of their inability to interdigitate side chains PIDT$_{C16}$-TPD$_{C8}$ and PIDT$_{C16}$-TPD$_{C16}$ thin-films can dissipate strain through plastic deformation; exhibiting greatly improved fracture strains and remarkably low elastic moduli. This suggests that side chain interdigitation is a major contributor to preventing polymer chain reorganization of IDT-copolymers while under strain. Inhibition of interdigitation can endow planar IDT-copolymers with reduced elastic moduli and the ability deform plastically under strain.

3.6 Supplementary Information

3.6.1 Chemical synthesis

All chemicals used in this study were obtained through commercial sources and used as received. All reactions were performed in air unless otherwise specified.

Synthesis of TPD-Br$_2$

1,3-Dibromothieno[3,4-c]pyrrole-4,6-dione

This was performed as reported previously.[150]

Synthesis of TPD$_{C1}$-Br$_2$

1,3-dibromo-5-methyl-4H-thieno[3,4-c]pyrrole-4,6(5H)-dione

This was performed as reported previously.[53]

Synthesis of monomer TPD_{C8}-Br_2

(1,3-dibromo-5-octyl-4H-thieno[3,4-c]pyrrole-4,6(5H)-dione)

(311 mg, 1 mmol), K_2CO_3 (276 mg, 2 mmol), and 10 of DMF (anhydrous) collected from a solvent still under nitrogen atmosphere. After 10 minutes of stirring, dropwise addition of 1-bromooctane (0.26 mL, 1.5 mmol) was performed. The reaction was then stirred at room temperature for 16 hours. The reaction was gravity filtered and concentrated using rotary evaporation. Silica gel chromatography was performed using 1:5 EtOAc:$CHCl_3$ as the eluent mixture. Following recrystallization in chloroform and methanol, white crystals were afforded in 71% yield. ^{1}H NMR (500 MHz, CDCl3, δ, ppm): 3.07 (t, 2H), 1.10-0.34 (m, 15H).

Synthesis of monomer TPD_{C13B}-Br_2

(1,3-dibromo-5-(6-ethyl-undecane)-4H-thieno[3,4-c]pyrrole-4,6(5H)-dione)

To an oven-dried and gas-degassed 3-neck round bottom flask was charged TPD-Br_2 (250 mg, 0.94 mmol), K_2CO_3 (259mg, 1.88 mmol), and 12mL of DMF (anhydrous) collected from a solvent still under nitrogen atmosphere. After 10 minutes of stirring, dropwise addition of 5-(2-bromoethyl)-undecane (370mg, 1.41mmol) was performed. The reaction was then stirred at room temperature for 16 hours. The reaction was gravity filtered and concentrated using rotary evaporation. Silica gel chromatography was performed using 1:5 EtOAc:$CHCl_3$ as the eluent mixture. Following recrystallization in chloroform and methanol, white crystals were afforded in 63% yield. ^{1}H NMR (500 MHz, CDCl3, δ, ppm): 3.61 (t, 2H), 1.61 (m, 2H), 1.26 (m, 17H), 0.88 (m, 6H).

Synthesis of monomer IDT_{C20}

(4,4,9,9-tetraicosane-4,9-dihydro-s-indaceno[1,2-b:5,6-b']dithiophene)

This synthesis was performed in accordance with the synthesis of monomer TPD_{C1} as previously reported,[53] but using a different alkyl-halide than 1-bromohexadecane. To an oven-dried 3-neck round bottom flask was charged IDT-scaffold (200mg, 0.8 mmol), sodium tert-butoxide (366, 3.8 mmol), 15mL of 1:1 DMSO:Toluene (anhydrous). This was stirred and heated to 80 °C in an oil bath for 1 hours. 1-bromohexadecane (1379.3mg, 3.8mmol) was dissolved in the solvent mixture and added dropwise to the reaction vessel. The material was subjected to silica gel chromatography using hexanes as the eluent. The solid was recrystallized in hexanes, to afford a white/yellow solid in 42% yield. ^{1}H NMR (500 MHz, CDCl3, δ, ppm): 7.27 (s, 2H), 7.25 (s,2H), 6.96 (s, 2H), 2.02 (s, 4H), 1.87 (s, 4H), 1.26 (m, 144H), 0.89 (t, 12H).

Synthesis of IDT-scaffold

(4,9-dihydro-s-indaceno[1,2-b:5,6-b']dithiophene)

This was performed as reported previously.[53]

Synthesis of $PIDT_{C16}$-BT

(poly(4-methyl-7-(4,4,9,9-tetrahexadecyl-7-methyl-4,9-dihydro-s-indaceno[1,2-b:5,6-b']dithiophen-2-yl)benzo[c][1,2,5]thiadiazole))

This was performed as reported previously.[53] A mixture of IDT_{C16} (58.2 mg, 0.05 mmol), $BT\text{-}Br_2$ (14.7 mg, 0.05 mmol), tris(dibenzylideneacetone)dipalladium(0) (2.3 mg, 5 mol%), tris(o-anisyl)phosphine (1.8 mg, 10 mol%), cesium carbonate (81 mg, 0.25 mmol) and pivalic acid (2.6 mg, 0.025 mmol) in o-xylene (1 mL) was degassed and filled with nitrogen in a pressure reaction tube. The tube was sealed and the mixture was heated at 100 °C for 16 h, followed by being cooled to room temperature and precipitated into methanol (100 mL). The precipitate was filtered through a Soxhlet

thimble and then purified by Soxhlet extraction with methanol, acetone and hexanes. The hexanes fraction was collected and the solvent was removed by rotary evaporation. The residue was dissolved in chloroform and precipitated into methanol. The precipitate was collected by filtration and dried under vacuum to afford a deep blue solid in 68% yield. (500 MHz, CDCl3, δ, ppm): 8.10 (s, 2H), 7.95 (s, 2H), 7.39 (s, 2H), 2.09 (s, 4H), 1.96 (s, 4H), 1.17 (m, 112H), 0.85 (t, 12H).

Synthesis of PIDT$_{C20}$-BT

(poly(4-methyl-7-(4,4,9,9-tetraicosane-7-methyl-4,9-dihydro-s-indaceno[1,2-b:5,6-b']dithiophen-2-yl)benzo[c][1,2,5]thiadiazole))

This was performed as reported previously,[53] except the IDT$_{C16}$ monomer was swapped with the IDT$_{C20}$ monomer and used in equimolar amount relative to the IDT$_{C16}$ monomer. A mixture of IDT$_{C20}$ (mg, mmol), BT-Br$_2$ (14.7 mg, 0.05 mmol), tris(dibenzylideneacetone)dipalladium(0) (2.3 mg, 5 mol%), tris(o-anisyl)phosphine (1.8 mg, 10 mol%), cesium carbonate (81 mg, 0.25 mmol) and pivalic acid (2.6 mg, 0.025 mmol) in o-xylene (1 mL) was degassed and filled with nitrogen in a pressure reaction tube. The tube was sealed and the mixture was heated at 100 °C for 16 h, followed by being cooled to room temperature and precipitated into methanol (100 mL). The precipitate was filtered through a Soxhlet thimble and then purified by Soxhlet extraction with methanol, acetone and hexanes. The hexanes fraction was collected and the solvent was removed by rotary evaporation. The residue was dissolved in chloroform and precipitated into methanol. The precipitate was collected by filtration and dried under vacuum to afford a deep blue solid in 74% yield. ^{1}H NMR (500 MHz, CDCl3, δ, ppm): 8.09 (s, 2H), 7.94 (s, 2H), 7.39 (s, 2H), 2.10 (s, 4H), 1.96 (s, 4H), 1.23 (m, 144H), 0.87 (t, 12H).

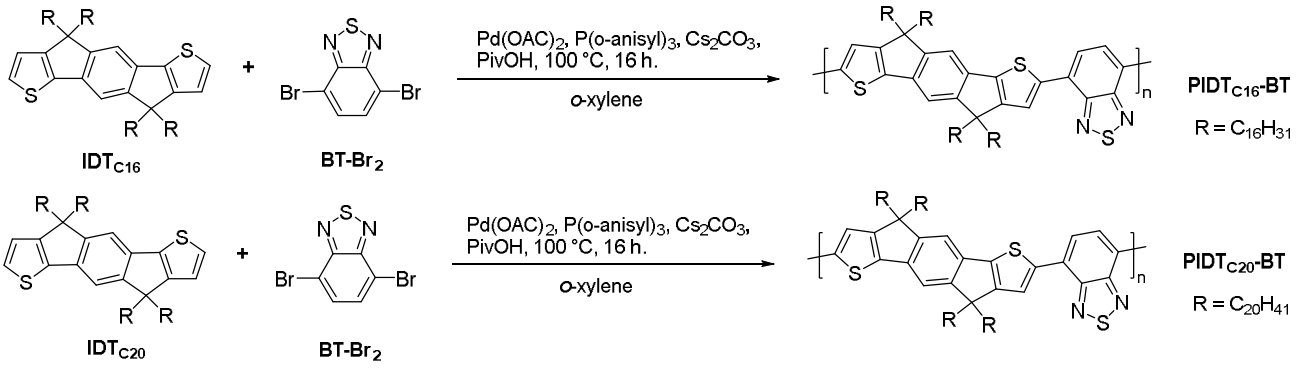

Scheme 3.1. Synthesis of BT-containing IDT-copolymers.

Synthesis of PIDT$_{C16}$-TPD$_{C1}$

(poly(5-methyl-1-(4,4,9,9-tetrahexadecyl-4,9-dihydro-s-indaceno[1,2-b:5,6-b']dithiophen-2-yl)-4H-thieno[3,4-c]pyrrole-4,6(5H)-dione))

This was performed as reported previously.[53]

A mixture of IDT$_{C16}$ (58.2 mg, 0.05 mmol), TPD$_{C1}$-Br$_2$ (16.2 mg, 0.05 mmol), tris(dibenzylideneacetone)dipalladium(0) (2.3 mg, 5 mol%), tris(o-anisyl)phosphine (1.8 mg, 10 mol%), cesium carbonate (81 mg, 0.25 mmol) and pivalic acid (2.6 mg, 0.025 mmol) in o-xylene (1 mL) was degassed and filled with nitrogen in a pressure reaction tube. The tube was sealed and the mixture was heated at 100 °C for 16 h, followed by being cooled to room temperature and precipitated into methanol (100 mL). The precipitate was filtered through a Soxhlet thimble and then purified by Soxhlet extraction with methanol, acetone and hexanes. The hexanes fraction was collected and the solvent was removed by rotary evaporation. The residue was dissolved in chloroform and precipitated into methanol. The precipitate was collected by filtration and dried under vacuum to afford a deep purple solid in 55% yield. (500 MHz, CDCl3, δ, ppm): 7.98 (s, 2H), 7.38 (s, 2H), 3.25 (s, 3H), 2.07 (s, 4H), 1.93 (s, 4H), 1.22-1.14 (m, 112H), 0.87-0.85 (t, 12H).

Synthesis of $PIDT_{C16}$-TPD_{C8}

(poly(5-octyl-1-(4,4,9,9-tetrahexadecyl-4,9-dihydro-s-indaceno[1,2-b:5,6-b']dithiophen-2-yl)-4H-thieno[3,4-c]pyrrole-4,6(5H)-dione))

This was performed as reported previously,[53] except the TPD_{C1} monomer was swapped with the TPD_{C8} monomer and used in equimolar amount relative to the IDT_{C16} monomer. A mixture of IDT_{C16} (95 mg, 0.08 mmol), TPD_{C1}-Br_2 (34.2 mg, 0.08 mmol), tris(dibenzylideneacetone)dipalladium(0) (3.7 mg, 5 mol%), tris(o-anisyl)phosphine (2.8 mg, 10 mol%), cesium carbonate (132 mg, 0.38 mmol) and pivalic acid (4.1 mg, 0.025 mmol) in o-xylene (1 mL) was degassed and filled with nitrogen in a pressure reaction tube. The tube was sealed and the mixture was heated at 100 °C for 16 h, followed by being cooled to room temperature and precipitated into methanol (100 mL). The precipitate was filtered through a Soxhlet thimble and then purified by Soxhlet extraction with methanol, acetone and hexanes. The hexanes fraction was collected and the solvent was removed by rotary evaporation. The residue was dissolved in chloroform and precipitated into methanol. The precipitate was collected by filtration and dried under vacuum to afford a deep purple solid in 58% yield. ^{1}H NMR (500 MHz, CDCl3, δ, ppm): 7.93 (s, 2H), 7.37 (s, 2H), 3.72 (t, 3H), 2.06 (s, 4H), 1.93 (s, 4H), 1.22 (m, 115H), 0.95 (t, 3H), 0.86 (12H).

Synthesis of $PIDT_{C16}$-TPD_{C13B}

(poly(5-(6-ethyl-undecane)-1-(4,4,9,9-tetrahexadecyl-4,9-dihydro-s-indaceno[1,2-b:5,6-b']dithiophen-2-yl)-4H-thieno[3,4-c]pyrrole-4,6(5H)-dione))

This was performed as reported previously,[53] except the TPD_{C1} monomer was swapped with the TPD_{C13B} monomer and used in equimolar amount relative to the IDT_{C16} monomer. A mixture of IDT_{C16}

(90 mg, 0.08 mmol), TPD_{C1}-Br_2 (37.9 mg, 0.08 mmol), tris(dibenzylideneacetone)dipalladium(0) (3.5 mg, 5 mol%), tris(o-anisyl)phosphine (2.7 mg, 10 mol%), cesium carbonate (125 mg, 0.38 mmol) and pivalic acid (3.9 mg, 0.025 mmol) in o-xylene (1 mL) was degassed and filled with nitrogen in a pressure reaction tube. The tube was sealed and the mixture was heated at 100 °C for 16 h, followed by being cooled to room temperature and precipitated into methanol (100 mL). The precipitate was filtered through a Soxhlet thimble and then purified by Soxhlet extraction with methanol, acetone and hexanes. The hexanes fraction was collected and the solvent was removed by rotary evaporation. The residue was dissolved in chloroform and precipitated into methanol. The precipitate was collected by filtration and dried under vacuum to afford a deep purple solid in 66% yield. ^{1}H NMR (500 MHz, CDCl3, δ, ppm): 7.89 (s, 2H), 7.37 (s,2H), 6.96 (s, 2H), 3.74 (s, 2H), 2.06 (s. 4H), 1.93 (s, 4H), 1.22 (m, 123H), 0.90 (m, 6H), 0.84 (m, 12H).

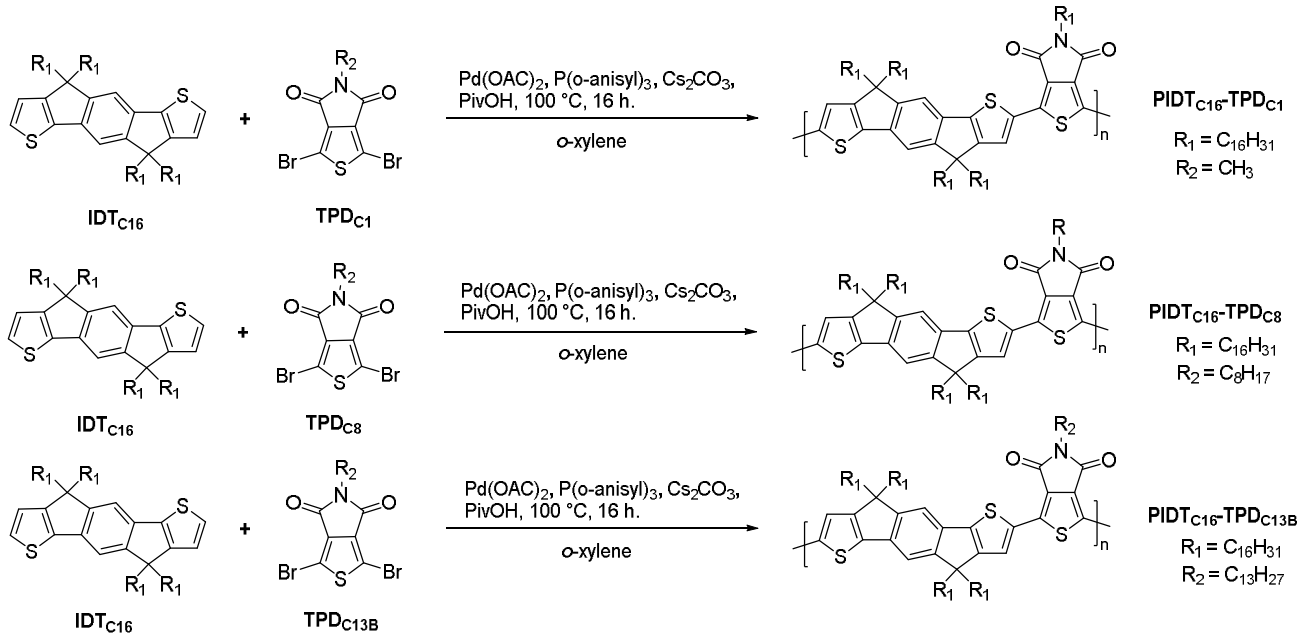

Scheme 3.2. Synthesis of TPD-containing IDT-copolymers.

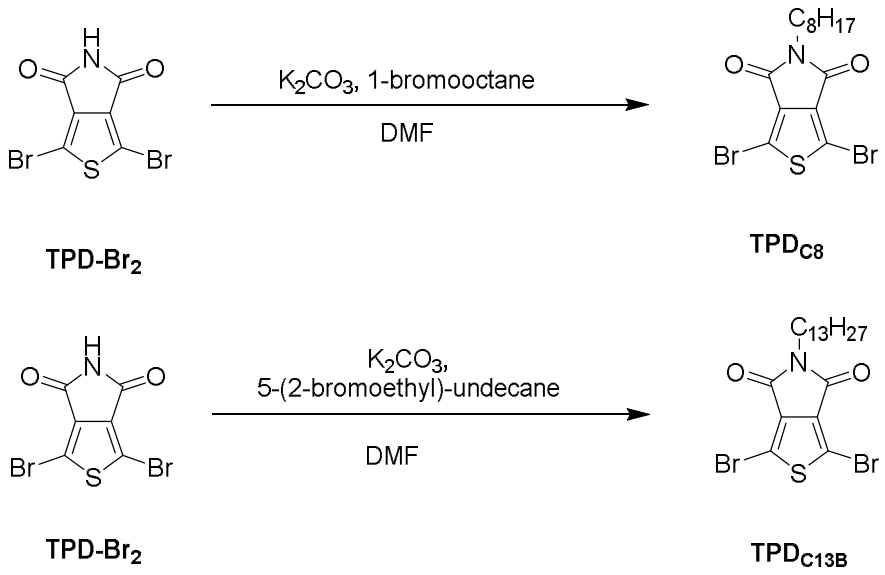

Scheme 3.3. Synthesis of monomers TPD_{C8} and TPD_{C13B}.

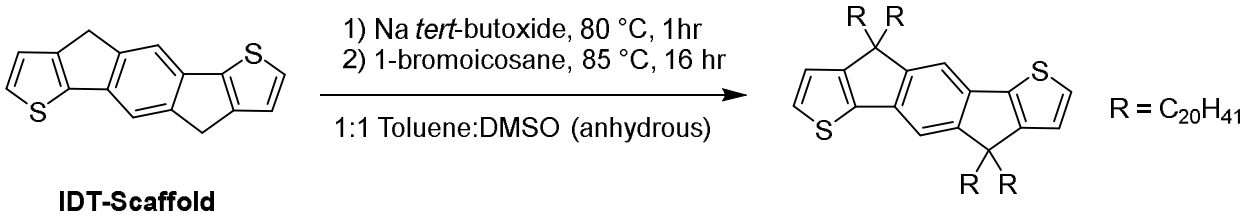

Scheme 3.4. Synthesis of monomer IDT_{C20}.

3.6.2 Size exclusion chromatography (SEC) characterization

The polymer molecular weights (vs. narrow dispersity polystyrene standards) were determined using a Viscotek TDA 305 gel permeation chromatography (GPC) system with combined UV detector at 30 °C, using chlorobenzene at a flow rate of 0.5 mL/min as the eluent.

3.6.3 Optoelectronic measurements

UV-Vis and PL spectra were measured on a Varian Cary 5000 UV-Vis-NIR spectrometer and a Horiba Fluorolog FL-3 spectrometer, respectively. Solution measurements were performed in

chloroform solutions with a polymer concentration of 0.05 mg/mL. Thin films used for measurement were spin cast from a chloroform solution with a polymer concentration of 5 mg/mL onto cut glass substrates.

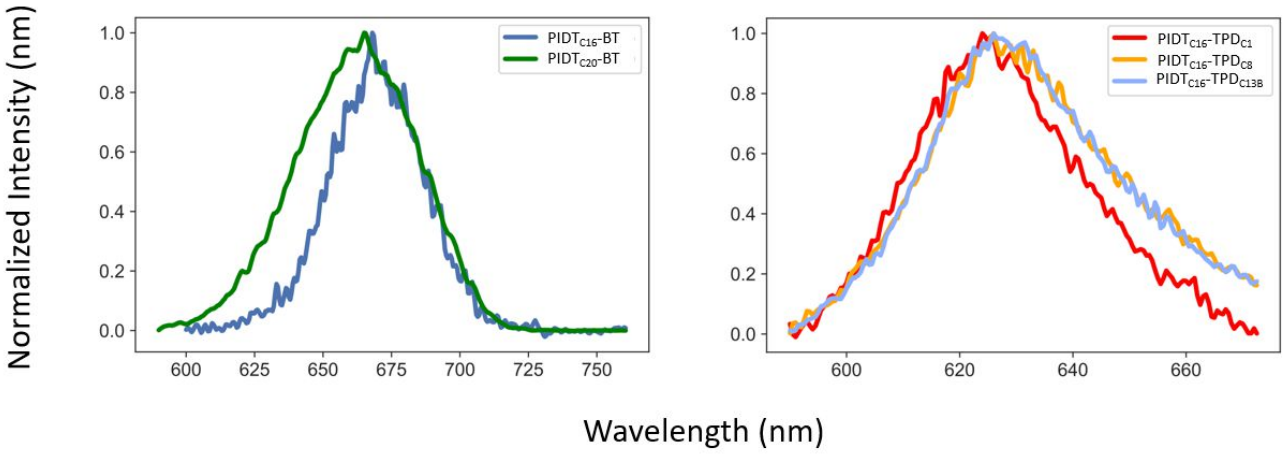

Figure 3.8. Solution PL for all IDT-copolymers.

3.6.4 Fast Scanning Calorimetry (FSC)

Fast Scanning Calorimetry was conducted under nitrogen using a Mettler Toledo Flash DSC 1 equipped with a Huber TC100 cooler to control the temperature between -90 and +450 °C. Powder samples of the polymers were deposited onto Flash DSC chips. Samples were subjected to a thermal aging process via 30 minute isotherms in the range of -90 to +200 °C, followed by 2 sequences of 4000 °C/s heating and cooling from -90°C to +350 °C. The overshoot between the heat flow of the first heating and second heating was used to calculate the glass transition temperature. Further information on experimental procedures can be found in reference 117.

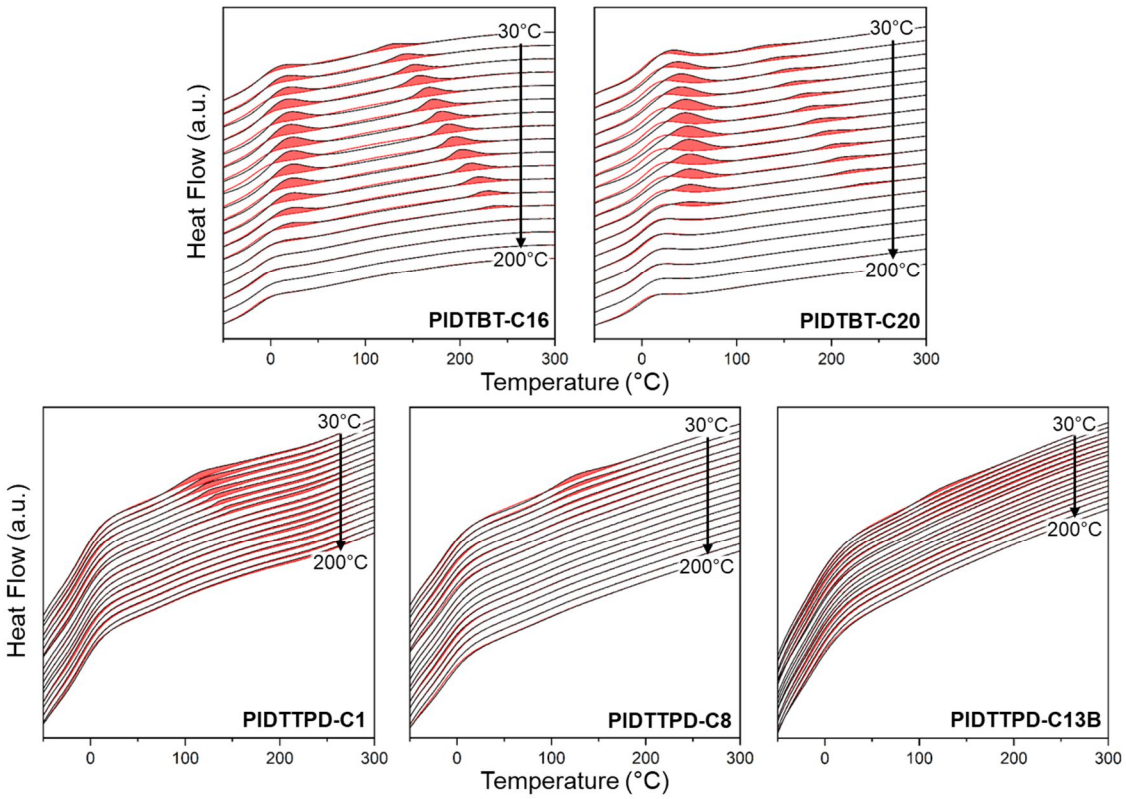

Figure 3.9. Fast Scanning Calorimetry of Annealed IDT series. Heating traces of annealed (black) and reference (red) lines IDT copolymers with annealing temperatures listed on the right side in increments of 10 degrees °C. PIDT$_{C16}$-BT copolymers show side-chain softening and liquid-crystalline-like melting peaks with annealing, while PIDT$_{C16}$-BPD$_{C1}$ copolymers show weak endotherms that indicate limited liquid-crystalline-like ordering, but no side-chain softening peaks.

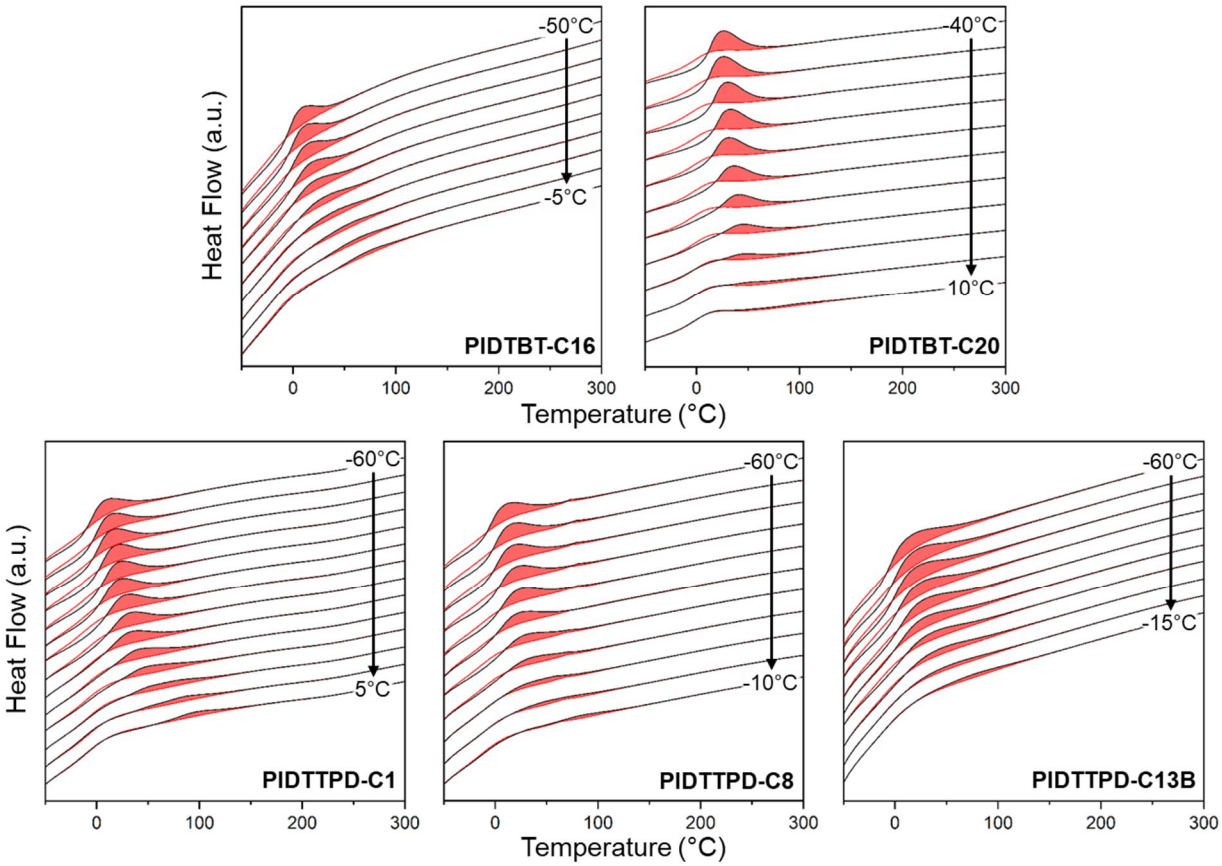

Figure 3.10. Physical Aging of Planar IDT Copolymers. Heating traces of annealed (black) and reference (red) lines IDT copolymers with aging temperatures listed on the right side in increments of 10 degrees °C.

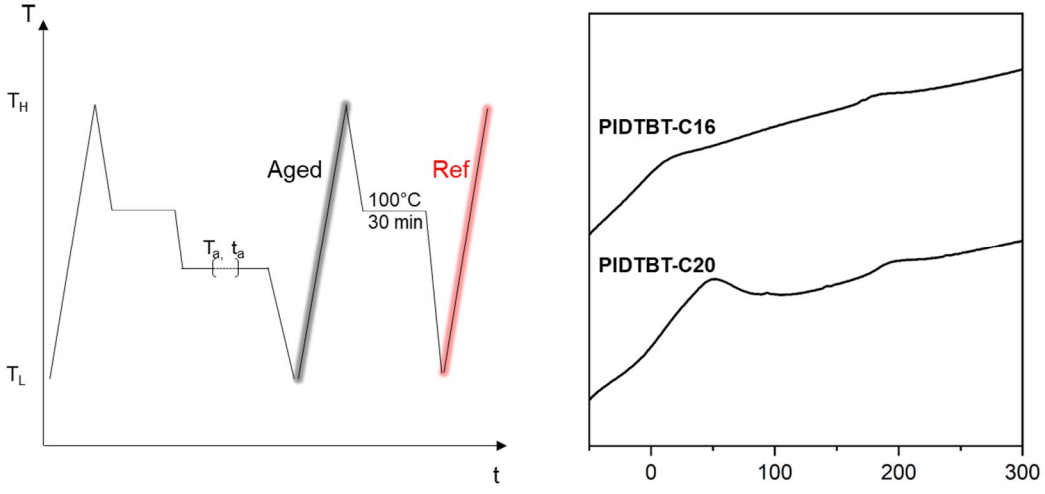

Figure 3.11. Annealing and Aging Protocol for Side-chain crystal ordering. (left) Flash DSC annealing and aging protocol in create side-chain crystals and then age below the glass transition temperature (right) Flash DSC reference curves from annealing protocol. $PIDT_{C16}$-BT and $PIDT_{C16}$-BT_{C20} both show side-chain softening endotherms and liquid-crystalline-like melting endotherms.

3.6.5 Crystallographic measurements

Grazing incidence wide-angle x-ray scattering (GIWAXS) measurements are conducted at Stanford Synchrotron Radiation Lightsource, SLAC National Accelerator Laboratory, Beamline 11-3. An incident x-ray energy of 12.7 keV was used. The incidence angle α of the x-ray beam was 0.1°. Scattering intensity was detected with a Rayonix MX225 CCD 2D area detector, and sample to detector distance was calibrated with a LaB6 polycrystalline standard. Data is reported in terms of the scattering vector, $q = (4\pi/\lambda)\sin(\theta)$, where θ is the angle of scattering. GIWAXS raw data was corrected for distortions introduced by the area detector with Nika 1D SAXS2 and WAXStools3 software packages in Igor Pro. Polymer films for GIWAXS were prepared in the same method as those prepared for CMS described above.

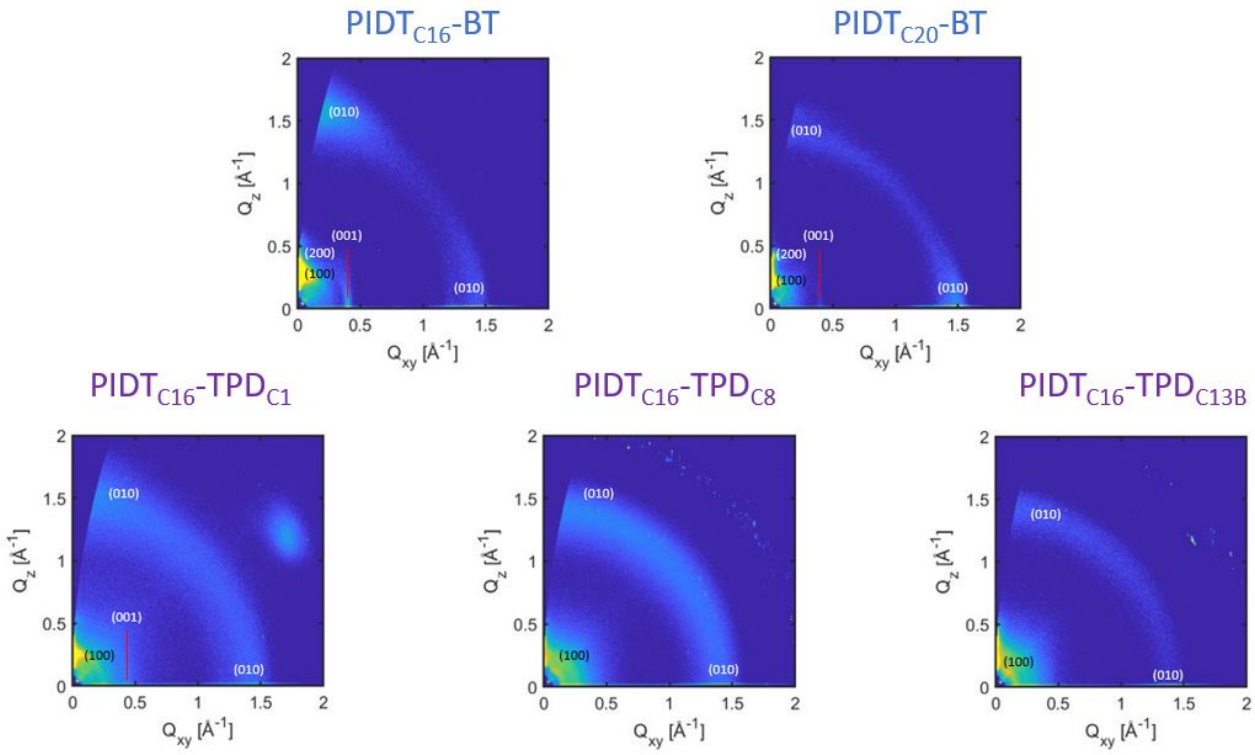

Figure 3.12. 2D GIWAXS spectra for all polymer systems.

3.6.6 Charge Modulation Spectroscopy (CMS)

CMS devices were prepared on lightly doped n-Type silicon with a thermally grown SiO2 dielectric layer (ρ = 1 to 10 ohm-cm). Substrates were cleaned using acetone, methanol, and isopropanol, followed by UV-Ozone cleaning for 20 minutes. All substrates were prepared with an octadecyltrichlorosilane (OTS) treatment to the SiO2 dielectric. OTS treatments were performed by placing substrates in a 40 mM solution of OTS in hexanes (mixture of isomers) in a nitrogen glovebox (O2 < 0.5 ppm). Substrates were left for 16 hours, and then removed to ambient to be sonicated in toluene for 1 minute, followed by rinsing with isopropanol and drying with a nitrogen stream. Substrates were then transferred to a nitrogen glovebox (O2 < 0.5 ppm) where all remaining processing steps occurred. The OTS treated substrates were annealed at 130oC for 15 minutes prior to spin-coating

polymer solutions. All polymer solutions for CMS device preparation were prepared at a concentration of 5 mg ml-1 in chloroform. All solutions were stirred for 48 hours at 55 oC prior to spin-coating. Dynamic Spin coating was performed at 2000 rpm for 60 seconds to yield polymer films of approximately 50 nm. To generate the necessary electrical contacts for CMS, a 15 nm semi-transparent gold contact was evaporated onto the polymer surface, and a 75 nm silver contact was evaporated onto a region of exposed silicon where the SiO2 dielectric layer was scratched through using a diamond scribe to form the device gate contact. CMS devices were then loaded into a home-built nitrogen chamber with KBr infrared transparent windows to perform the necessary spectroscopy measurements. The CMS measurement was performed by biasing CMS devices to V_g = -40V in accumulation and V_g = +10V in depletion. Vg is the gate bias applied to the silicon substrate. The differential infrared spectrum (ΔT/T) were performed to accumulate at least 12,000 individual spectral averages using a Nicolet iS50R Fourier Transform IR spectrometer. A Keithley K2400 was used to apply the gate biases. Device biasing and spectral acquisition were controlled with a home-built LabView code.

Differential spectra are reported as (ΔT/T), given by the Equation 3:

$$\frac{\Delta T}{T} = \frac{T_{accumulation} - T_{depletion}}{T_{neutral}} \quad (3)$$

where $T_{accumulation}$ and $T_{depletion}$ represent the IR transmission through the CMS sample under accumulation and depletion carrier regimes respectively, and $T_{neutral}$ is the IR transmission through the CMS sample under no applied bias. The $T_{neutral}$ is necessary to normalize sample transmission, IR spectrometer throughput, and IR source variations over time.

3.6.7 Pseudo free-standing tensile tests (FOW)

Thin film tensile tests were performed on the water surface through pseudo-free-standing tensile tester. Details about the tensile stage setup can be referred to previous description.[150] Briefly speaking, the polymer thin films (≈90 nm) were patterned into dog-bone shape by oxygen plasma etching process and floated on top of water before being further unidirectionally pulled at a strain rate of 5 × 10−4 s−1 until the film fractures. At least six independent samples were measured for each conjugated polymer to provide statistically averaged mechanical properties. The elastic modulus was obtained from the slope of the linear fit of the stress–strain curve using the first 0.5% strain (elastic region).

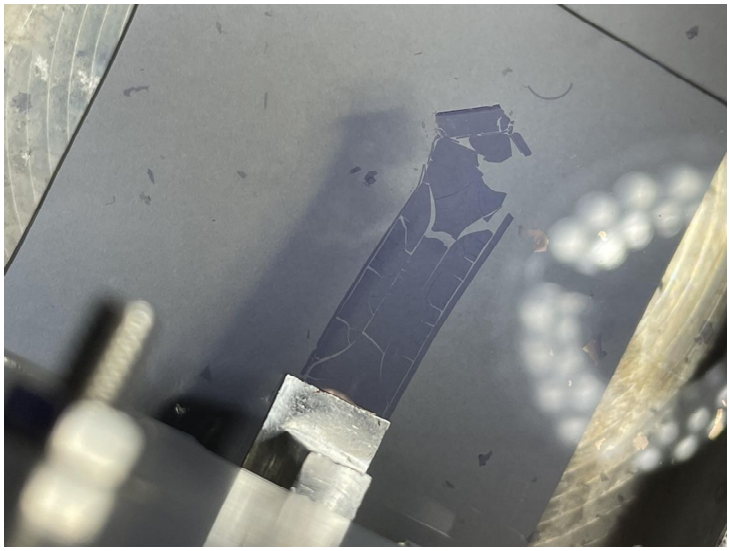

Figure 3.13. $PIDT_{C16}$-TPD_{C1} thin-film fractured before it could be loaded onto the strain stage. This occurred each of the twenty times it was attempted.

3.6.8 Charge transport property measurements

Table 3.4. OFET data is reported for all IDT-copolymers.

Sample	$\mu_{,hole}$ ($cm^2 \cdot V^{-1} \cdot s^{-1}$)	V_T (V)	I_{on}/I_{off}
$PIDT_{C16}$-BT	0.068 ± 0.020	-30	50000
$PIDT_{C20}$-BT	0.023 ± 0.003	-60	10000
$PIDT_{C16}$-TPD_{C1}	0.051 ± 0.030	-57	10000
$PIDT_{C16}$-TPD_{C8}	0.007 ± 0.005	-60	1000
$PIDT_{C16}$-$TPDC_{13B}$	0.006 ± 0.002	-34	1000

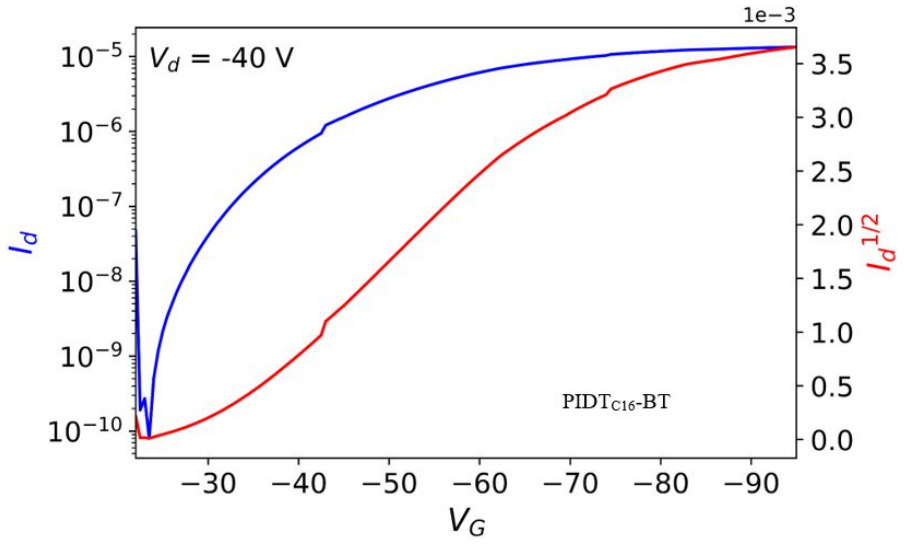

Figure 3.14. Representative OFET curve of $PIDT_{C16}$-BT thin films.

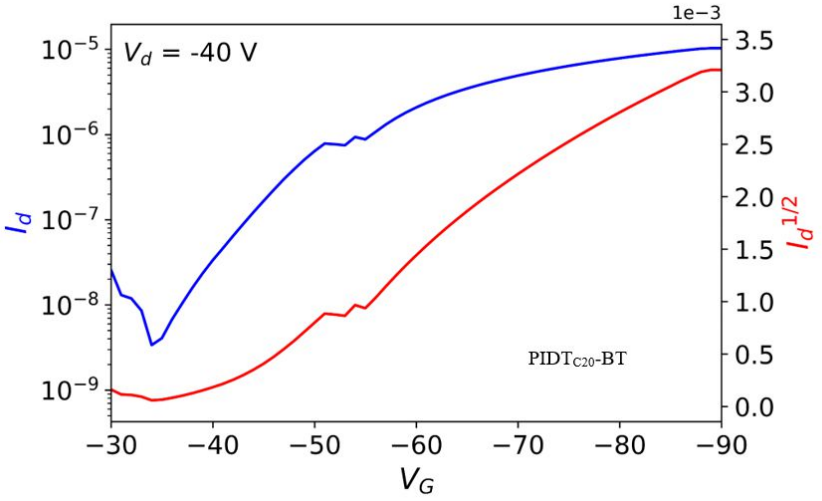

Figure 3.15. Representative OFET curve of PIDT$_{C20}$-BT thin films.

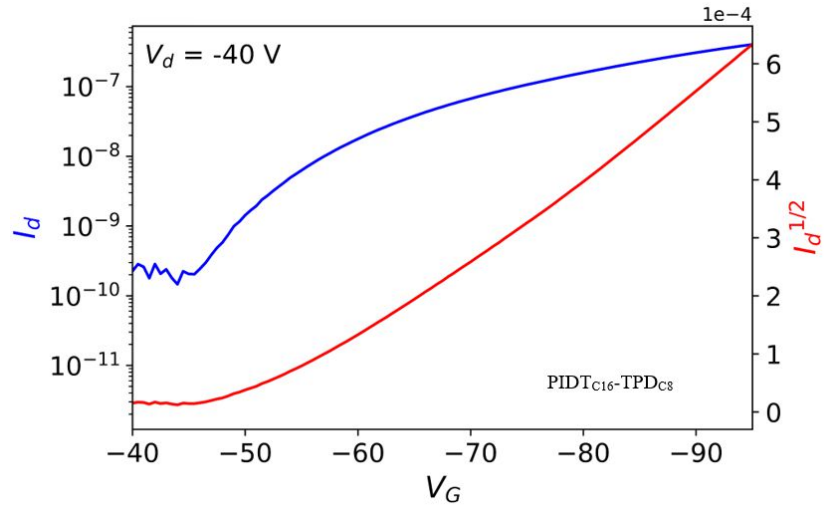

Figure 3.16. Representative OFET curve of PIDT$_{C16}$-TPD$_{C1}$ thin films.

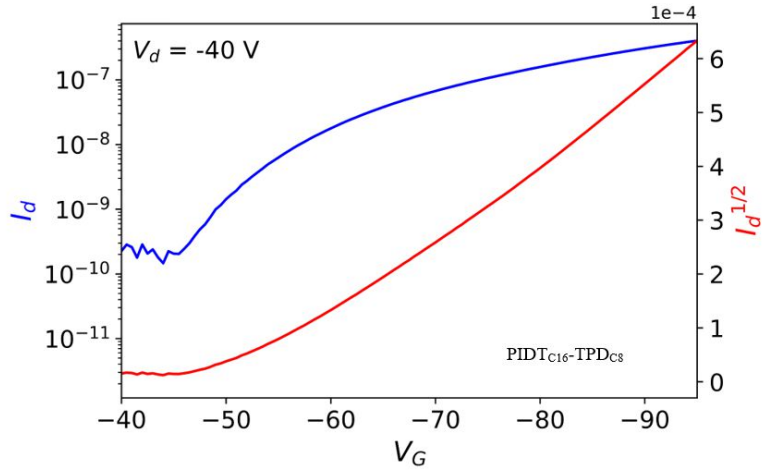

Figure 3.17. Representative OFET curve of PIDT$_{C16}$-TPD$_{C8}$ thin films.

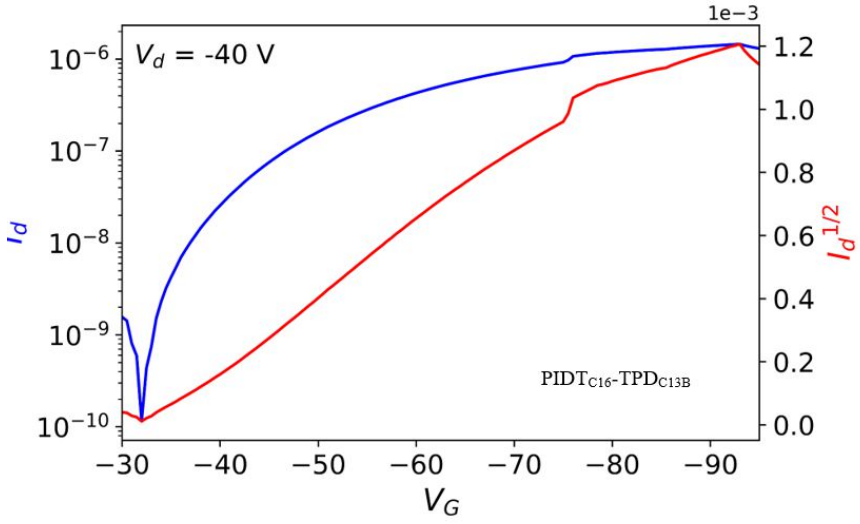

Figure 3.18. Representative OFET curve of PIDT$_{C16}$-TPD$_{C13B}$ thin films**.**

3.6.8 ^{1}H NMR spectroscopy

^{1}H NMR spectra were collected on a 500 MHz Bruker AV500 NMR spectrometer. $CDCl_3$ was used as solvent and the measurements were conducted at room temperature.

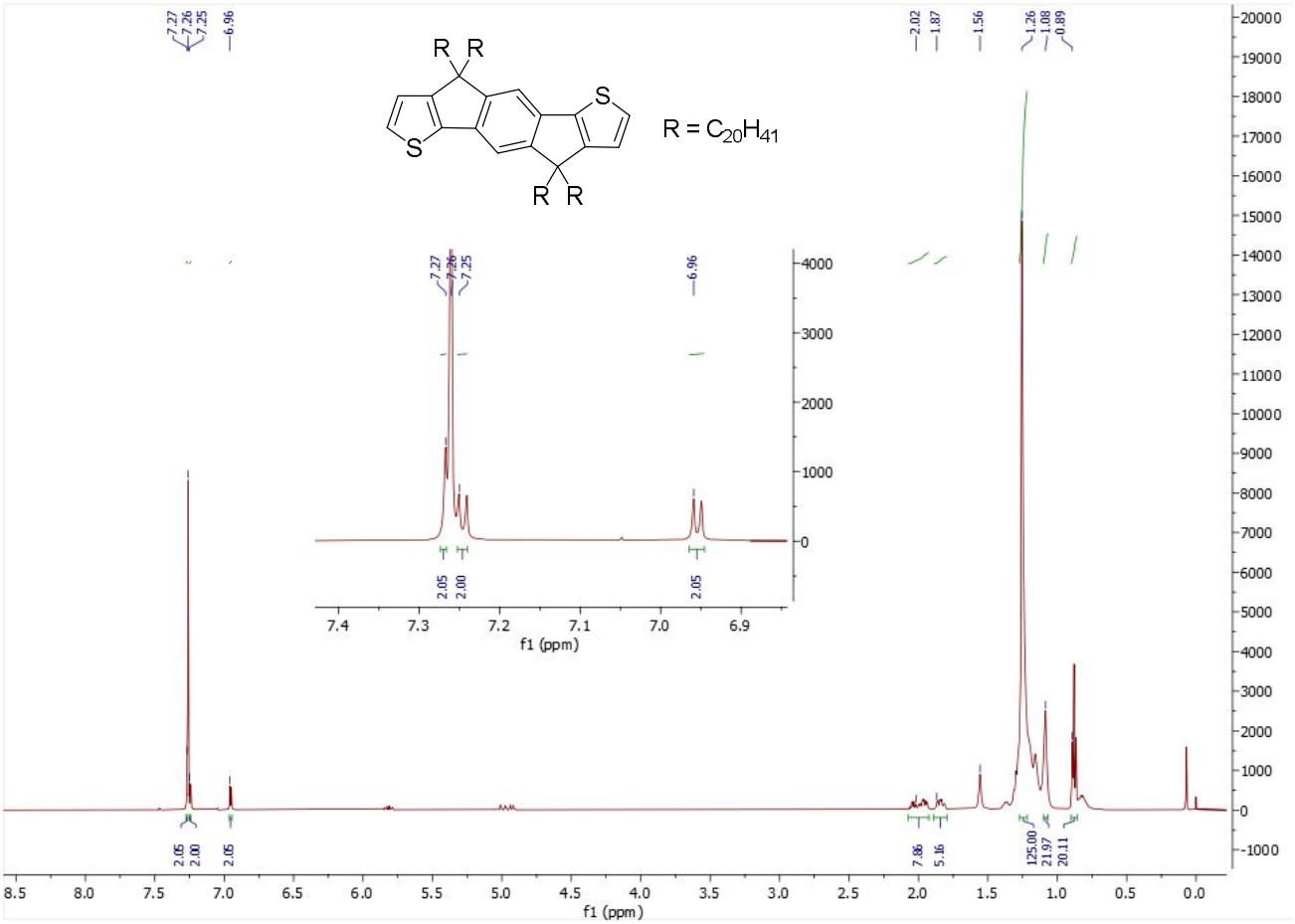

Figure 3.19. ^{1}H NMR spectrum of IDT_{C20}.

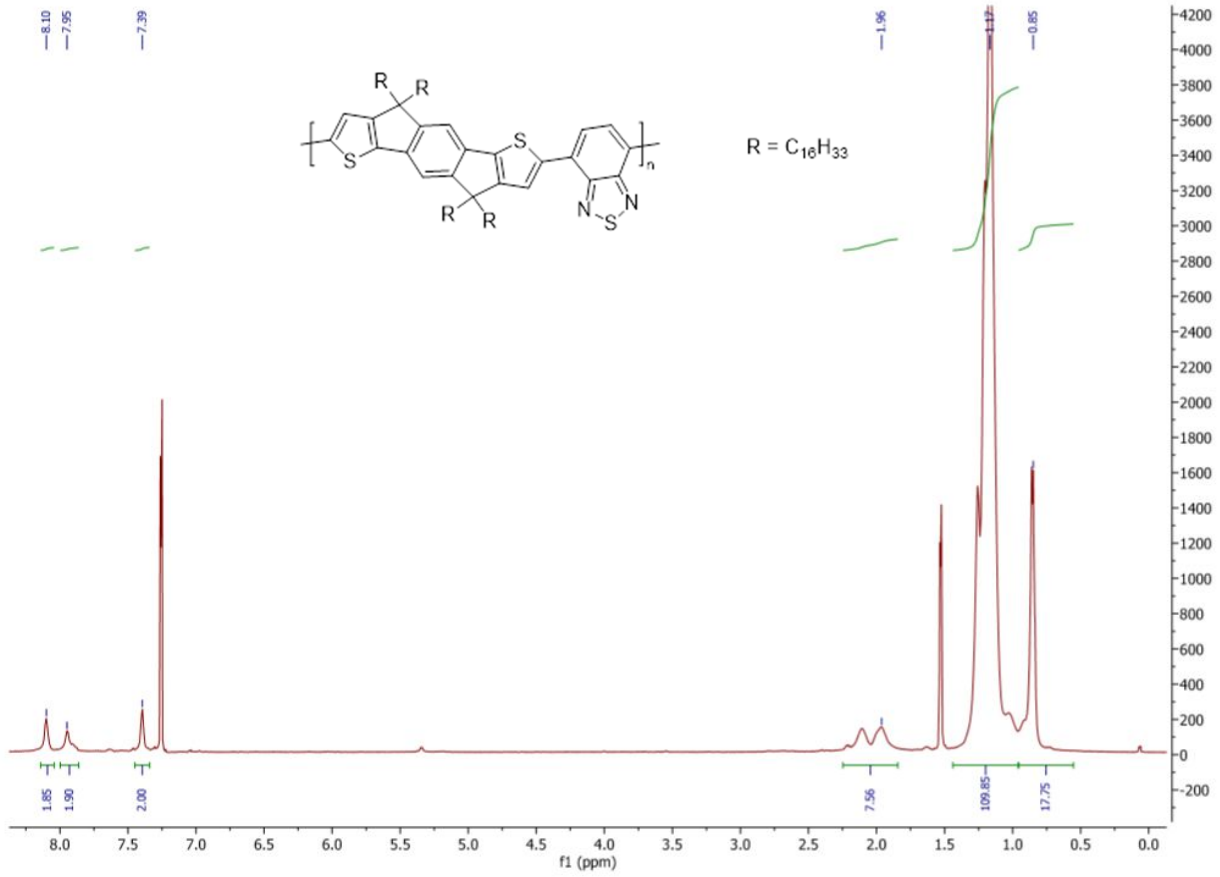

Figure 3.20. ^{1}H NMR of PIDT$_{C16}$-BT.

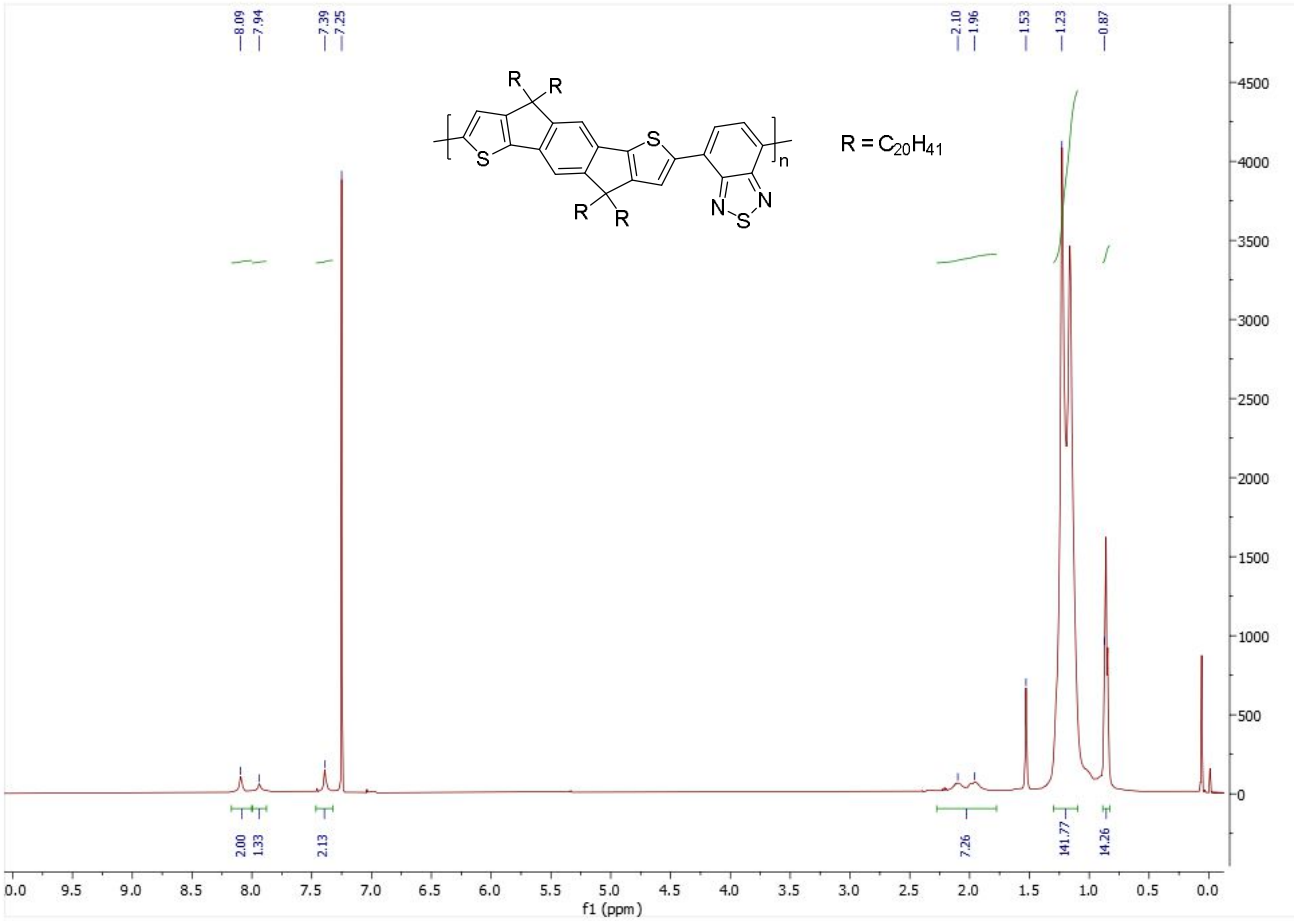

Figure 3.21. ^{1}H HNMR spectra of PIDT$_{C20}$-BT.

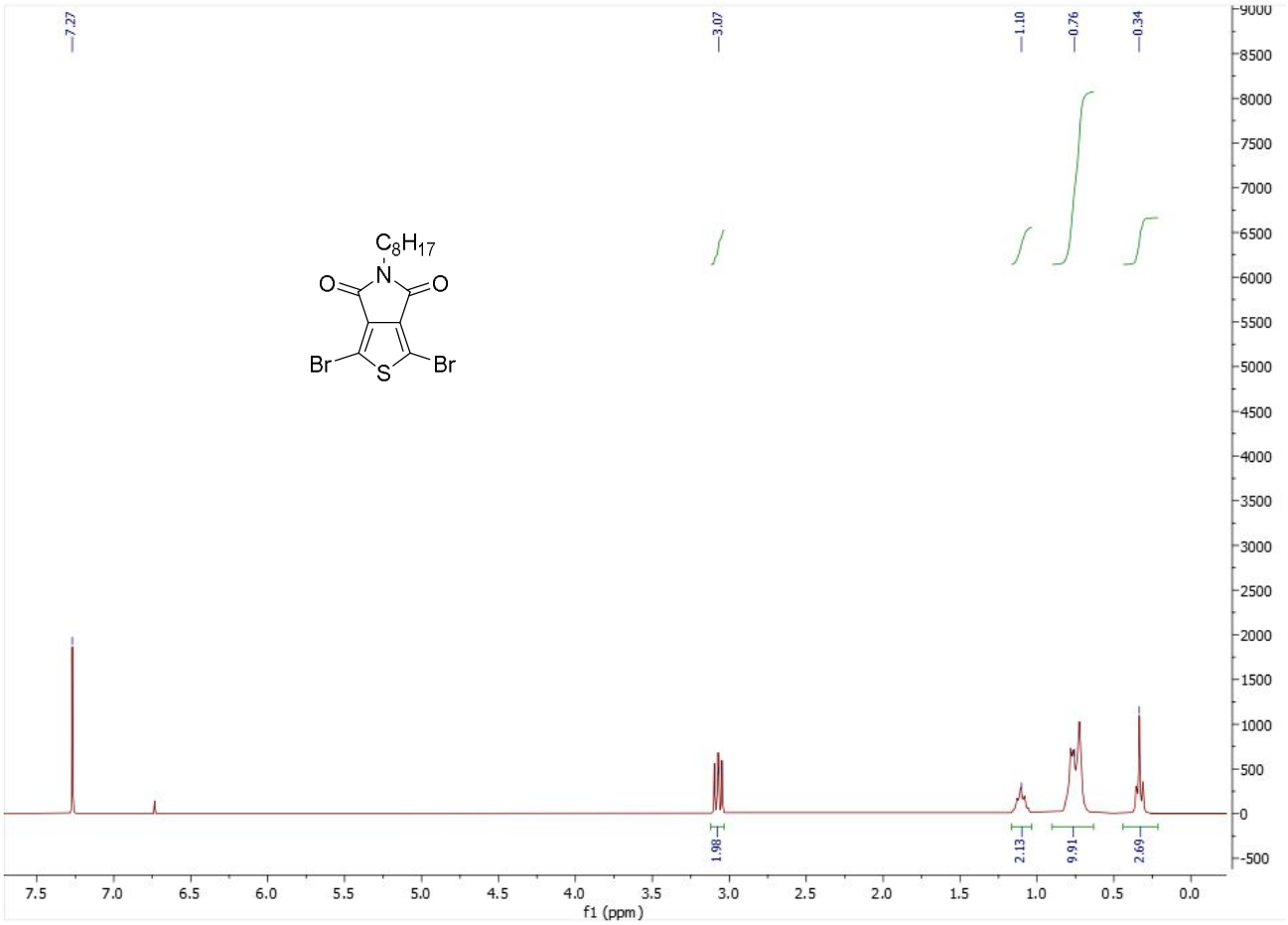

Figure 3.22. ^{1}H NMR spectrum of TPD_{C8}-Br_2

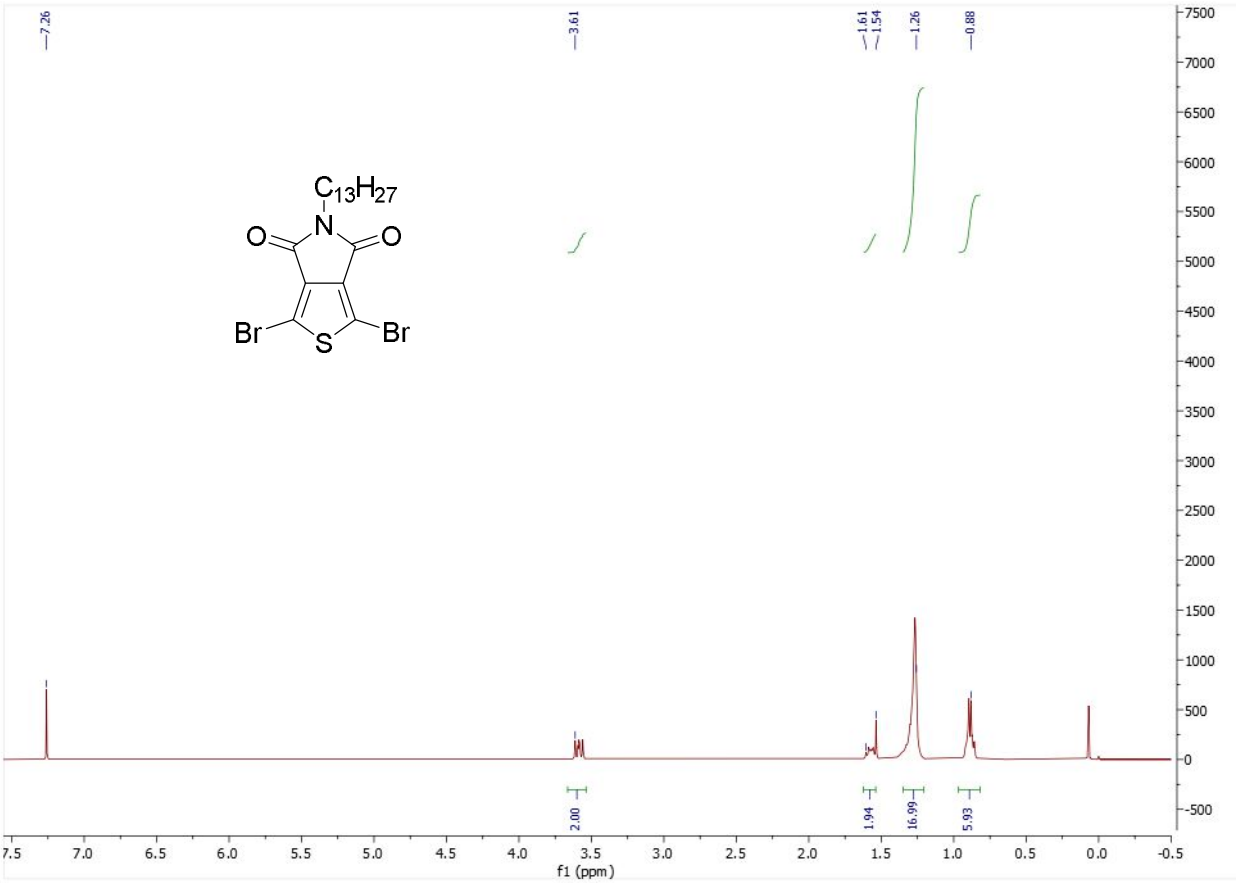

Figure 3.23. ^{1}H NMR spectrum of TPD_{C13B}-Br_2.

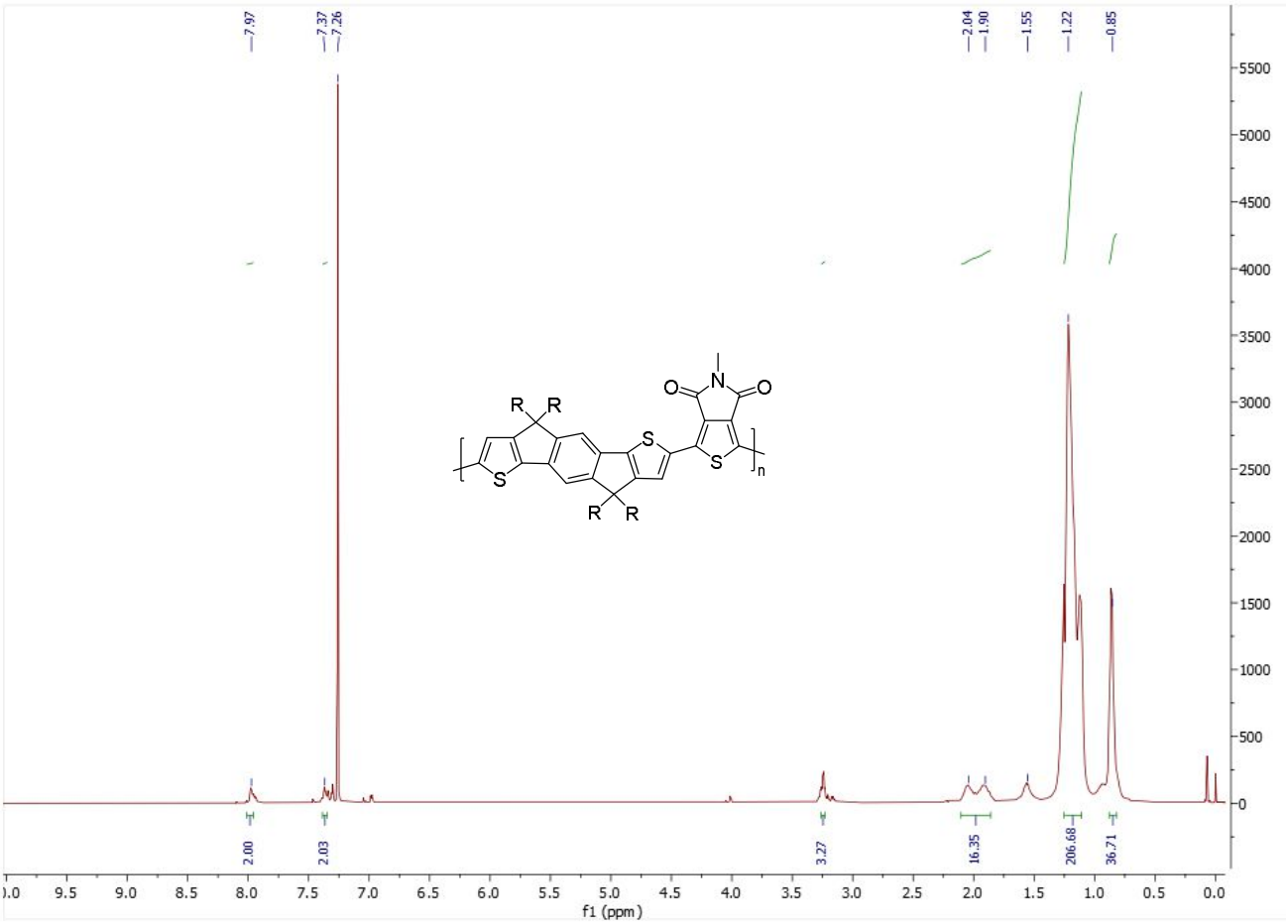

Figure 3.24. ^{1}H NMR spectrum of $PIDT_{C16}$-TPD_{C1}.

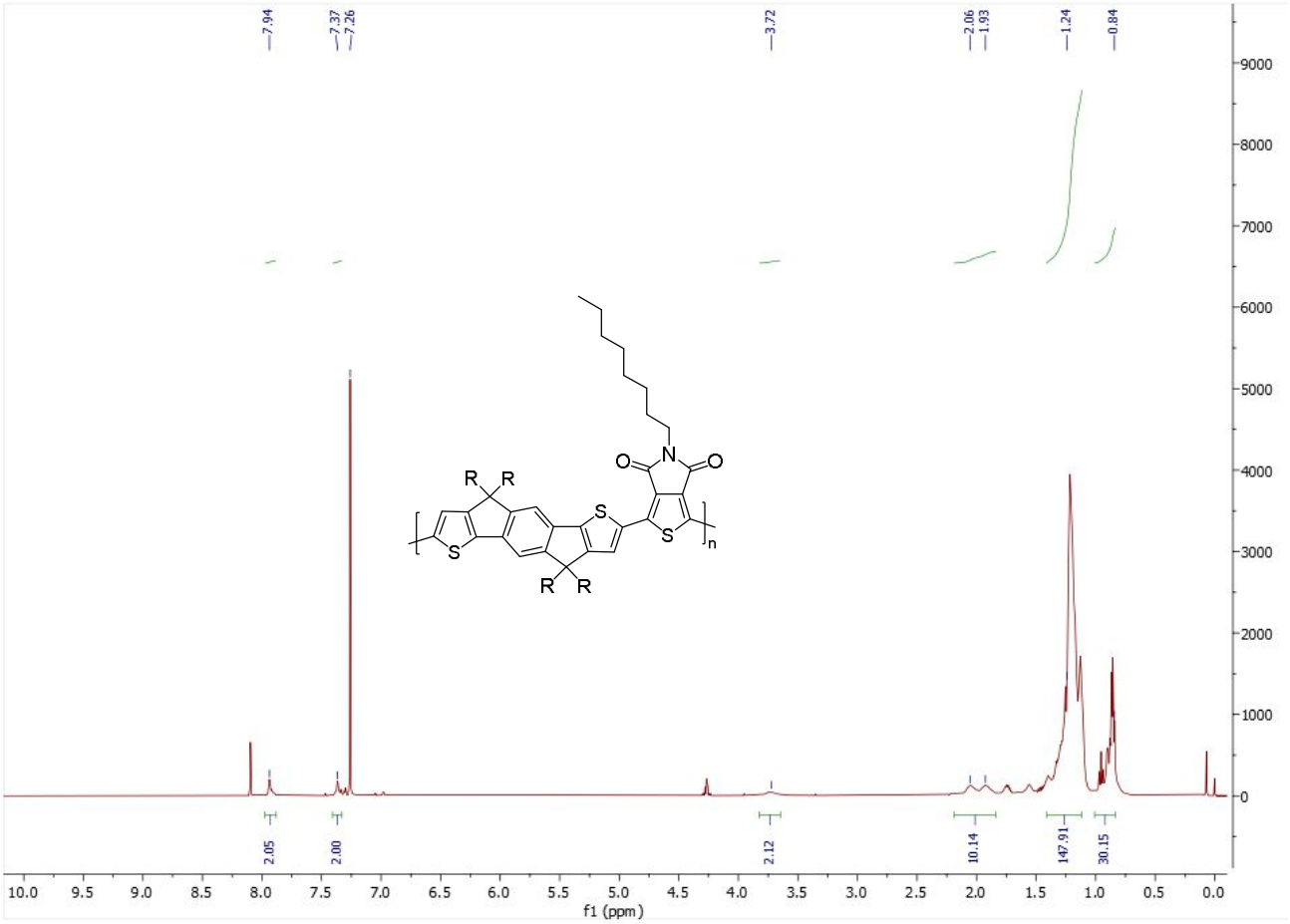

Figure 3.25. ^{1}H NMR spectrum of $PIDT_{C16}$-TPD_{C8}.

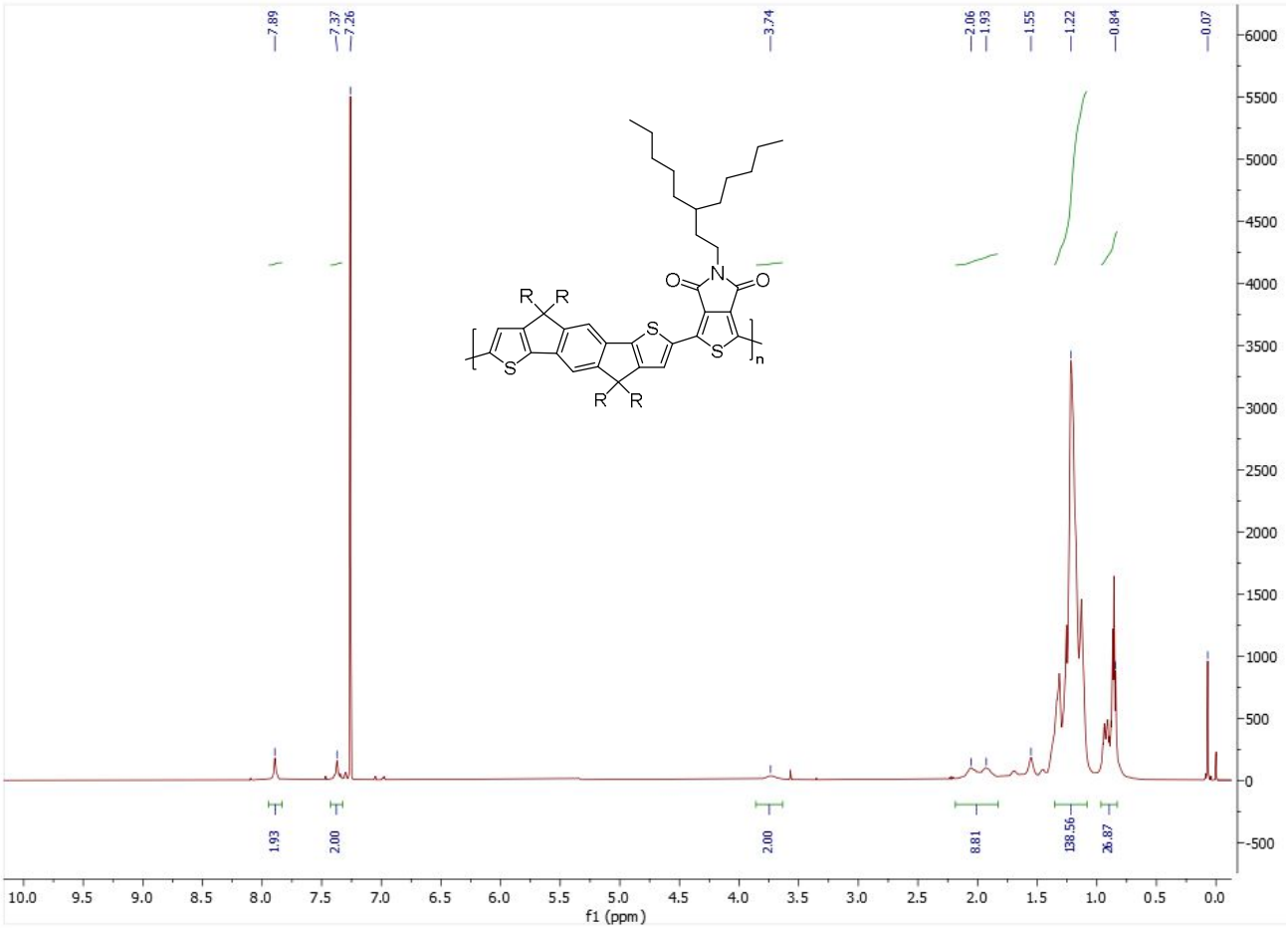

Figure 3.26. ^{1}H NMR spectrum of PIDT$_{C16}$-TPD$_{C13B}$.

Chapter 4. Outlook and recommendations for future work

4.1 Outlook

The work described in Chapters 2 and 3 uncovered the specific roles that the alkyl side chains of IDT-copolymers play in determining their mechanical and electronic properties. Increasing the circularity of the side chain extension profile and disrupting interdigitation of alkyl side-chains are promising ways to increase the elongation at break of IDT-copolymer thin films. Given the results of the investigation into side chain substitution of TPD-containing systems, alkylation of every monomer unit within the backbone is an effective method of decreasing the elastic modulus. Unfortunately, development of intrinsically stretchable CPs with low elastic moduli, high elongation at break, and high charge mobility remains elusive. This is because of the relationship between M_n, backbone entanglement, elastic modulus and hole mobility. Increasing the M_n leads to increases in hole mobility due to a reduced number of inter-molecular charge transport events required to complete the circuit between source and drain electrodes. Increasing M_n can lead to significant increases in elongation at break due to the formation of entanglements. However, entanglements are a form of stress-bearing interactions between backbones, which increases the elastic modulus of materials. Therefore, while it is a method to increase elongation at break, it is unlikely to yield materials of increased stretchability that are also low modulus. The work described in chapter 3 indicates that IDT-copolymers with low modulus and an ability to plastically deform can be achieved, but at with cost of decreased $\mu_{,hole}$. A proposed strategy to guide future study is to synthesize CPs with increased side chain attachment density and M_n low enough to be below M_e, but of sufficient length to promote long range intra-molecular charge transport. These materials should be of ultra-high persistence length so they can have long contour lengths while remaining unentangled to facilitate charge transport. Finally, these

materials would ideally have positions along the backbone that facilitate necessary intermolecular charge transfers, in spite of the high alkyl-side chain density, to a greater degree than the IDT-monomer. This stands as a potential method to develop intrinsically stretchable CPs with low elastic moduli, an ability to deform plastically, while retaining the $\mu_{,hole}$ of their less densely alkylated parent polymers.

4.2 Side chain substitution of TIF- and TBIDT-copolymers

Dithiopheneindenofluorene (TIF) and thienobenzo[b]indacenodithiophene (TBIDT) are structural analogs of IDT derived from π-extension of the aromatic core.[25,91,135] PTIF$_{C16}$-BT and PBTIDT$_{C16}$-BT copolymers have achieved respectable hole mobilities of 3.0 and 0.9 respectively.[91,135] Given the longer size of the fused aromatic core and the colinear arrangement of their monomer-monomer bonds, these materials are expected to have larger L_p*'s* than BT- and TPD-containing IDT-copolymers. Incorporation of the TIF and TBIDT monomer into a CP could potentially allow for longer polymer systems that remain unentangled, while increasing the length charges can be transported on an individual chain before requiring intermolecular charge transfer. Synthesis of PTIF$_{C16}$-BT, PTIF$_{C16}$-TPD$_{C13B}$, PBTIDT$_{C16}$-BT and PBTIDT$_{C16}$-TPD$_{C13B}$ would potentially satisfy the design criteria discussed in section 4.1 and allow for useful comparison to the materials studied in chapter 3. Like PIDT$_{C16}$-TPD$_{C13B}$, the PTIF$_{C16}$-TPD$_{C13B}$ and PBTIDT$_{C16}$-TPD$_{C13B}$ would contain a large side chain on every monomer repeat unit, but there is more un-alkylated, albeit fused, aromatic backbone between the TPD-unit and the sp^3 bridgehead carbon. We could thereby differentiate the impact of increasing the distance between side chain attachment points, without changing the attachment density (every repeat unit would remain alkylated). TPD$_{C13B}$-containing TIF- and TBIDT-copolymers would allow for the assessment of new structure property relationships relating to side chain substitution and aromatic core extension.

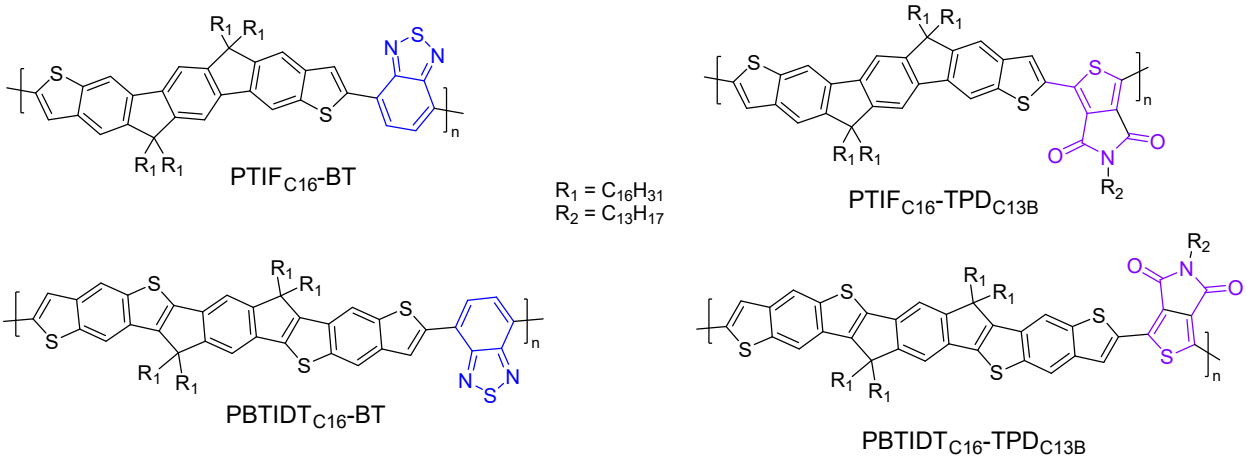

Figure 4.1. BT-containing and TPD$_{C13B}$-containing TIF- and BTIDT-copolymer targets.

Appendix A: References

(1) Pron, A.; Rannou, P. Processible Conjugated Polymers: From Organic Semiconductors to Organic Metals and Superconductors. *Progress in Polymer Science* **2002**, *27* (1), 135–190. https://doi.org/10.1016/S0079-6700(01)00043-0.

(2) Lu, H.; Li, X.; Lei, Q. Conjugated Conductive Polymer Materials and Its Applications: A Mini-Review. *Frontiers in Chemistry* **2021**, *9,* 732132.

(3) Etemad, S.; Heeger, A. J. Polyacetylene, (CH)x: The Prototype Conducting Polymer. *Annual Review of Physical Chemistry* **1982**, *33* (1), 443–469. https://doi.org/10.1146/annurev.pc.33.100182.002303.

(4) van Mullekom, H. A. M.; Vekemans, J. A. J. M.; Havinga, E. E.; Meijer, E. W. Developments in the Chemistry and Band Gap Engineering of Donor–Acceptor Substituted Conjugated Polymers. *Materials Science and Engineering: R: Reports* **2001**, *32* (1), 1–40. https://doi.org/10.1016/S0927-796X(00)00029-2.

(5) Scharber, M. C.; Sariciftci, N. S. Low Band Gap Conjugated Semiconducting Polymers. *Advanced Materials Technologies* **2021**, *6* (4), 2000857. https://doi.org/10.1002/admt.202000857.

(6) Moliton, A.; Hiorns, R. C. Review of Electronic and Optical Properties of Semiconducting π-Conjugated Polymers: Applications in Optoelectronics. *Polymer International* **2004**, *53* (10), 1397–1412. https://doi.org/10.1002/pi.1587.

(7) Wang, X.; Shapiro, B.; Smela, E. Development of a Model for Charge Transport in Conjugated Polymers. *J. Phys. Chem. C* **2009**, *113* (1), 382–401. https://doi.org/10.1021/jp802941m.

(8) Wu, Y.; Zhao, Y.; Liu, Y. Toward Efficient Charge Transport of Polymer-Based Organic Field-Effect Transistors: Molecular Design, Processing, and Functional Utilization. *Acc. Mater. Res.* **2021**, *2* (11), 1047–1058. https://doi.org/10.1021/accountsmr.1c00149.

(9) Chang, M.; Lim, G. T.; Park, B.; Reichmanis, E. Control of Molecular Ordering, Alignment, and Charge Transport in Solution-Processed Conjugated Polymer Thin Films. *Polymers* **2017**, *9* (6), 212. https://doi.org/10.3390/polym9060212.

(10) Fratini, S.; Nikolka, M.; Salleo, A.; Schweicher, G.; Sirringhaus, H. Charge Transport in High-Mobility Conjugated Polymers and Molecular Semiconductors. *Nat. Mater.* **2020**, *19* (5), 491–502. https://doi.org/10.1038/s41563-020-0647-2.

(11) Noriega, R.; Rivnay, J.; Vandewal, K.; Koch, F. P. V.; Stingelin, N.; Smith, P.; Toney, M. F.; Salleo, A. A General Relationship between Disorder, Aggregation and Charge Transport in Conjugated Polymers. *Nature Materials* **2013**, *12* (11), 1038–1044. https://doi.org/10.1038/nmat3722.

(12) Lee, J. Physical Modeling of Charge Transport in Conjugated Polymer Field-Effect Transistors. *J. Phys. D: Appl. Phys.* **2021**, *54* (14), 143002. https://doi.org/10.1088/1361-6463/abd271.

(13) Grozema, F. C.; van Duijnen, P. Th.; Berlin, Y. A.; Ratner, M. A.; Siebbeles, L. D. A. Intramolecular Charge Transport along Isolated Chains of Conjugated Polymers: Effect of Torsional Disorder and Polymerization Defects. *J. Phys. Chem. B* **2002**, *106* (32), 7791–7795. https://doi.org/10.1021/jp021114v.

(14) Mollinger, S. A.; Salleo, A.; Spakowitz, A. J. Anomalous Charge Transport in Conjugated Polymers Reveals Underlying Mechanisms of Trapping and Percolation. *ACS Cent. Sci.* **2016**, *2* (12), 910–915. https://doi.org/10.1021/acscentsci.6b00251.

(15) Abbaszadeh, D.; Kunz, A.; Kotadiya, N. B.; Mondal, A.; Andrienko, D.; Michels, J. J.; Wetzelaer, G.-J. A. H.; Blom, P. W. M. Electron Trapping in Conjugated Polymers. *Chem. Mater.* **2019**, *31* (17), 6380–6386. https://doi.org/10.1021/acs.chemmater.9b01211.

(16) Kim, M.; Ryu, S. U.; Park, S. A.; Choi, K.; Kim, T.; Chung, D.; Park, T. Donor–Acceptor-Conjugated Polymer for High-Performance Organic Field-Effect Transistors: A Progress Report. *Advanced Functional Materials* **2020**, *30* (20), 1904545. https://doi.org/10.1002/adfm.201904545.

(17) Graupner, W.; Leditzky, G.; Leising, G.; Scherf, U. Shallow and Deep Traps in Conjugated Polymers of High Intrachain Order. *Phys. Rev. B* **1996**, *54* (11), 7610–7613. https://doi.org/10.1103/PhysRevB.54.7610.

(18) Adamczak, D.; Perinot, A.; Komber, H.; Illy, A.; Hultmark, S.; Passarella, B.; Tan, W. L.; Hutsch, S.; Becker-Koch, D.; Rapley, C.; Scaccabarozzi, A. D.; Heeney, M.; Vaynzof, Y.; Ortmann, F.; McNeill, C. R.; Müller, C.; Caironi, M.; Sommer, M. Influence of Synthetic Pathway, Molecular Weight and Side Chains on Properties of Indacenodithiophene-Benzothiadiazole Copolymers Made by Direct Arylation Polycondensation. *J. Mater. Chem. C* **2021**, *9* (13), 4597–4606. https://doi.org/10.1039/D1TC00043H.

(19) Noriega, R.; Salleo, A.; Spakowitz, A. J. Chain Conformations Dictate Multiscale Charge Transport Phenomena in Disordered Semiconducting Polymers. *Proceedings of the National Academy of Sciences* **2013**, *110* (41), 16315–16320. https://doi.org/10.1073/PNAS.1307158110.

(20) Noriega, R. Efficient Charge Transport in Disordered Conjugated Polymer Microstructures. *Macromolecular Rapid Communications* **2018**, *39* (14), 1800096. https://doi.org/10.1002/marc.201800096.

(21) Pankow, R. M.; Thompson, B. C. The Development of Conjugated Polymers as the Cornerstone of Organic Electronics. *Polymer* **2020**, *207*, 122874. https://doi.org/10.1016/j.polymer.2020.122874.

(22) Mei, J.; Bao, Z. Side Chain Engineering in Solution-Processable Conjugated Polymers. *Chemistry of Materials* **2014**, *26* (1), 604–615. https://doi.org/10.1021/cm4020805.

(23) Gu, X.; Zhou, Y.; Gu, K.; Kurosawa, T.; Guo, Y.; Li, Y.; Lin, H.; Schroeder, B. C.; Yan, H.; Molina-Lopez, F.; Tassone, C. J.; Wang, C.; Mannsfeld, S. C. B.; Yan, H.; Zhao, D.; Toney, M. F.; Bao, Z. Roll-to-Roll Printed Large-Area All-Polymer Solar Cells with 5% Efficiency Based on a Low Crystallinity Conjugated Polymer Blend. *Advanced Energy Materials* **2017**, *7* (14), 1602742. https://doi.org/10.1002/aenm.201602742.

(24) Yang, J.; Zhao, Z.; Wang, S.; Guo, Y.; Liu, Y. Insight into High-Performance Conjugated Polymers for Organic Field-Effect Transistors. *Chem* **2018**, *4* (12), 2748–2785. https://doi.org/10.1016/j.chempr.2018.08.005.

(25) Wadsworth, A.; Chen, H.; Thorley, K. J.; Cendra, C.; Nikolka, M.; Bristow, H.; Moser, M.; Salleo, A.; Anthopoulos, T. D.; Sirringhaus, H.; McCulloch, I. Modification of Indacenodithiophene-Based Polymers and Its Impact on Charge Carrier Mobility in Organic Thin-Film Transistors. *J. Am. Chem. Soc.* **2020**, *142* (2), 652–664. https://doi.org/10.1021/jacs.9b09374.

(26) Mike, J. F.; Lutkenhaus, J. L. Recent Advances in Conjugated Polymer Energy Storage. *Journal of Polymer Science Part B: Polymer Physics* **2013**, *51* (7), 468–480. https://doi.org/10.1002/polb.23256.

(27) Ashizawa, M.; Zheng, Y.; Tran, H.; Bao, Z. Intrinsically Stretchable Conjugated Polymer Semiconductors in Field Effect Transistors. *Progress in Polymer Science* **2020**, *100*, 101181. https://doi.org/10.1016/j.progpolymsci.2019.101181.

(28) Facchetti, A. Semiconductors for Organic Transistors. *Materials Today* **2007**, *10* (3), 28–37. https://doi.org/10.1016/S1369-7021(07)70017-2.

(29) Ghibaudo, G.; Rafhay, Q. Electron and Hole Mobility in Semiconductor Devices. In *Wiley Encyclopedia of Electrical and Electronics Engineering*; John Wiley & Sons, Ltd, 2014; pp 1–13. https://doi.org/10.1002/047134608X.W3148.pub2.

(30) Zaumseil, J. Semiconducting Single-Walled Carbon Nanotubes or Very Rigid Conjugated Polymers: A Comparison. *Advanced Electronic Materials* **2019**, *5* (2), 1800514. https://doi.org/10.1002/aelm.201800514.

(31) Sui, Y.; Deng, Y.; Du, T.; Shi, Y.; Geng, Y. Design Strategies of N-Type Conjugated Polymers for Organic Thin-Film Transistors. *Mater. Chem. Front.* **2019**, *3* (10), 1932–1951. https://doi.org/10.1039/C9QM00382G.

(32) Horowitz, G. Organic Field-Effect Transistors. *Advanced Materials* **1998**, *10* (5), 365–377. https://doi.org/10.1002/(SICI)1521-4095(199803)10:5<365::AID-ADMA365>3.0.CO;2-U.

(33) Bae, S.-H.; Zhao, H.; Hsieh, Y.-T.; Zuo, L.; De Marco, N.; Rim, Y. S.; Li, G.; Yang, Y. Printable Solar Cells from Advanced Solution-Processible Materials. *Chem* **2016**, *1* (2), 197–219. https://doi.org/10.1016/j.chempr.2016.07.010.

(34) Higashihara, T. Strategic Design and Synthesis of π-Conjugated Polymers Suitable as Intrinsically Stretchable Semiconducting Materials. *Polym J* **2021**, *53* (10), 1061–1071. https://doi.org/10.1038/s41428-021-00510-1.

(35) Jansen, F.; Machonkin, M. A.; Palmieri, N.; Kuhman, D. Thermomechanical Properties of Amorphous Silicon and Nonstoichiometric Silicon Oxide Films. *Journal of Applied Physics* **1987**, *62* (12), 4732–4736. https://doi.org/10.1063/1.339026.

(36) Wang, G.-J. N.; Gasperini, A.; Bao, Z. Stretchable Polymer Semiconductors for Plastic Electronics. *Advanced Electronic Materials* **2018**, *4* (2), 1700429. https://doi.org/10.1002/aelm.201700429.

(37) Wang, M.; Baek, P.; Akbarinejad, A.; Barker, D.; Travas-Sejdic, J. Conjugated Polymers and Composites for Stretchable Organic Electronics. *J. Mater. Chem. C* **2019**, *7* (19), 5534–5552. https://doi.org/10.1039/C9TC00709A.

(38) Zheng, Y.; Yu, Z.; Zhang, S.; Kong, X.; Michaels, W.; Wang, W.; Chen, G.; Liu, D.; Lai, J.-C.; Prine, N.; Zhang, W.; Nikzad, S.; Cooper, C. B.; Zhong, D.; Mun, J.; Zhang, Z.; Kang, J.; Tok, J. B.-H.; McCulloch, I.; Qin, J.; Gu, X.; Bao, Z. A Molecular Design Approach towards Elastic and Multifunctional Polymer Electronics. *Nat Commun* **2021**, *12* (1), 1–11. https://doi.org/10.1038/s41467-021-25719-9.

(39) Kim, H.-J.; Sim, K.; Thukral, A.; Yu, C. Rubbery Electronics and Sensors from Intrinsically Stretchable Elastomeric Composites of Semiconductors and Conductors. *Science Advances 3* (9), e1701114. https://doi.org/10.1126/sciadv.1701114.

(40) Dai, Y.; Hu, H.; Wang, M.; Xu, J.; Wang, S. Stretchable Transistors and Functional Circuits for Human-Integrated Electronics. *Nat Electron* **2021**, *4* (1), 17–29. https://doi.org/10.1038/s41928-020-00513-5.

(41) Rogers, J. A.; Someya, T.; Huang, Y. Materials and Mechanics for Stretchable Electronics. *Science* **2010**, *327* (5973), 1603–1607. https://doi.org/10.1126/science.1182383.

(42) Sim, K.; Rao, Z.; Ershad, F.; Yu, C. Rubbery Electronics Fully Made of Stretchable Elastomeric Electronic Materials. *Advanced Materials* **2020**, *32* (15), 1902417. https://doi.org/10.1002/adma.201902417.

(43) Qiu, Y.; Zhang, B.; Yang, J.; Gao, H.; Li, S.; Wang, L.; Wu, P.; Su, Y.; Zhao, Y.; Feng, J.; Jiang, L.; Wu, Y. Wafer-Scale Integration of Stretchable Semiconducting Polymer Microstructures via Capillary Gradient. *Nat Commun* **2021**, *12* (1), 7038. https://doi.org/10.1038/s41467-021-27370-w.

(44) Zheng, Y.; Zhang, S.; Tok, J. B.-H.; Bao, Z. Molecular Design of Stretchable Polymer Semiconductors: Current Progress and Future Directions. *J. Am. Chem. Soc.* **2022**, *144* (11), 4699–4715. https://doi.org/10.1021/jacs.2c00072.

(45) Zhao, B.; Pei, D.; Jiang, Y.; Wang, Z.; An, C.; Deng, Y.; Ma, Z.; Han, Y.; Geng, Y. Simultaneous Enhancement of Stretchability, Strength, and Mobility in Ultrahigh-Molecular-Weight Poly(Indacenodithiophene-Co-Benzothiadiazole). *Macromolecules* **2021**, *54* (21), 9896–9905. https://doi.org/10.1021/acs.macromol.1c01513.

(46) O'Connor, B.; Kline, R. J.; Conrad, B. R.; Richter, L. J.; Gundlach, D.; Toney, M. F.; DeLongchamp, D. M. Anisotropic Structure and Charge Transport in Highly Strain-Aligned Regioregular Poly(3-Hexylthiophene). *Advanced Functional Materials* **2011**, *21* (19), 3697–3705. https://doi.org/10.1002/adfm.201100904.

(47) Root, S. E.; Savagatrup, S.; Pais, C. J.; Arya, G.; Lipomi, D. J. Predicting the Mechanical Properties of Organic Semiconductors Using Coarse-Grained Molecular Dynamics Simulations. *Macromolecules* **2016**, *49* (7), 2886–2894. https://doi.org/10.1021/acs.macromol.6b00204.

(48) Root, S. E.; Savagatrup, S.; Printz, A. D.; Rodriquez, D.; Lipomi, D. J. Mechanical Properties of Organic Semiconductors for Stretchable, Highly Flexible, and Mechanically Robust Electronics. *Chemical Reviews* **2017**, *117* (9), 6467–6499. https://doi.org/10.1021/acs.chemrev.7b00003.

(49) Ding, Z.; Liu, D.; Zhao, K.; Han, Y. Optimizing Morphology to Trade Off Charge Transport and Mechanical Properties of Stretchable Conjugated Polymer Films. *Macromolecules* **2021**, *54* (9), 3907–3926. https://doi.org/10.1021/acs.macromol.1c00268.

(50) Alkhadra, M. A.; Root, S. E.; Hilby, K. M.; Rodriquez, D.; Sugiyama, F.; Lipomi, D. J. Quantifying the Fracture Behavior of Brittle and Ductile Thin Films of Semiconducting Polymers. *Chemistry of Materials* **2017**, *29* (23), 10139–10149. https://doi.org/10.1021/acs.chemmater.7b03922.

(51) Kim, G.-M.; Michler, G. H. Micromechanical Deformation Processes in Toughened and Particle Filled Semicrystalline Polymers: Part 2. Model Representation for Micromechanical Deformation Processes. *Polymer* **1998**, *39* (23), 5699–5703. https://doi.org/10.1016/S0032-3861(98)00169-4.

(52) Rodriquez, D.; Kim, J.-H.; Root, S. E.; Fei, Z.; Boufflet, P.; Heeney, M.; Kim, T.-S.; Lipomi, D. J. Comparison of Methods for Determining the Mechanical Properties of Semiconducting Polymer Films for Stretchable Electronics. *ACS Appl. Mater. Interfaces* **2017**, *9* (10), 8855–8862. https://doi.org/10.1021/acsami.6b16115.

(53) Li, Y.; Tatum, W. K.; Onorato, J. W.; Zhang, Y.; Luscombe, C. K. Low Elastic Modulus and High Charge Mobility of Low-Crystallinity Indacenodithiophene-Based Semiconducting Polymers for Potential Applications in Stretchable Electronics. *Macromolecules* **2018**, *51* (16), 6352–6358. https://doi.org/10.1021/acs.macromol.8b00898.

(54) Zhang, S.; Galuska, L. A.; Gu, X. Water-Assisted Mechanical Testing of Polymeric Thin-Films. *Journal of Polymer Science* **2022**, *60* (7), 1108–1129. https://doi.org/10.1002/pol.20210281.

(55) Chen, A. X.; Kleinschmidt, A. T.; Choudhary, K.; Lipomi, D. J. Beyond Stretchability: Strength, Toughness, and Elastic Range in Semiconducting Polymers. *Chem. Mater.* **2020**, *32* (18), 7582–7601. https://doi.org/10.1021/acs.chemmater.0c03019.

(56) Son, S. Y.; Kim, Y.; Lee, J.; Lee, G.-Y.; Park, W.-T.; Noh, Y.-Y.; Park, C. E.; Park, T. High-Field-Effect Mobility of Low-Crystallinity Conjugated Polymers with Localized Aggregates. *Journal of the American Chemical Society* **2016**, *138* (26), 8096–8103. https://doi.org/10.1021/jacs.6b01046.

(57) Xie, R.; Weisen, A. R.; Lee, Y.; Aplan, M. A.; Fenton, A. M.; Masucci, A. E.; Kempe, F.; Sommer, M.; Pester, C. W.; Colby, R. H.; Gomez, E. D. Glass Transition Temperature from the Chemical Structure of Conjugated Polymers. *Nature Communications* **2020**, *11* (1), 1–8. https://doi.org/10.1038/s41467-020-14656-8.

(58) Bloom, J. W. G.; Wheeler, S. E. Benchmark Torsional Potentials of Building Blocks for Conjugated Materials: Bifuran, Bithiophene, and Biselenophene. *Journal of Chemical Theory and Computation* **2014**, *10* (9), 3647–3655. https://doi.org/10.1021/ct5004725.

(59) Kanimozhi, C.; Naik, M.; Yaacobi-Gross, N.; Burnett, E. K.; Briseno, A. L.; Anthopoulos, T. D.; Patil, S. Controlling Conformations of Diketopyrrolopyrrole-Based Conjugated Polymers: Role of Torsional Angle. *The Journal of Physical Chemistry C* **2014**, *118* (22), 11536–11544. https://doi.org/10.1021/jp501526h.

(60) Steyrleuthner, R.; Di Pietro, R.; Collins, B. A.; Polzer, F.; Himmelberger, S.; Schubert, M.; Chen, Z.; Zhang, S.; Salleo, A.; Ade, H.; Facchetti, A.; Neher, D. The Role of Regioregularity, Crystallinity, and Chain Orientation on Electron Transport in a High-Mobility n-Type Copolymer. *Journal of the American Chemical Society* **2014**, *136* (11), 4245–4256. https://doi.org/10.1021/ja4118736.

(61) Onorato, J.; Pakhnyuk, V.; Luscombe, C. K. Structure and Design of Polymers for Durable, Stretchable Organic Electronics. *Polym J* **2017**, *49* (1), 41–60. https://doi.org/10.1038/pj.2016.76.

(62) Lei, T.; Wang, J.-Y.; Pei, J. Design, Synthesis, and Structure–Property Relationships of Isoindigo-Based Conjugated Polymers. *Acc. Chem. Res.* **2014**, *47* (4), 1117–1126. https://doi.org/10.1021/ar400254j.

(63) Raithel, D.; Simine, L.; Pickel, S.; Schötz, K.; Panzer, F.; Baderschneider, S.; Schiefer, D.; Lohwasser, R.; Köhler, J.; Thelakkat, M.; Sommer, M.; Köhler, A.; Rossky, P. J.; Hildner, R. Direct Observation of Backbone Planarization via Side-Chain Alignment in Single Bulky-Substituted Polythiophenes. *Proceedings of the National Academy of Sciences* **2018**, *115* (11), 2699–2704. https://doi.org/10.1073/pnas.1719303115.

(64) Zhang, T.; Yuan, Y.; Cui, X.; Yin, H.; Gu, J.; Huang, H.; Shu, J. Impact of Side-Chain Length on the Phase Structures of P3ATs and P3AT:PCBM Films as Revealed by SSNMR and FTIR. *Journal of Polymer Science Part B: Polymer Physics* **2018**, *56* (9), 751–761. https://doi.org/10.1002/polb.24587.

(65) Joshi, S.; Pingel, P.; Grigorian, S.; Panzner, T.; Pietsch, U.; Neher, D.; Forster, M.; Scherf, U. Bimodal Temperature Behavior of Structure and Mobility in High Molecular Weight P3HT Thin Films. *Macromolecules* **2009**, *42* (13), 4651–4660. https://doi.org/10.1021/ma900021w.

(66) Chua, M. H.; Zhu, Q.; Tang, T.; Shah, K. W.; Xu, J. Diversity of Electron Acceptor Groups in Donor–Acceptor Type Electrochromic Conjugated Polymers. *Solar Energy Materials and Solar Cells* **2019**, *197*, 32–75. https://doi.org/10.1016/j.solmat.2019.04.002.

(67) Li, Y. Molecular Design of Photovoltaic Materials for Polymer Solar Cells: Toward Suitable Electronic Energy Levels and Broad Absorption. *Acc. Chem. Res.* **2012**, *45* (5), 723–733. https://doi.org/10.1021/ar2002446.

(68) Zhang, Z.; Wang, J. Structures and Properties of Conjugated Donor–Acceptor Copolymers for Solar Cell Applications. *Journal of Materials Chemistry* **2012**, *22* (10), 4178–4178. https://doi.org/10.1039/c2jm14951f.

(69) McDearmon, B.; Lim, E.; Lee, I.-H.; Kozycz, L. M.; O'Hara, K.; Robledo, P. I.; Venkatesan, N. R.; Chabinyc, M. L.; Hawker, C. J. Effects of Side-Chain Topology on Aggregation of Conjugated Polymers. *Macromolecules* **2018**, *51* (7), 2580–2590. https://doi.org/10.1021/acs.macromol.8b00176.

(70) Kline, R. J.; DeLongchamp, D. M.; Fischer, D. A.; Lin, E. K.; Richter, L. J.; Chabinyc, M. L.; Toney, M. F.; Heeney, M.; McCulloch, I. Critical Role of Side-Chain Attachment Density on the Order and Device Performance of Polythiophenes. *Macromolecules* **2007**, *40* (22), 7960–7965. https://doi.org/10.1021/ma0709001.

(71) A. Finn, P.; E. Jacobs, I.; Armitage, J.; Wu, R.; D. Paulsen, B.; Freeley, M.; Palma, M.; Rivnay, J.; Sirringhaus, H.; B. Nielsen, C. Effect of Polar Side Chains on Neutral and P-Doped Polythiophene. *Journal of Materials Chemistry C* **2020**, *8* (45), 16216–16223. https://doi.org/10.1039/D0TC04290K.

(72) Vezie, M. S.; Few, S.; Meager, I.; Pieridou, G.; Dörling, B.; Ashraf, R. S.; Goñi, A. R.; Bronstein, H.; McCulloch, I.; Hayes, S. C.; Campoy-Quiles, M.; Nelson, J. Exploring the Origin of High Optical Absorption in Conjugated Polymers. *Nature Materials* **2016**, *15* (7), 746–753. https://doi.org/10.1038/nmat4645.

(73) Danielsen, S. P. O.; Bridges, C. R.; Segalman, R. A. Chain Stiffness of Donor–Acceptor Conjugated Polymers in Solution. *Macromolecules* **2022**, *55* (2), 437–449. https://doi.org/10.1021/acs.macromol.1c02229.

(74) Zhao, K.; Khan, H. U.; Li, R.; Su, Y.; Amassian, A. Entanglement of Conjugated Polymer Chains Influences Molecular Self-Assembly and Carrier Transport. *Advanced Functional Materials* **2013**, *23* (48), 6024–6035. https://doi.org/10.1002/adfm.201301007.

(75) Jackson, N. E.; Savoie, B. M.; Kohlstedt, K. L.; Olvera de la Cruz, M.; Schatz, G. C.; Chen, L. X.; Ratner, M. A. Controlling Conformations of Conjugated Polymers and Small Molecules: The Role of Nonbonding Interactions. *J. Am. Chem. Soc.* **2013**, *135* (28), 10475–10483. https://doi.org/10.1021/ja403667s.

(76) DuBay, K. H.; Hall, M. L.; Hughes, T. F.; Wu, C.; Reichman, D. R.; Friesner, R. A. Accurate Force Field Development for Modeling Conjugated Polymers. *J. Chem. Theory Comput.* **2012**, *8* (11), 4556–4569. https://doi.org/10.1021/ct300175w.

(77) Yan, X.; Xiong, M.; Deng, X.-Y.; Liu, K.-K.; Li, J.-T.; Wang, X.-Q.; Zhang, S.; Prine, N.; Zhang, Z.; Huang, W.; Wang, Y.; Wang, J.-Y.; Gu, X.; So, S. K.; Zhu, J.; Lei, T. Approaching Disorder-Tolerant Semiconducting Polymers. *Nat Commun* **2021**, *12* (1), 5723. https://doi.org/10.1038/s41467-021-26043-y.

(78) Ma, Y.; Chen, S.-C.; Wang, Z.; Ma, W.; Wang, J.; Yin, Z.; Tang, C.; Cai, D.; Zheng, Q. Indacenodithiophene-Based Wide Bandgap Copolymers for High Performance Single-Junction and Tandem Polymer Solar Cells. *Nano Energy* **2017**, *33*, 313–324. https://doi.org/10.1016/j.nanoen.2017.01.050.

(79) Xie, R.; Colby, R. H.; Gomez, E. D. Connecting the Mechanical and Conductive Properties of Conjugated Polymers. *Advanced Electronic Materials* **2018**, *4* (10), 1700356–1700356. https://doi.org/10.1002/aelm.201700356.

(80) Choudhary, K.; Chen, A. X.; Pitch, G. M.; Runser, R.; Urbina, A.; Dunn, T. J.; Kodur, M.; Kleinschmidt, A. T.; Wang, B. G.; Bunch, J. A.; Fenning, D. P.; Ayzner, A. L.; Lipomi, D. J.

Comparison of the Mechanical Properties of a Conjugated Polymer Deposited Using Spin Coating, Interfacial Spreading, Solution Shearing, and Spray Coating. *ACS Appl. Mater. Interfaces* **2021**, *13* (43), 51436–51446. https://doi.org/10.1021/acsami.1c13043.

(81) Xu, Z.; Park, K. S.; Diao, Y. What Is the Assembly Pathway of a Conjugated Polymer From Solution to Thin Films? *Frontiers in Chemistry* **2020**, *8,* 583521.

(82) McCulloch, B.; Ho, V.; Hoarfrost, M.; Stanley, C.; Do, C.; Heller, W. T.; Segalman, R. A. Polymer Chain Shape of Poly(3-Alkylthiophenes) in Solution Using Small-Angle Neutron Scattering. *Macromolecules* **2013**, *46* (5), 1899–1907. https://doi.org/10.1021/ma302463d.

(83) Lan, Y.-K.; Huang, C.-I. Charge Mobility and Transport Behavior in the Ordered and Disordered States of the Regioregular Poly(3-Hexylthiophene). *J. Phys. Chem. B* **2009**, *113* (44), 14555–14564. https://doi.org/10.1021/jp904841j.

(84) Gu, K.; Snyder, C. R.; Onorato, J.; Luscombe, C. K.; Bosse, A. W.; Loo, Y.-L. Assessing the Huang–Brown Description of Tie Chains for Charge Transport in Conjugated Polymers. *ACS Macro Letters* **2018**, *7* (11), 1333–1338. https://doi.org/10.1021/acsmacrolett.8b00626.

(85) Zhang, X.; Bronstein, H.; Kronemeijer, A. J.; Smith, J.; Kim, Y.; Kline, R. J.; Richter, L. J.; Anthopoulos, T. D.; Sirringhaus, H.; Song, K.; Heeney, M.; Zhang, W.; McCulloch, I.; DeLongchamp, D. M. Molecular Origin of High Field-Effect Mobility in an Indacenodithiophene–Benzothiadiazole Copolymer. *Nature Communications* **2013**, *4* (1), 2238–2238. https://doi.org/10.1038/ncomms3238.

(86) Park, Y. D.; Lee, H. S.; Choi, Y. J.; Kwak, D.; Cho, J. H.; Lee, S.; Cho, K. Solubility-Induced Ordered Polythiophene Precursors for High-Performance Organic Thin-Film Transistors. *Advanced Functional Materials* **2009**, *19* (8), 1200–1206. https://doi.org/10.1002/adfm.200801763.

(87) Wang, P.; Yang, J.; Zhang, Y.; Hu, W.; Dong, H. Near-Amorphous Conjugated Polymers: An Emerging Class of Semiconductors for Flexible Electronics. *ACS Materials Lett.* **2022**, 1112–1123. https://doi.org/10.1021/acsmaterialslett.2c00138.

(88) Printz, A. D.; Zaretski, A. V.; Savagatrup, S.; Chiang, A. S.-C.; Lipomi, D. J. Yield Point of Semiconducting Polymer Films on Stretchable Substrates Determined by Onset of Buckling. *ACS Appl. Mater. Interfaces* **2015**, *7* (41), 23257–23264. https://doi.org/10.1021/acsami.5b08628.

(89) Bronstein, H.; Leem, D. S.; Hamilton, R.; Woebkenberg, P.; King, S.; Zhang, W.; Ashraf, R. S.; Heeney, M.; Anthopoulos, T. D.; Mello, J. de; McCulloch, I. Indacenodithiophene-Co-Benzothiadiazole Copolymers for High Performance Solar Cells or Transistors via Alkyl Chain Optimization. *Macromolecules* **2011**, *44* (17), 6649–6652. https://doi.org/10.1021/ma201158d.

(90) Schroeder, B. C.; Huang, Z.; Ashraf, R. S.; Smith, J.; D'Angelo, P.; Watkins, S. E.; Anthopoulos, T. D.; Durrant, J. R.; McCulloch, I. Silaindacenodithiophene-Based Low Band Gap Polymers – The Effect of Fluorine Substitution on Device Performances and Film Morphologies. *Advanced Functional Materials* **2012**, *22* (8), 1663–1670. https://doi.org/10.1002/adfm.201102941.

(91) Chen, H.; Hurhangee, M.; Nikolka, M.; Zhang, W.; Kirkus, M.; Neophytou, M.; Cryer, S. J.; Harkin, D.; Hayoz, P.; Abdi-Jalebi, M.; McNeill, C. R.; Sirringhaus, H.; McCulloch, I. Dithiopheneindenofluorene (TIF) Semiconducting Polymers with Very High Mobility in Field-Effect Transistors. *Advanced Materials* **2017**, *29* (36), 1702523. https://doi.org/10.1002/adma.201702523.

(92) Ren, H.; Zhang, J.; Tong, Y.; Zhang, J.; Zhao, X.; Cui, N.; Li, Y.; Ye, X.; Tang, Q.; Liu, Y. Synchronously Improved Stretchability and Mobility by Tuning the Molecular Weight for Intrinsically Stretchable Transistors. *J. Mater. Chem. C* **2020**, *8* (44), 15646–15654. https://doi.org/10.1039/D0TC02363A.

(93) Li, Y.; Tatum, W. K.; Onorato, J. W.; Barajas, S. D.; Yang, Y. Y.; Luscombe, C. K. An Indacenodithiophene-Based Semiconducting Polymer with High Ductility for Stretchable Organic Electronics. *Polymer Chemistry* **2017**, *8* (34), 5185–5193. https://doi.org/10.1039/C7PY00435D.

(94) Sirringhaus, H. 25th Anniversary Article: Organic Field-Effect Transistors: The Path Beyond Amorphous Silicon. *Advanced Materials* **2014**, *26* (9), 1319–1335. https://doi.org/10.1002/adma.201304346.

(95) Li, G.; Chang, W.-H.; Yang, Y. Low-Bandgap Conjugated Polymers Enabling Solution-Processable Tandem Solar Cells. *Nat Rev Mater* **2017**, *2* (8), 17043. https://doi.org/10.1038/natrevmats.2017.43.

(96) Woo, C. H.; Piliego, C.; Holcombe, T. W.; Toney, M. F.; Fréchet, J. M. J. A Quantitative Correlation between the Mobility and Crystallinity of Photo-Cross-Linkable P3HT. *Macromolecules* **2012**, *45* (7), 3057–3062. https://doi.org/10.1021/ma202203z.

(97) Bronstein, H.; Leem, D. S.; Hamilton, R.; Woebkenberg, P.; King, S.; Zhang, W.; Ashraf, R. S.; Heeney, M.; Anthopoulos, T. D.; De Mello, J.; Mcculloch, I. Indacenodithiophene-Co-Benzothiadiazole Copolymers for High Performance Solar Cells or Transistors via Alkyl Chain Optimization. **2011**. https://doi.org/10.1021/ma201158d.

(98) Zheng, Y.; Wang, G. N.; Kang, J.; Nikolka, M.; Wu, H.; Tran, H.; Zhang, S.; Yan, H.; Chen, H.; Yuen, P. Y.; Mun, J.; Dauskardt, R. H.; McCulloch, I.; Tok, J. B. -H.; Gu, X.; Bao, Z. An Intrinsically Stretchable High-Performance Polymer Semiconductor with Low Crystallinity. *Advanced Functional Materials* **2019**, 1905340–1905340. https://doi.org/10.1002/adfm.201905340.

(99) Yao, Y.; Dong, H.; Hu, W. Charge Transport in Organic and Polymeric Semiconductors for Flexible and Stretchable Devices. *Advanced Materials* **2016**, *28* (22), 4513–4523. https://doi.org/10.1002/adma.201503007.

(100) Savagatrup, S.; Makaram, A. S.; Burke, D. J.; Lipomi, D. J. Mechanical Properties of Conjugated Polymers and Polymer-Fullerene Composites as a Function of Molecular Structure. *Advanced Functional Materials* **2014**, *24* (8), 1169–1181. https://doi.org/10.1002/adfm.201302646.

(101) Lin, B.; Taylor, P. L. Dynamics of Polymer Chain Pull-Out. *Macromolecules* **1994**, *27* (15), 4212–4219. https://doi.org/10.1021/ma00093a024.

(102) Postema, A. R.; Liou, K.; Wudl, F.; Smith, P. Highly Oriented Low-Modulus Materials from Liquid-Crystalline Polymers: The Ultimate Penalty for Solubilizing Alkyl Side Chains. *Macromolecules* **1990**, *23* (6), 1842–1845. https://doi.org/10.1021/ma00208a048.

(103) Root, S. E.; Jackson, N. E.; Savagatrup, S.; Arya, G.; Lipomi, D. J. Modelling the Morphology and Thermomechanical Behaviour of Low-Bandgap Conjugated Polymers and Bulk Heterojunction Films. *Energy & Environmental Science* **2017**, *10* (2), 558–569. https://doi.org/10.1039/C6EE03456J.

(104) Lu, C.; Lee, W.-Y.; Gu, X.; Xu, J.; Chou, H.-H.; Yan, H.; Chiu, Y.-C.; He, M.; Matthews, J. R.; Niu, W.; Tok, J. B.-H.; Toney, M. F.; Chen, W.-C.; Bao, Z. Effects of Molecular Structure and Packing Order on the Stretchability of Semicrystalline Conjugated Poly(Tetrathienoacene-Diketopyrrolopyrrole) Polymers. *Advanced Electronic Materials* **2017**, *3* (2), 1600311. https://doi.org/10.1002/aelm.201600311.

(105) Sugiyama, F.; Kleinschmidt, A. T.; Kayser, L. V.; Rodriquez, D.; Finn, M.; Alkhadra, M. A.; Wan, J. M.-H.; Ramírez, J.; Chiang, A. S.-C.; Root, S. E.; Savagatrup, S.; Lipomi, D. J. Effects of Flexibility and Branching of Side Chains on the Mechanical Properties of Low-Bandgap Conjugated Polymers. *Polym Chem* **2018**, *9* (33), 4354–4363. https://doi.org/10.1039/C8PY00820E.

(106) Cao, Z.; Galuska, L.; Qian, Z.; Zhang, S.; Huang, L.; Prine, N.; Li, T.; He, Y.; Hong, K.; Gu, X. The Effect of Side-Chain Branch Position on the Thermal Properties of Poly(3-Alkylthiophenes). *Polym. Chem.* **2020**, *11* (2), 517–526. https://doi.org/10.1039/C9PY01026B.

(107) Jin, Y.-J.; Bae, J.-E.; Cho, K.-S.; Lee, W.-E.; Hwang, D.-Y.; Kwak, G. Room Temperature Fluorescent Conjugated Polymer Gums. *Advanced Functional Materials* **2014**, *24* (13), 1928–1937. https://doi.org/10.1002/adfm.201302829.

(108) Balar, N.; O'Connor, B. T. Correlating Crack Onset Strain and Cohesive Fracture Energy in Polymer Semiconductor Films. *Macromolecules* **2017**, *50* (21), 8611–8618. https://doi.org/10.1021/acs.macromol.7b01282.

(109) Eder, T.; Stangl, T.; Gmelch, M.; Remmerssen, K.; Laux, D.; Höger, S.; Lupton, J. M.; Vogelsang, J. Switching between H- and J-Type Electronic Coupling in Single Conjugated Polymer Aggregates. *Nat Commun* **2017**, *8* (1), 1641. https://doi.org/10.1038/s41467-017-01773-0.

(110) Wang, S.; Fabiano, S.; Himmelberger, S.; Puzinas, S.; Crispin, X.; Salleo, A.; Berggren, M. Experimental Evidence That Short-Range Intermolecular Aggregation Is Sufficient for Efficient Charge Transport in Conjugated Polymers. *Proceedings of the National Academy of Sciences* **2015**, *112* (34), 10599–10604. https://doi.org/10.1073/pnas.1501381112.

(111) Lin, J. B.; Jin, Y.; Lopez, S. A.; Druckerman, N.; Wheeler, S. E.; Houk, K. N. Torsional Barriers to Rotation and Planarization in Heterocyclic Oligomers of Value in Organic Electronics. *J. Chem. Theory Comput* **2017**, *13*, 5624–5638. https://doi.org/10.1021/acs.jctc.7b00709.

(112) Hultell, M.; Stafström, S. Impact of Ring Torsion on the Intrachain Mobility in Conjugated Polymers. *Phys. Rev. B* **2007**, *75* (10), 104304. https://doi.org/10.1103/PhysRevB.75.104304.

(113) Thomas, T. H.; Harkin, D. J.; Gillett, A. J.; Lemaur, V.; Nikolka, M.; Sadhanala, A.; Richter, J. M.; Armitage, J.; Chen, H.; McCulloch, I.; Menke, S. M.; Olivier, Y.; Beljonne, D.; Sirringhaus,

H. Short Contacts between Chains Enhancing Luminescence Quantum Yields and Carrier Mobilities in Conjugated Copolymers. *Nat Commun* **2019**, *10* (1), 1–10. https://doi.org/10.1038/s41467-019-10277-y.

(114) Printz, A. D.; Savagatrup, S.; Burke, D. J.; Purdy, T. N.; Lipomi, D. J. Increased Elasticity of a Low-Bandgap Conjugated Copolymer by Random Segmentation for Mechanically Robust Solar Cells. *RSC Adv.* **2014**, *4* (26), 13635–13643. https://doi.org/10.1039/C4RA00029C.

(115) Sharma, A.; Pan, X.; Campbell, J. A.; Andersson, M. R.; Lewis, D. A. Unravelling the Thermomechanical Properties of Bulk Heterojunction Blends in Polymer Solar Cells. *Macromolecules* **2017**, *50* (8), 3347–3354. https://doi.org/10.1021/acs.macromol.7b00430.

(116) *Fast Scanning Calorimetry*; Schick, C., Mathot, V., Eds.; Springer International Publishing, 2016. https://doi.org/10.1007/978-3-319-31329-0.

(117) Martín, J.; Stingelin, N.; Cangialosi, D. Direct Calorimetric Observation of the Rigid Amorphous Fraction in a Semiconducting Polymer. *J. Phys. Chem. Lett.* **2018**, *9* (5), 990–995. https://doi.org/10.1021/acs.jpclett.7b03110.

(118) Balar, N.; Siddika, S.; Kashani, S.; Peng, Z.; Rech, J. J.; Ye, L.; You, W.; Ade, H.; O'Connor, B. T. Role of Secondary Thermal Relaxations in Conjugated Polymer Film Toughness. *Chem. Mater.* **2020**, *32* (15), 6540–6549. https://doi.org/10.1021/acs.chemmater.0c01910.

(119) Sharma, A.; Pan, X.; Bjuggren, J. M.; Gedefaw, D.; Xu, X.; Kroon, R.; Wang, E.; Campbell, J. A.; Lewis, D. A.; Andersson, M. R. Probing the Relationship between Molecular Structures, Thermal Transitions, and Morphology in Polymer Semiconductors Using a Woven Glass-Mesh-Based DMTA Technique. *Chem. Mater.* **2019**, *31* (17), 6740–6749. https://doi.org/10.1021/acs.chemmater.9b01213.

(120) Meyer, D. L.; Schmidt-Meinzer, N.; Matt, C.; Rein, S.; Lombeck, F.; Sommer, M.; Biskup, T. Side-Chain Engineering of Conjugated Polymers: Distinguishing Its Impact on Film Morphology and Electronic Structure. *J. Phys. Chem. C* **2019**, *123* (33), 20071–20083. https://doi.org/10.1021/acs.jpcc.9b02835.

(121) Jiang, Z. GIXSGUI: A MATLAB Toolbox for Grazing-Incidence X-Ray Scattering Data Visualization and Reduction, and Indexing of Buried Three-Dimensional Periodic Nanostructured Films. *Journal of Applied Crystallography* **2015**, *48* (3), 917–926. https://doi.org/10.1107/S1600576715004434.

(122) Choi, H. H.; Cho, K.; Frisbie, C. D.; Sirringhaus, H.; Podzorov, V. Critical Assessment of Charge Mobility Extraction in FETs. *Nature Mater* **2018**, *17* (1), 2–7. https://doi.org/10.1038/nmat5035.

(123) Schara, S.; Blau, R.; Church, D. C.; Pokorski, J. K.; Lipomi, D. J. Polymer Chemistry for Haptics, Soft Robotics, and Human–Machine Interfaces. *Advanced Functional Materials* **2021**, *31* (39), 2008375. https://doi.org/10.1002/adfm.202008375.

(124) Benight, S. J.; Wang, C.; Tok, J. B. H.; Bao, Z. Stretchable and Self-Healing Polymers and Devices for Electronic Skin. *Progress in Polymer Science* **2013**, *38* (12), 1961–1977. https://doi.org/10.1016/J.PROGPOLYMSCI.2013.08.001.

(125) St. Onge, P. B. J.; Ocheje, M. U.; Selivanova, M.; Rondeau-Gagné, S. Recent Advances in Mechanically Robust and Stretchable Bulk Heterojunction Polymer Solar Cells. *The Chemical Record* **2019**, *19* (6), 1008–1027. https://doi.org/10.1002/tcr.201800163.

(126) Roth, B.; Savagatrup, S.; V. de los Santos, N.; Hagemann, O.; Carlé, J. E.; Helgesen, M.; Livi, F.; Bundgaard, E.; Søndergaard, R. R.; Krebs, F. C.; Lipomi, D. J. Mechanical Properties of a

Library of Low-Band-Gap Polymers. *Chem. Mater.* **2016**, *28* (7), 2363–2373. https://doi.org/10.1021/acs.chemmater.6b00525.

(127) Bridges, C. R.; Ford, M. J.; Thomas, E. M.; Gomez, C.; Bazan, G. C.; Segalman, R. A. Effects of Side Chain Branch Point on Self Assembly, Structure, and Electronic Properties of High Mobility Semiconducting Polymers. *Macromolecules* **2018**, *51* (21), 8597–8604. https://doi.org/10.1021/acs.macromol.8b01906.

(128) Guo, Z.; Shinohara, A.; Pan, C.; Stadler, F. J.; Liu, Z.; Yan, Z.-C.; Zhao, J.; Wang, L.; Nakanishi, T. Consistent Red Luminescence in π-Conjugated Polymers with Tuneable Elastic Moduli over Five Orders of Magnitude. *Mater. Horiz.* **2020**, *7* (5), 1421–1426. https://doi.org/10.1039/D0MH00029A.

(129) Moulton, J.; Smith, P. Electrical and Mechanical Properties of Oriented Poly(3-Alkylthiophenes): 2. Effect of Side-Chain Length. *Polymer* **1992**, *33* (11), 2340–2347. https://doi.org/10.1016/0032-3861(92)90525-2.

(130) Savagatrup, S.; Printz, A. D.; Rodriquez, D.; Lipomi, D. J. Best of Both Worlds: Conjugated Polymers Exhibiting Good Photovoltaic Behavior and High Tensile Elasticity. *Macromolecules* **2014**, *47* (6), 1981–1992. https://doi.org/10.1021/ma500286d.

(131) Ma, Z.; Geng, H.; Wang, D.; Shuai, Z. Influence of Alkyl Side-Chain Length on the Carrier Mobility in Organic Semiconductors: Herringbone vs. Pi–Pi Stacking. *J. Mater. Chem. C* **2016**, *4* (20), 4546–4555. https://doi.org/10.1039/C6TC00755D.

(132) Huang, Y.-W.; Lin, Y.-C.; Yen, H.-C.; Chen, C.-K.; Lee, W.-Y.; Chen, W.-C.; Chueh, C.-C. High Mobility Preservation of Near Amorphous Conjugated Polymers in the Stretched States Enabled by Biaxially-Extended Conjugated Side-Chain Design. *Chem. Mater.* **2020**, *32* (17), 7370–7382. https://doi.org/10.1021/acs.chemmater.0c02258.

(133) Sommerville, P. J. W.; Li, Y.; Dong, B. X.; Zhang, Y.; Onorato, J. W.; Tatum, W. K.; Balzer, A. H.; Stingelin, N.; Patel, S. N.; Nealey, P. F.; Luscombe, C. K. Elucidating the Influence of Side-Chain Circular Distribution on the Crack Onset Strain and Hole Mobility of Near-Amorphous Indacenodithiophene Copolymers. *Macromolecules* **2020**, *53* (17), 7511–7518. https://doi.org/10.1021/acs.macromol.0c00512.

(134) Cendra, C.; Balhorn, L.; Zhang, W.; O'Hara, K.; Bruening, K.; Tassone, C. J.; Steinrück, H.-G.; Liang, M.; Toney, M. F.; McCulloch, I.; Chabinyc, M. L.; Salleo, A.; Takacs, C. J. Unraveling the Unconventional Order of a High-Mobility Indacenodithiophene–Benzothiadiazole Copolymer. *ACS Macro Lett.* **2021**, *10* (10), 1306–1314. https://doi.org/10.1021/acsmacrolett.1c00547.

(135) Chen, H.; Wadsworth, A.; Ma, C.; Nanni, A.; Zhang, W.; Nikolka, M.; Luci, A. M. T.; Perdigão, L. M. A.; Thorley, K. J.; Cendra, C.; Larson, B.; Rumbles, G.; Anthopoulos, T. D.; Salleo, A.; Costantini, G.; Sirringhaus, H.; McCulloch, I. The Effect of Ring Expansion in Thienobenzo[b]Indacenodithiophene Polymers for Organic Field-Effect Transistors. *J. Am. Chem. Soc.* **2019**, *141* (47), 18806–18813. https://doi.org/10.1021/jacs.9b09367.

(136) Venkateshvaran, D.; Nikolka, M.; Sadhanala, A.; Lemaur, V.; Zelazny, M.; Kepa, M.; Hurhangee, M.; Kronemeijer, A. J.; Pecunia, V.; Nasrallah, I.; Romanov, I.; Broch, K.; McCulloch, I.; Emin, D.; Olivier, Y.; Cornil, J.; Beljonne, D.; Sirringhaus, H. Approaching Disorder-Free Transport in High-Mobility Conjugated Polymers. *Nature* **2014**, *515* (7527), 384–388. https://doi.org/10.1038/nature13854.

(137) Zhan, P.; Zhang, W.; Jacobs, I. E.; Nisson, D. M.; Xie, R.; Weissen, A. R.; Colby, R. H.; Moulé, A. J.; Milner, S. T.; Maranas, J. K.; Gomez, E. D. Side Chain Length Affects Backbone Dynamics in Poly(3-Alkylthiophene)s. *Journal of Polymer Science Part B: Polymer Physics* **2018**, *56* (17), 1193–1202. https://doi.org/10.1002/polb.24637.

(138) Reimschuessel, H. K. On the Glass Transition Temperature of Comblike Polymers: Effects of Side Chain Length and Backbone Chain Structure. *Journal of Polymer Science: Polymer Chemistry Edition* **1979**, *17* (8), 2447–2457. https://doi.org/10.1002/pol.1979.170170817.

(139) Fox, T. G.; Flory, P. J. Second-Order Transition Temperatures and Related Properties of Polystyrene. I. Influence of Molecular Weight. *Journal of Applied Physics* **1950**, *21* (6), 581–591. https://doi.org/10.1063/1.1699711.

(140) Ghosh, R.; Chew, A. R.; Onorato, J.; Pakhnyuk, V.; Luscombe, C. K.; Salleo, A.; Spano, F. C. Spectral Signatures and Spatial Coherence of Bound and Unbound Polarons in P3HT Films: Theory Versus Experiment. *J. Phys. Chem. C* **2018**, *122* (31), 18048–18060. https://doi.org/10.1021/acs.jpcc.8b03873.

(141) Ghosh, R.; Pochas, C. M.; Spano, F. C. Polaron Delocalization in Conjugated Polymer Films. *J. Phys. Chem. C* **2016**, *120* (21), 11394–11406. https://doi.org/10.1021/acs.jpcc.6b02917.

(142) Ghosh, R.; Luscombe, C. K.; Hambsch, M.; Mannsfeld, S. C. B.; Salleo, A.; Spano, F. C. Anisotropic Polaron Delocalization in Conjugated Homopolymers and Donor–Acceptor Copolymers. *Chem. Mater.* **2019**, *31* (17), 7033–7045. https://doi.org/10.1021/acs.chemmater.9b01704.

(143) Chew, A. R.; Ghosh, R.; Pakhnyuk, V.; Onorato, J.; Davidson, E. C.; Segalman, R. A.; Luscombe, C. K.; Spano, F. C.; Salleo, A. Unraveling the Effect of Conformational and Electronic Disorder in the Charge Transport Processes of Semiconducting Polymers. *Advanced Functional Materials* **2018**, *28* (41), 1804142–1804142. https://doi.org/10.1002/adfm.201804142.

(144) Koch, F. P. V.; Heeney, M.; Smith, P. Thermal and Structural Characteristics of Oligo(3-Hexylthiophene)s (3HT)n, n = 4–36. *J. Am. Chem. Soc.* **2013**, *135* (37), 13699–13709. https://doi.org/10.1021/ja405792b.

(145) O'Connor, B.; Chan, E. P.; Chan, C.; Conrad, B. R.; Richter, L. J.; Kline, R. J.; Heeney, M.; McCulloch, I.; Soles, C. L.; DeLongchamp, D. M. Correlations between Mechanical and Electrical Properties of Polythiophenes. *ACS Nano* **2010**, *4* (12), 7538–7544. https://doi.org/10.1021/nn1018768.

(146) Griffin, M. F.; Leung, B. C.; Premakumar, Y.; Szarko, M.; Butler, P. E. Comparison of the Mechanical Properties of Different Skin Sites for Auricular and Nasal Reconstruction. *Journal of Otolaryngology - Head & Neck Surgery* **2017**, *46* (1), 33. https://doi.org/10.1186/s40463-017-0210-6.

(147) Savagatrup, S.; Zhao, X.; Chan, E.; Mei, J.; Lipomi, D. J. Effect of Broken Conjugation on the Stretchability of Semiconducting Polymers. *Macromol. Rapid Commun.* **2016**, *37* (19), 1623–1628. https://doi.org/10.1002/marc.201600377.

(148) Sugiyama, F.; Kleinschmidt, A. T.; Kayser, L. V.; Rodriquez, D.; Finn, M.; Alkhadra, M. A.; Wan, J. M.-H.; Ramírez, J.; Chiang, A. S.-C.; Root, S. E.; Savagatrup, S.; Lipomi, D. J. Effects of Flexibility and Branching of Side Chains on the Mechanical Properties of Low-Bandgap Conjugated Polymers. *Polym. Chem.* **2018**, *9* (33), 4354–4363. https://doi.org/10.1039/C8PY00820E.

(149) Wolfe, R. M. W.; Reynolds, J. R. Direct Imide Formation from Thiophene Dicarboxylic Acids Gives Expanded Side-Chain Selection in Thienopyrrolediones. *Org. Lett.* **2017**, *19* (5), 996–999. https://doi.org/10.1021/acs.orglett.6b03830.

(150) Zhang, S.; Ocheje, M. U.; Luo, S.; Ehlenberg, D.; Appleby, B.; Weller, D.; Zhou, D.; Rondeau-Gagné, S.; Gu, X. Probing the Viscoelastic Property of Pseudo Free-Standing Conjugated Polymeric Thin Films. *Macromolecular Rapid Communications* **2018**, *39* (14), 1800092. https://doi.org/10.1002/marc.201800092.

Vita

Parker Sommerville is from Seattle, Washington. He attended Cal Poly, SLO for his undergraduate studies, majoring in Biochemistry. He began his research career his freshman summer in lab of Prof. Willie Swanson, studying the evolution rates of fruit fly genes involved in reproduction. The next fall, he joined the lab of Prof. Derik Frantz at Cal Poly, where he learned synthetic organic chemistry over the course of the next three years; attempting to synthesize strained macrocycles. With a love of aromatic molecules and synthetic organic chemistry, he joined the lab of Prof. Christine Luscombe at the University of Washington for his doctoral studies in developing structure property relationships of IDT-copolymers for soft and stretchable electronics.